

**Quantum dynamics and tunnelling of
methyl rotors studied by field-cycling
NMR**

Cheng Sun, B.Sc.

February 2009

Thesis submitted to the University of Nottingham for the degree of
Doctor of Philosophy

Contents

CHAPTER 1 INTRODUCTION	1
<i>1.1 Reviews and motivations</i>	1
<i>1.2 Quantum molecular tunnelling and field-cycling NMR</i>	3
<i>1.3 Organisation of the thesis</i>	4
<i>1.4 Chemical structures of the samples</i>	5
CHAPTER 2 THEORETICAL	7
<i>2.1 Introduction</i>	7
<i>2.2 Single-particle rotations of the hindered methyl group</i>	7
2.2.1. Molecular motions in the solid state.....	7
2.2.2. Single-particle rotations in molecular solids.....	8
2.2.3. Rotational eigenstates of the methyl group.....	9
<i>2.3 NMR</i>	11
2.3.1. Spin.....	11
2.3.2. Larmor precession.....	12
2.3.3. x -pulse.....	13
2.3.4. Bloch equations.....	15
2.3.5. Pulsed NMR signal – FID.....	16
2.3.6. NMR spectrum.....	17
<i>2.4 Nuclear spin wave functions of the methyl group</i>	18
<i>2.5 Methyl group thermodynamics</i>	20
<i>2.6 Correlation times and the Haupt equation</i>	22
2.6.1. Correlation times.....	22
2.6.2. Correlation function.....	23
2.6.3. Spin-lattice relaxation.....	23
2.6.4. Haupt equation for the methyl group.....	26

2.6.5. Rate equations in ESR tunnel resonance.....	27
--	----

CHAPTER 3 EXPERIMENTAL..... 29

3.1 Introduction.....	29
3.2 Field-cycling NMR spectrometer.....	29
3.2.1. Magnet and magnet power supply.....	30
3.2.2. Cryostat.....	30
3.2.3. Spectrometer.....	31
3.2.4. Apollo NMR console.....	32
3.2.5. Duplexer.....	33
3.2.6. Probe.....	34
3.2.7. Receiver.....	36
3.3 Pulse sequences.....	37
3.3.1. Tuning experiments.....	37
3.3.2. Calibration curve.....	40
3.3.3. Field-cycling T_1 experiments.....	41
3.3.4. Tunnel resonance level-crossing experiment.....	45
3.3.5. Low-field dipole-dipole driven experiment.....	46
3.4 Software.....	48

CHAPTER 4 LOW-FIELD DIPOLE-DIPOLE DRIVEN EXPERIMENTS ON METHYLMALONIC ACID AND METHYL ETHYL KETONE..... 50

4.1 Introduction.....	50
4.2 Theoretical.....	50
4.3 Experimental.....	54
4.4 Results and discussion.....	55
4.4.1. Methylmalonic acid.....	55

4.4.2. Methyl ethyl ketone	62
4.5 Conclusions.....	64

**CHAPTER 5 QUANTUM DYNAMICS AND
TUNNELLING OF THE METHYL ROTOR IN SODIUM
ACETATE TRIHYDRATE AND SORBIC ACID..... 65**

5.1 Introduction.....	65
5.2 Theoretical	66
5.2.1. Methyl groups.....	66
5.2.2. Hydrogen bonds.....	67
5.3 Experimental.....	68
5.4 Results and discussion.....	68
5.4.1. Sodium acetate trihydrate.....	68
5.4.2. Sorbic acid.....	74
5.5 Conclusions.....	81

**CHAPTER 6 TUNNELLING RESERVOIRS IN COPPER
DOPED ZINC ACETATE DIHYDRATE AND TOLUENE
DOPED WITH DPPH RADICALS..... 83**

6.1 Introduction.....	83
6.2 Theoretical.....	84
6.3 Experimental.....	88
6.3.1. Copper doped zinc acetate dihydrate.....	88
6.3.2. Toluene doped with DPPH radicals.....	90
6.3.3. Numerical simulations.....	91
6.4 Results and discussion.....	92
6.4.1. Copper doped zinc acetate dihydrate.....	92

6.4.2. Toluene doped with DPPH radicals.....	105
6.5 Conclusions.....	108
CHAPTER 7 SUMMARY.....	110
CHAPTER 8 BIBLIOGRAPHY.....	112

List of Figures

Figure 2.1 (a) Schematic structure and (b) top view of a methyl rotor; ϕ is an angle describing the position of the methyl rotor.....	9
Figure 2.2 Schematic diagram of energy levels of the methyl rotor under a three-fold hindering potential of magnitude V_3 ; figure adapted from Ref. [4].....	10
Figure 2.3 Zeeman energy levels for a spin $I = 3/2$ particle.....	12
Figure 2.4 Larmor precession of the magnetic moment.....	13
Figure 2.5 rf pulse and the induced NMR signal (FID)	17
Figure 2.6 Schematic NMR spectrum; real part indicated by the solid line and imaginary part indicated by the dashed line.....	18
Figure 2.7 Zeeman splittings of the ground torsional state of the methyl group under an applied magnetic field B_0 ; ω_L is the ^1H Larmor frequency and ω_t is the methyl tunnelling frequency.....	20
Figure 2.8 Schematic interpretation of methyl group thermodynamics in terms of thermal reservoirs associated with tunnelling and Zeeman energy; T_1 is the spin-lattice relaxation time and τ_{con} is the $A-E$ conversion time constant; the tunnelling reservoir and the Zeeman reservoir can be coupled under the tunnel resonance conditions [6].....	21
Figure 2.9 Schematic diagram of two potential wells.....	22
Figure 2.10 Schematic diagram of a two spin-state system.....	24
Figure 3.1 Schematic diagram of the magnet and cryostat.....	31
Figure 3.2 Schematic overview of the heterodyne NMR spectrometer.....	32
Figure 3.3 Schematic diagram of the crossed diodes.....	33
Figure 3.4 Schematic diagram of the duplexer circuit.....	33
Figure 3.5 Picture of the NMR probe.....	34
Figure 3.6 Schematic diagram of the series tank circuit	35
Figure 3.7 Schematic diagram of the quadrature receiver.....	36
Figure 3.8 Pulse sequence of the tuning experiment without saturation.....	38
Figure 3.9 Pulse sequence of the tuning experiment with saturation.....	38
Figure 3.10 Schematic diagram of the NMR signal acquisition.....	39
Figure 3.11 Pulse sequence of the probe calibration experiment.....	40
Figure 3.12 Normalised calibration curve; the data were recorded at the off-resonant field $B_{\text{nmr}} + \Delta B$	41
Figure 3.13 Pulse sequence of the saturation-recovery experiment.....	42
Figure 3.14 Saturation-recovery experimental data of the spin-lattice relaxation time T_1 for ^1H in sodium acetate trihydrate recorded at $T = 7.45\text{K}$ and $B_r = 0.0375\text{T}$; the solid line was obtained from the curve fitting; $T_1 = 357 \pm 7$ s.....	42
Figure 3.15 Pulse sequence of the polarisation-recovery experiment.....	43

Figure 3.16 Polarisation-recovery experimental data of the spin-lattice relaxation time T_1 for ^1H in sodium acetate trihydrate recorded at $T = 57\text{K}$ at $B_r = 0.0375\text{T}$; the ^1H spin was polarised at $B_{\text{pol}} = 0.863\text{T}$ for $\tau_{\text{pol}} = 10\text{s}$; the solid line was obtained from the curve fitting; $T_1 = 3.77 \pm 0.08 \text{ s}$	44
Figure 3.17 Level-crossing pulse sequence of the tunnel resonance experiment.....	45
Figure 3.18 Tunnel resonance spectra of m-xylene doped with DPPH radicals recorded at $T = 4.2\text{K}$; both field scan directions have been conducted.....	46
Figure 3.19 Pulse sequence of the low-field dipole-dipole driven experiment.....	47
Figure 3.20 Low-field NMR spectrum of Methylmalonic acid recorded at $T = 4.2\text{K}$ and $B_{\text{low}} = 0.175\text{T}$	48
Figure 4.1 Saturation conditions of the tunnelling transitions in the $\beta_t - \beta_z$ space.....	52
Figure 4.2 Schematic illustration of the population evolution of the Zeeman and tunnelling reservoirs in the low-field NMR experiment.....	54
Figure 4.3 Pulse sequence of the stirring low-field NMR experiment; a loop of two-frequency rf irradiations was utilised.....	54
Figure 4.4 Low-field NMR spectrum of methylmalonic acid recorded at $T = 4.2\text{K}$ and $B_{\text{low}} = 0.0183\text{T}$	56
Figure 4.5 Stirring low-field NMR spectra of methylmalonic acid recorded at $T = 4.2\text{K}$ and $B_{\text{low}} = 0.0183\text{T}$	57
Figure 4.6 Results from numerical simulations of the stirring low-field NMR spectra of methylmalonic acid at $B_{\text{low}} = 0.0183\text{T}$; $\nu_t = 77\text{kHz}$	59
Figure 4.7 Irradiation time-dependence of the stirring low-field NMR spectra of methylmalonic acid recorded at $T = 4.2\text{K}$ and $B_{\text{low}} = 0.0183\text{T}$	60
Figure 4.8 Results from numerical simulations of irradiation time-dependence of the stirring low-field NMR spectra of methylmalonic acid at $B_{\text{low}} = 0.0183\text{T}$	60
Figure 4.9 Irradiation time-dependence of the relative change in ^1H polarisation, $\Delta I_z / I_z$, at the a- and a+ tunnelling transitions in methylmalonic acid at $B_{\text{low}} = 0.0183\text{T}$	61
Figure 4.10 Low-field NMR spectrum of methyl ethyl ketone recorded at $T = 4.2\text{K}$ and $B_{\text{low}} = 0.00234\text{T}$	62
Figure 4.11 Irradiation time-dependence of the stirring low-field NMR spectra of methyl ethyl ketone recorded at $T = 4.2\text{K}$ and $B_{\text{low}} = 0.0143\text{T}$ with $\nu_{\text{stir}} = 724\text{kHz}$	63
Figure 5.1 Inverse temperature dependence of the inverse spin-lattice relaxation time T_1^{-1} for ^1H in sodium acetate trihydrate; solid lines were obtained from simulations (EE components in the long-dash line and AE in the short-dash line).....	69
Figure 5.2 Spectral densities of sodium acetate trihydrate recorded at (a) $11.1\text{K} \leq T \leq 29.0\text{K}$ and (b) $34.0\text{K} \leq T \leq 46.0\text{K}$; solid lines in (a) were obtained from curve fittings.....	70
Figure 5.3 Inverse temperature dependence of the inverse correlation time τ_c^{-1} in sodium acetate trihydrate; the solid line indicates the fitting.....	72

Figure 5.4 Tunnel resonance spectra of sorbic acid recorded at $T = 34.8\text{K}$; solid lines are guides to the eye.....	74
Figure 5.5 Low-field NMR spectra of sorbic acid recorded at $T = 30.0\text{K}$	75
Figure 5.6 Inverse temperature dependence of the inverse spin-lattice relaxation time T_1^{-1} for ^1H in sorbic acid; solid lines were obtained from simulations (components arising from proton transfer are indicated by dashed lines).....	76
Figure 5.7 Spectral densities of sorbic acid recorded at (a) $50.0\text{K} \leq T \leq 61.5\text{K}$ and (b) $33.3 \leq T \leq 40.0\text{K}$; solid lines in (a) were obtained from curve fittings; solid lines in (b) represent simulations.....	77
Figure 5.8 Inverse temperature dependence of the inverse correlation time τ_c^{-1} for CH_3 reorientation in sorbic acid; solid line indicates the fitting.....	79
Figure 5.9 Spectral density of sorbic acid recorded at $T = 36.4\text{K}$; the solid line was obtained from the simulation (component arising from proton transfer and EE components of methyl reorientation are indicated by dashed lines, and AE components are plotted in dot-dash line; offset by -0.03 for clarity).....	80
Figure 6.1 Schematic diagrams of the tunnelling state transitions in ESR tunnel resonance in terms of thermal reservoirs.....	86
Figure 6.2 Schematic diagram of spectral tunnel diffusion amongst methyl tunnelling subgroups; $\omega_t^{(i)} - \omega_t^{(i\pm)} = \pm \omega_n$	88
Figure 6.3 Field-cycling NMR pulse sequence of the tunnelling reservoir cooling experiment... 89	89
Figure 6.4 Field-cycling NMR pulse sequence of the tunnel diffusion experiment.....	90
Figure 6.5 Schematic diagram of the numerical simulation of the ESR tunnel resonance phenomena.....	91
Figure 6.6 Tunnel resonance spectra of copper doped zinc acetate dehydrate; the data were recorded at $T = 4.2\text{K}$; solid lines represent simulation results.....	92
Figure 6.7 Tunnel resonance spectra of copper doped zinc acetate dihydrate (1:18.2) with field scan directions of (a) high-to-low-to-high and (b) low-to-high-to-low ($T = 4.2\text{K}$); solid lines represent simulation results.....	94
Figure 6.8 Results from summation and subtraction of the tunnel resonance spectra of copper doped zinc acetate dihydrate (1:54.5) recorded in both field directions ($T = 4.2\text{K}$); solid lines represent simulation results.....	96
Figure 6.9 (a) Evolution of tunnelling temperatures θ_t as a function of time t and tunnelling frequency ν from simulation of the tunnel resonance spectra in Fig. 6.7a; (b) plot of tunnelling temperature vs. tunnelling frequency.....	98
Figure 6.10 (a) plot of time t vs. tunnelling frequency ν and (b) plot of tunnelling temperature θ_t vs. time t from simulation of the tunnel resonance spectra in Fig. 6.7a.....	99
Figure 6.11 Cooling of the tunnelling reservoir in copper doped zinc acetate dihydrate single crystals ($T = 4.2\text{K}$); solid lines represent simulation results.....	100

Figure 6.12 Results of the tunnel diffusion experiments conducted on copper doped zinc acetate dihydrate ($T = 4.2\text{K}$); solid lines represent simulation results.....	102
Figure 6.13 Evolution of tunnelling temperatures θ_i as a function of time t and tunnelling frequency ν from the simulation of the tunnel diffusion curve shown as the red, filled squares in Fig. 6.12.....	103
Figure 6.14 Results of the saturation-recovery experiments on copper doped Zinc acetate dihydrate ($T = 4.2\text{K}$); solid lines represent simulation results.....	104
Figure 6.15 Tunnel resonance spectra of toluene doped with DPPH radicals ($T = 4.2\text{K}$); dashed lines are shown as eye guides.....	106
Figure 6.16 Result of numerical simulation of the tunnel resonance spectrum of toluene with DPPH radical with $\tau_{\text{rec}} = 70\text{s}$; experimental data are shown as points.....	107

List of Tables

Table 1.1 Chemical structures of the samples.....	5
Table 1.2 Chemical structures of the samples (continued).....	6
Table 2.1 Classification of single-particle rotations in molecular solids in terms of rotational potential [20].....	8
Table 2.2 Nuclear spin eigenfunctions of the methyl group; $\varepsilon = \exp(2\pi i/3)$	19
Table 5.1 Best fit parameters for sodium acetate trihydrate and sorbic acid.....	82
Table 6.1 Best fit values of the cooling rate of the tunnelling reservoir in copper doped zinc acetate single crystals.....	101
Table 6.2 Best fit parameters for copper doped zinc acetate single crystals; $g_{\text{obs}} = 2.38 \pm 0.03$, $A_{\text{Cu}} = 7.25 \pm 0.05$ mT, $\omega_t = 7.25 \times 10^9 \text{ s}^{-1}$ [71] and $b = (1.9 \pm 0.1) \times 10^8 \text{ s}^{-1}$	105
Table 6.3 Best fit parameters for toluene doped with DPPH radicals.....	108

Abstract

Quantum dynamics and tunnelling of methyl rotors has been studied using field-cycling nuclear magnetic resonance (NMR) spectrometer, in a variety of samples. The characteristic frequency of the tunnelling motion of methyl groups has been investigated using both low-field dipole-dipole driven experiments and tunnel resonance level-crossing experiments. The classical hopping and quantum tunnelling of methyl groups have been studied by making temperature-dependent and field-dependent measurements of the spin-lattice relaxation time T_1 . The spectral density functions of the dipolar interaction, mediated by the rotation of methyl groups, have been directly plotted, and the correlation times characteristic of the rotational motion have been determined.

Electron spin resonance (ESR) tunnel resonance spectra have been studied in samples with unpaired electrons by making resonant contact between the methyl tunnelling reservoir and the electron spins. The phenomenon of dynamic proton polarisation (DNP) has also been investigated in these samples. Experiments demonstrating the cooling of methyl tunnelling reservoir and the diffusion of energy amongst tunnelling reservoirs are presented.

In low-field dipole-dipole driven experiments, in order to avoid the tunnelling transition saturation problem, the sideband stirring radiofrequency (rf) irradiation technique has been utilised and the low-field NMR spectra have been observed with enhanced sideband peaks. The rf irradiation time-dependence of the low-field spectra has been investigated.

The experimental data is supported by numerical simulations, using appropriate theoretical models.

Acknowledgements

This thesis is dedicated to my beloved parents: Mrs Xia Ren and Mr Min Sun.

Sincere thanks go to my PhD supervisor Professor Anthony J. Horsewill for all his kindly supervision throughout the last three years. I have acquired a great deal of knowledge about molecular quantum tunnelling and NMR from him, and for that I am truly grateful.

Many thanks to Professor John R. Owers-Bradley for all of his help and input during the course of my research.

I would like to thank Dr. Daniel Noble for his guidance on the use of the field-cycling NMR spectrometer, and Dr. Kuldeep S. Panesar, Ilya Frantsuzov and Mark J. Patton for their invaluable discussions regarding both physics and the English language.

Thanks also go to Chris Pallender and David Holt for their help with helium supply and to Bob Chettle for his help in maintaining the NMR probes.

Finally, I would like to thank the University of Nottingham for the EPSRC scholarship support and the China postgraduate research scholarship.

Chapter 1 Introduction

1.1 Reviews and motivations

In 1687, since Sir Isaac Newton published his famous laws of motion in the seminal *Philosophiae Naturalis Principia Mathematica* [1], thereby establishing the classical mechanics that govern the classical motion of physical objects, it seemed that all motions in our world could be predicted using classical mechanics. However following this, a series of discoveries brought this assertion into question; including the discovery of cathode rays by Michael Faraday in 1838 [2], the statement of the black body radiation problem by Gustav Kirchhoff in 1859 [3], the suggestion of discrete energy states by Ludwig Boltzmann in 1877 and the proposal of quantum hypothesis by Max Planck in 1900 [3]. In 1905 the explanation of the photoelectric effect by Albert Einstein [3] finally guided us towards the quantum aspects of our world.

There are many novel characteristics of quantum mechanics: (a) the quantisation of certain physical quantities, (b) wave-particle duality, (c) the uncertainty principle and (d) quantum entanglement. Among manifestations of the wave-like nature of matter, the phenomenon of quantum tunnelling is one of the most interesting and remarkable. Especially at low temperatures, the dynamics of atoms or molecular groups with low mass can be dominated by the effects of tunnelling, displaying significant and very obvious departures from classical behaviour as the particles are free to explore potential energy regions that are classically forbidden. Furthermore, the requirements of the antisymmetry principle for fermions can also have a profound effect, giving rise to quantum dynamical behaviour that has no classical analogue.

As an example of one dimensional rotational motion, the methyl rotor (CH_3) is a very good, convenient model to study quantum dynamics and to test the corresponding theories. Therefore, the phenomena associated with quantum dynamics that characterise the CH_3 rotational states have been widely studied [4]. The methyl rotor has a high degree of spatial symmetry and the dynamics are substantially influenced by the requirements of spin-symmetry. It exhibits coherent quantum tunnelling characteristics whereby the probability of finding the protons oscillates among potential wells. In molecular systems where methyl groups are present, the motion of CH_3 rotor will invariably provide the dominant nuclear spin-lattice relaxation mechanism, especially at low temperature, and

therefore nuclear magnetic resonance (NMR) provides one means to investigate the dynamical behaviour.

Before the influence of methyl tunnelling in solid state NMR began to be considered in the 1950s [5, 6], several effects due to the rotational motion of methyl groups had been studied by various means [7–10]. The rotational motion of methyl groups was first inferred from measurements of bulk macroscopic properties such as the dielectric constant in the 1930s [7]. The first solid state NMR studies of methyl group rotation were focused on temperature dependence of the shape of the proton NMR absorption peak in the late 1940s [8, 9]. In 1950, molecular reorientation was taken into account by Gutowsky and Pake to investigate NMR lineshapes [10]. In 1955, a quantum tunnelling process together with a classical over-barrier hopping process was considered by Gutowsky and co-workers [5]. Since then, the influence of methyl tunnelling on the proton spin-lattice relaxation time T_1 has been widely studied [6, 11, 12].

In the 1970s, direct measurements of methyl tunnelling frequencies via NMR and inelastic neutron scattering (INS) became possible [13, 14]. Since then, NMR and neutron scattering have been the most important techniques for studying the methyl tunnelling properties. Additionally, a comprehensive table of methyl tunnelling frequencies has been compiled by Prager and Heidemann [15] comprising an extensive bibliography of papers relating to methyl tunnelling.

To date, decades of development in NMR have enabled us to study in depth not only methyl tunnelling frequencies [16] but also methyl tunnelling related phenomena (e.g. electron spin tunnel resonance [17, 18]). In particular, the emergence of field-cycling NMR [4] provides us with an important tool for investigating the molecular dynamical spectrum where the influence of methyl tunnelling on nuclear spin relaxation can be revealed. However, there have also been a number of significant, open questions in the field of NMR (such as whether the Lorentzian component due to methyl tunnelling proposed by Haupt [12] can be observed in the molecular dynamical spectrum, whether the cooling process of tunnelling temperature at electron spin tunnel resonance can be revealed and whether diffusion of tunnelling energy can be shown, etc.). The motivation behind this thesis is to address these open questions using field-cycling NMR. A brief introduction to both theoretical and experimental investigations in this work is presented in next section.

1.2 Quantum molecular tunnelling and field-cycling NMR

In quantum mechanics the Exclusion Principle [19] plays a very important role. In general, the CH₃ rotator has three-fold symmetry and the ground torsional state is split by a tunnelling splitting, separating two rotational energy levels: *A* and degenerate E_a and E_b . In methyl groups, only symmetric complete wave functions are allowed [20] as the consequence of the Exclusion Principle. The constraint means that the *A* species is a nuclear spin quartet with the total spin $I = 3/2$ while the degenerate E_a and E_b species are nuclear spin doublets with the total spin $I = 1/2$. *A-E* conversion is therefore spin restricted. A methyl tunnelling reservoir [4] can be identified associated with the *A* and *E* nuclear spin symmetry species which are thermally isolated from the lattice, particularly at low temperature.

In solid state NMR, molecular dynamics have often been investigated through experiments that probe the nuclear spin relaxation and polarisation properties. Information on the correlation times for the motion is most readily extracted from experiments that investigate the nuclear spin relaxation properties of the system, for example through temperature and field dependent measurements of the spin-lattice relaxation time T_1 . Methyl groups undergo quantum tunnelling with a well-defined frequency, which can give rise to discrete features in the NMR spectrum [4, 20]. The tunnelling frequencies have a wide range from a few kHz to hundreds of GHz, depending on the molecular environment that the particular methyl groups experience.

At high magnetic field, transitions between rotational states of *A* and *E* symmetry are forbidden due to the Selection Rules [3]. However at low magnetic field, the Selection Rules are dramatically modified, and the states are not pure *A* and *E* states, therefore some transitions forbidden at high field become allowed in the presence of radiofrequency (rf) irradiation. Based on this idea, by utilising magnetic field-cycling NMR [4], a variety of low-field dipole-dipole driven experiments have been developed to study the quantum tunnelling properties of methyl groups, especially to measure the tunnelling frequency directly.

In paramagnetic samples, the phenomena of electron spin resonance (ESR) tunnel resonances [21–23] may be observed when methyl tunnelling reservoirs are brought into resonant contact with the electron spins under an appropriate magnetic field. Due to the spin symmetry requirements, tunnel resonances are accompanied by changes in the nuclear spin states. Because the ratio of the electron and nuclear magnetic moments is very large, the nuclear polarisation can be substantially enhanced, thereby giving rise to the phenomenon of dynamic

nuclear polarisation (DNP) [24, 25]. Therefore NMR signals can be substantially improved using the phenomenon of DNP.

It is crucial to reveal the molecular dynamics and the tunnelling characteristics in a much broader magnetic field region. Using field-cycling NMR it becomes possible to map out directly the spectral density associated with the molecular dynamics. Field-cycling techniques have also been utilised to achieve rapid excursions in the magnetic field, thereby allowing reliable measurements of the spin-lattice relaxation time T_1 at low field.

1.3 Organisation of the thesis

Chapter 2 is a theoretical section where the background knowledge is introduced. First of all, rotations of methyl groups are described. Secondly principles of NMR are discussed. A thermodynamic model for the methyl group is then introduced. Correlation times are defined that describe the molecular motion, and the Haupt equation is discussed. Finally the rate equations in the ESR tunnel resonance are shown.

In Chapter 3 the experimental aspects of the thesis research are discussed. Firstly the technical characteristics of the Nottingham field-cycling NMR spectrometer including the magnet and cryostat are presented. The pulse sequences used for the various experiments are then introduced. Finally the associated software including NTNMR, Visual Basic and Matlab are described.

In Chapters 4 to 6, experimental results from investigations of three different methyl group tunnelling-related phenomena are presented and discussed. Chapter 4 describes the study of low-field NMR experiments, Chapter 5 presents the study of the temperature and field dependence of the spin-lattice relaxation time T_1 , and Chapter 6 discusses the study of the ESR tunnel resonances.

In Chapter 4 the low-field NMR spectra of methylmalonic acid and methyl ethyl ketone observed using low-field dipole-dipole driven NMR are presented. This low-field NMR technique applies particularly to the investigation of strongly hindered methyl groups with small tunnelling frequencies. Additionally using the tunnelling sideband stirring rf irradiation technique, the irradiation time dependence of the low-field NMR spectrum is also discussed.

In Chapter 5 focusing on the tunnelling properties, investigations conducted on sodium acetate trihydrate and sorbic acid are demonstrated. Among the results regarding sodium

acetate trihydrate, the Haupt peak arising from the methyl tunnelling [12] is observed in the plot of inverse spin-lattice relaxation time as a function of inverse temperature. Spectral density plots at both low temperatures and higher temperatures are presented. For sorbic acid both the temperature and field dependence of T_1 are discussed. Resonant features associated with the methyl tunnelling frequency are observed not only in the spectral densities but also in tunnel resonance experiments and low-field dipole-dipole driven experiments. Additionally in sorbic acid, spin-lattice relaxation components arising from the concerted proton transfer in the hydrogen bonds of the carboxylic acid dimer are also observed in the relaxation spectra.

Chapter 6 presents observations of DNP phenomena in copper doped zinc acetate dihydrate single crystals and in α -crystalline toluene doped with DPPH radicals. In copper doped zinc acetate dihydrate, apart from the DNP signal arising from the resonant contact between methyl tunnelling reservoirs and electron spins, the DNP signals arising from spectral diffusion amongst methyl tunnelling reservoirs are also observed. The cooling of the tunnelling reservoir and tunnel diffusion are then discussed. However the DNP spectra of toluene doped with DPPH radicals are presented as an example of a system without tunnel diffusion.

In Chapter 7 the work is summarised and important conclusions are discussed.

1.4 Chemical structures of the samples

In the research of the methyl tunnelling characteristics, a variety of samples have been studied. For the purpose of convenience, schematic chemical structures of the samples have been summarised in Table 1.1 and 1.2

Name	Molecular formula	Chemical structure
Methylmalonic acid	$C_4H_6O_4$	
Methyl ethyl ketone	C_4H_8O	

Table 1.1 Chemical structures of the samples

Name	Molecular formula	Chemical structure
Sodium acetate trihydrate	$\text{NaC}_2\text{H}_3\text{O}_2 \cdot 3\text{H}_2\text{O}$	
m-xylene	C_8H_{10}	
DPPH (2,2-Diphenyl-1-picrylhydrazyl)	$\text{C}_{34}\text{H}_{44}\text{N}_5\text{O}_6$	
Sorbic acid	$\text{C}_6\text{H}_8\text{O}_2$	
Toluene	C_7H_8	
Zinc acetate dihydrate	$\text{ZnC}_4\text{H}_{10}\text{O}_6$	

Table 1.2 Chemical structures of the samples (continued)

Chapter 2 Theoretical

2.1 Introduction

Since the 1970s systematic efforts have been made to study quantum tunnelling of atoms and molecules in molecular solids both experimentally and theoretically. Among the characteristics of molecules in the solid state, rotational dynamics is one of the most fascinating aspects. The field may be divided into collective and single-particle rotational motions [20]. In studies of methyl rotors it is convenient to treat the methyl rotational motions as single-molecule rotations. The influence of the methyl rotational dynamics on NMR has been recognised for many years [5, 6, 26]. In parallel with neutron scattering techniques [20, 27], NMR spectroscopy has been one of the most effective tools for investigating the rotational dynamics of methyl groups. Therefore, before describing the experiments conducted, it is necessary to introduce some basic theories and knowledge regarding methyl rotors and NMR [28–32].

In this chapter relevant theories will be introduced. In section 2.2 the basic idea of single-particle rotational motions will be discussed. In section 2.3 the basic background knowledge of NMR will be introduced. The nuclear spin wave functions of the methyl rotor will be discussed in section 2.4. The thermodynamics of methyl groups will be introduced in section 2.5. Finally the correlation time of CH₃ rotation, and the effect of this motion on ¹H spin-lattice relaxation will be discussed in section 2.6.

2.2 Single-particle rotations of the hindered methyl group

2.2.1 Molecular motions in the solid state

In the solid state, the internal molecular dynamics are mainly vibrations and rotations. In general, all nuclei oscillate rapidly around their mean positions. These motions are called vibrations, and are usually on the timescale of picoseconds (10^{-12} s) [29]. Light atoms such as hydrogen undergo rapid local oscillations, and these highly local motions are called librations. At low temperature, energy levels are quantised and the molecules sit in a discrete number of librational (or torsional) states.

Many symmetrical molecular groups such as methyl groups rotate rapidly about their local axes. This rotational motion is typically on the picosecond timescale at room temperature, but

may be slower if the motion is hindered. At low temperature the rotational motion gives rise to a tunnelling splitting for each torsional state and this will be discussed later.

2.2.2 Single-particle rotations in molecular solids

Molecular rotations are grouped into three types, depending on the number of rotational degrees of freedom. Here only the one dimensional case will be introduced since the methyl group has one rotational degree of freedom. Single-molecule rotations describe the rotational motion of a single molecule in its surroundings that can be approximated as an angle-dependent potential comprising a time-independent part and a fluctuating part. The fluctuating potential is mainly related to the lattice temperature whereas the static part is normally referred to as the hindering potential in the presence of methyl groups.

Single-particle rotations depend upon the relative magnitude of both potentials. Table 2.1 describes the classification of single-particle rotations in molecular solids in terms of the rotational potential. Different characteristic situations are distinguished by the magnitude of the static and the fluctuating part of the potential. At high temperature frequent transitions between the rotational states and phonon states in the solid give rise to a strong fluctuating potential. In the circumstances of strong static potential the heavily hindered molecules are confined to a discrete number of equilibrium orientations, transitions across barriers occur with thermally activated jumps or hops. This classical jump motion is also known as the molecular reorientation. In some disordered crystals the static (or hindering) potential is weak, and diffusion of the molecules with respect to their angular degrees of freedom occurs.

Fluctuating potential \ Static potential	Strong (high T)	Weak (low T)
Strong	Rotational jumps	Librations and rotational tunnelling
Weak	Rotational diffusion	Quantum-mechanical free rotation

Table 2.1 Classification of single-particle rotations in molecular solids in terms of rotational potential [20]

By contrast, at low temperature only few lattice phonon modes are populated and the system is in its rotational ground state. Therefore the fluctuating potential is weak and the quantum mechanics come into play. Due to the overlap of the wave functions in the neighbouring potential wells there is a tunnelling splitting of the torsional states of the molecules. Most

systems are hindered, thus only the quantum tunnelling through barriers is allowed. Systems with very weak static potentials are not very common; solid hydrogen [33] is one example that is a quantum crystal not only with respect to its rotational degrees of freedom but with respect to its translational degrees of freedom.

In this thesis, systems with hindered methyl groups have been studied, therefore with increasing temperature the continuous transition between the regime of quantum tunnelling and the regime of classical hopping is of interest.

2.2.3 Rotational eigenstates of the methyl group

In this thesis, molecules containing hindered methyl groups have been studied. A methyl group (Fig. 2.1) consists of one carbon atom and three hydrogen atoms binding with covalent bonds.

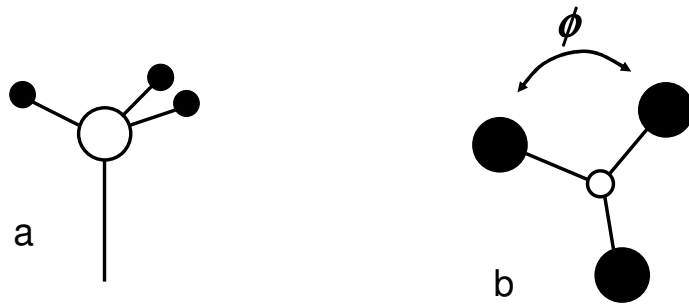


Figure 2.1 (a) Schematic structure and (b) top view of a methyl rotor; ϕ is an angle describing the position of the methyl rotor

In symmetrical methyl groups, the intra-group bonds are strong and the vibrational energy separations are large compared with temperature fluctuations ($\sim k_B T$) for molecules at room temperature and below. Therefore, the methyl rotor only occupies the ground vibrational state and is fairly rigid. Thus the methyl rotor may be considered as a rigid equilateral triangle of hydrogen atoms. Therefore we can identify a three-fold symmetry axis which is perpendicular to the paper in Fig. 2.1b, and the rotational motion of the methyl group can be defined in one dimension in terms of the angle ϕ . Inevitably, there is an environment surrounding the methyl group, and non-bonding interactions between the methyl group atoms and the molecular environment give rise to a hindering potential $V(\phi)$. Because of the three-fold symmetrical spatial configuration (the potential V_3 is illustrated in Fig. 2.2) the hindering potential has three minima which are separated by the interceding hindering barrier.

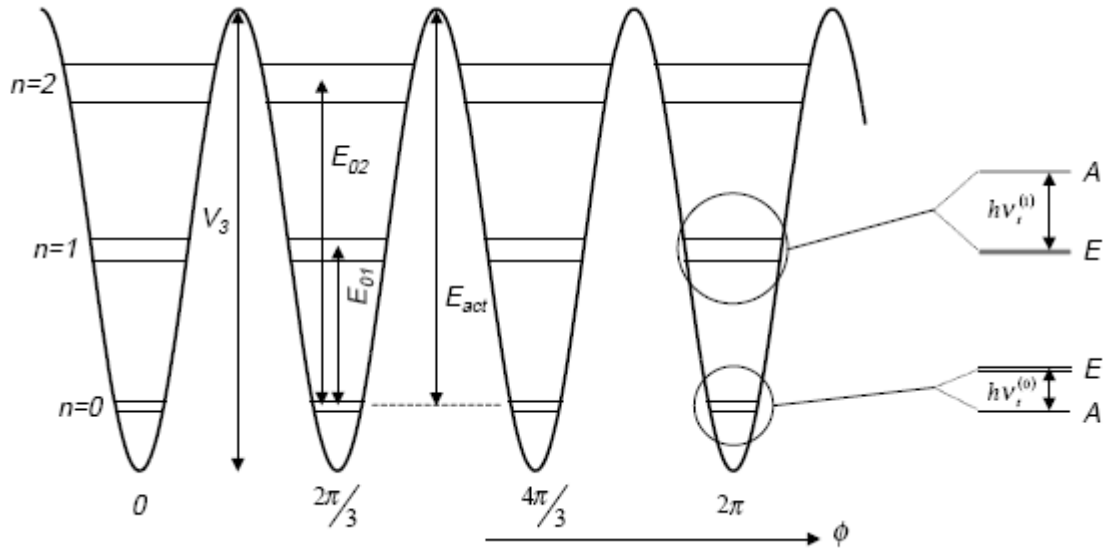


Figure 2.2 Schematic diagram of energy levels of the methyl rotor under a three-fold hindering potential of magnitude V_3 ; figure adapted from Ref. [4]

In Fig. 2.2 the hindering potential is related to the spatial degrees of freedom of the methyl group. Generally speaking, it is a time-independent potential, therefore the rotational Hamiltonian of the methyl group is time-independent and is written as,

$$\hat{H}_R = \frac{-\hbar^2}{2I} \frac{\partial^2}{\partial \phi^2} + V(\phi) \quad (2.1)$$

where I is the moment of inertia of the methyl group ($I = 5.31 \times 10^{-47} \text{kg m}^2$). The hindering potential may be written as a Fourier series consisting of three-fold, six-fold and higher harmonics,

$$V(\phi) = \sum \frac{V_{3l}}{2} [1 - \cos(3l(\phi + \chi_{3l}))] \quad (2.2)$$

where χ_{3l} is a phase angle and l is an integer. Because the symmetry of the methyl group is C_3 , the eigenstates corresponding to the rotational Hamiltonian are classified by the irreducible representations of the symmetry group which are A , E_a and E_b . In order to determine the rotational eigenfunctions $|\psi_R\rangle$ of the rotational Hamiltonian, the system can be described in terms of a basis set comprising harmonic oscillator states $|n, \phi_i\rangle$, where $i = 1, 2, \text{ or } 3$ and n defines the torsional states. It is worth noting that these states are localised in the individual potential wells. The eigenfunctions of the rotational Hamiltonian can be written as linear combinations of the basis harmonic oscillator states $|n, \phi_i\rangle$, and due to their symmetry, the combinations are written as follows,

$$\begin{aligned}
|n, A\rangle &= \frac{1}{\sqrt{3}}(|n, \varphi_1\rangle + |n, \varphi_2\rangle + |n, \varphi_3\rangle) \\
|n, E_a\rangle &= \frac{1}{\sqrt{3}}(|n, \varphi_1\rangle + \varepsilon|n, \varphi_2\rangle + \varepsilon^*|n, \varphi_3\rangle) \\
|n, E_b\rangle &= \frac{1}{\sqrt{3}}(|n, \varphi_1\rangle + \varepsilon^*|n, \varphi_2\rangle + \varepsilon|n, \varphi_3\rangle)
\end{aligned} \tag{2.3}$$

where $\varepsilon = \exp(2\pi i/3)$. In Eqn. (2.3) it is clear that these states are delocalised over the three potential wells, and it is this wave function overlap in the barrier regions that gives rise to the phenomenon of tunnelling.

The eigenstates of the hindered methyl group are illustrated in Fig. 2.2. The torsional states are labelled by n . The right-hand side of Fig. 2.2 shows the close up of the splitting of the n th torsional level $|n, A\rangle$ and $|n, E\rangle$ with A and E symmetry, respectively. The A - E splitting $h\nu_t^{(n)}$ corresponds to quantum tunnelling between A and E states, where $\nu_t^{(n)}$ is the tunnelling frequency of the n th torsional level. In fact the E states are degenerate with two states $|n, E_a\rangle$ and $|n, E_b\rangle$, which are related to E_a and E_b symmetry, respectively. In the ground torsional state (i.e. $n=0$), the A state has the lowest energy. For the excited torsional states, the barrier is narrower, therefore the tunnelling splitting is larger. Typical $\nu_t^{(1)}$ is approximately 30 times larger than that of ground state $\nu_t^{(0)}$, and the E states have a lower energy than the A state. The relative magnitudes of the A and E states alternate at even higher excited torsional states.

As shown in Fig. 2.2 the thermal activation energy E_{act} is defined as the height from the ground torsional state to top of the barrier, and the energy difference between the ground torsional state to the first (second) excited torsional state is labelled E_{01} (E_{02}).

2.3 NMR

2.3.1 Spin

As well as the fundamental properties of mass and charge, atomic nuclei also have another fundamental property – spin. Although there is no classical analogue to describe spin, some macroscopic phenomena arising from spin may be familiar to the layperson, for example, ferromagnetism arising from the strong dipole-dipole interactions of electron spins. For spin it is the spin angular momentum that characterises this intrinsic property.

Protons possess a spin of $I = 1/2$, therefore they have a magnetic moment due to their spin,

$$\underline{\mu} = \gamma \underline{I} \quad (2.4)$$

where γ is the magnetogyric ratio for the proton. The fact that protons and other nuclei have spin is the fundamental origin of the phenomenon of NMR.

When a nucleus is subjected to a magnetic field B , the Hamiltonian operator is given by,

$$\hat{H} = -\underline{\hat{\mu}} \cdot \underline{B} \quad (2.5)$$

If a dimensionless spin angular momentum operator \hat{I} is defined as the following,

$$I \rightarrow \hbar \hat{I} \quad (2.6)$$

and the applied magnetic field is taken to be aligned with the z -axis, combining Eqn. (2.4), (2.5) and (2.6), finally the Zeeman Hamiltonian is obtained,

$$\hat{H} = -\hbar \gamma B_0 \hat{I}_z \quad (2.7)$$

The eigenvalues of this Hamiltonian are proportional to the eigenvalues of \hat{I}_z . Therefore the energies of a spin in a magnetic field are,

$$E_m = -\hbar \gamma B_0 m_I \quad (2.8)$$

where the spin quantum number $m_I = I, I-1, \dots, -I$. These states are equally spaced and separated by energy $\Delta = \hbar \gamma B_0$, which is known as the Zeeman splitting. For nuclei with spin $I = 3/2$ the Zeeman states are illustrated in Fig. 2.3.

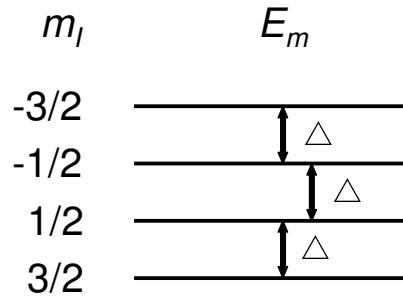


Figure 2.3 Zeeman energy levels for a spin $I = 3/2$ particle

2.3.2. Larmor Precession

As mentioned above, although spin has no classical analogue, in terms of magnetic moment it can be treated classically. When a nuclear spin is subjected to a static magnetic field, the motion of the magnetic moment associated with the spin is governed by,

$$\frac{d\boldsymbol{\mu}}{dt} = \gamma \boldsymbol{\mu} \times \mathbf{B}. \quad (2.9)$$

By convention, the direction of the magnetic field defines the z -direction, then Eqn. (2.9) can be rewritten as follows,

$$\begin{aligned} \frac{d\mu_x}{dt} &= \gamma \mu_y B_z \\ \frac{d\mu_y}{dt} &= -\gamma \mu_x B_z \\ \frac{d\mu_z}{dt} &= 0 \end{aligned} \quad (2.10)$$

The solution is illustrated in Fig 2.4, which shows that the magnetic moment undergoes a precession about the axis of the applied magnetic field at the frequency,

$$\omega_L = \gamma B_z \quad (2.11)$$

which is known as the Larmor frequency. The magnetic moment traces out a precessional cone, with the same angle between the spin axis and the magnetic field. This is called Larmor precession.

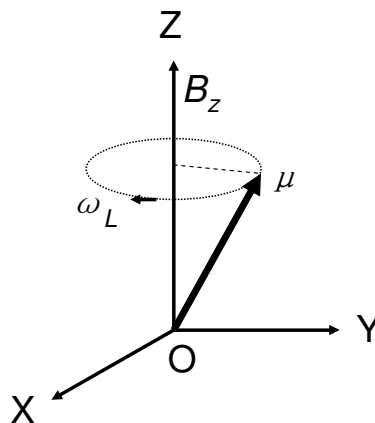


Figure 2.4 Larmor precession of the magnetic moment

It is worth noting that it is not the nucleus physically spinning about the axis, but the direction of the vector of the nuclear spin that varies with time.

2.3.3. *x*-pulse

When a radiofrequency (rf) pulse of angular frequency ω_{rf} is applied, the spin experiences two magnetic fields: a static field generated by the magnet, and an oscillating field from the excitation coil. Normally the static field is many orders of magnitude greater than the

oscillating field. Usually in NMR experiments the rf field irradiated is resonant with the precession of the spin, i.e. $\omega_{rf} = \omega_L$. The rotating rf field will keep up with the spin as it precesses, therefore although the rf field is weak compared with the static field, the influence will accumulate as time goes on. If the pulse is applied for long enough a significant change in the spin state can occur.

Generally the direction of the pulsed rf B -field can be various, however in practise the magnetic field oscillating perpendicular to the static field (x -pulse) is most frequently used and it is the only pulse used in our experiments. Therefore only the x -pulse is introduced here. It should be noted that for convenience this section is discussed in a frame of reference that is rotating about the z -axis, with angular frequency equal to the Larmor frequency ω_L [29].

Assuming the initial spin state is $|\psi\rangle_i$ and the spin state after the pulse is $|\psi\rangle_f$, by integration of the Schrödinger equation, these two states are related by a rotation operator $\hat{R}_x(\beta)$ as the following,

$$|\psi\rangle_f = \hat{R}_x(\beta)|\psi\rangle_i \quad (2.12)$$

where β is called the flip angle of the pulse and is proportional to the amplitude and duration of the pulse; the pulse propagator $\hat{R}_x(\beta)$ has the following matrix form,

$$\hat{R}_x(\beta) = \begin{pmatrix} \cos \frac{1}{2}\beta & -i \sin \frac{1}{2}\beta \\ -i \sin \frac{1}{2}\beta & \cos \frac{1}{2}\beta \end{pmatrix} \quad (2.13)$$

In practise, an rf pulse with a flip angle of 90° is most frequently used. The transformation of the state $|\alpha\rangle$ is,

$$|\alpha\rangle \xrightarrow{\hat{R}_x(90^\circ)} \frac{1}{\sqrt{2}} \begin{pmatrix} 1 & -i \\ -i & 1 \end{pmatrix} \begin{pmatrix} 1 \\ 0 \end{pmatrix} = e^{-i\pi/4} \begin{pmatrix} \frac{1+i}{2} \\ \frac{1-i}{2} \end{pmatrix} = e^{-i\pi/4} | -y \rangle \quad (2.14)$$

The 90° x -pulse transforms the state $|\alpha\rangle$ into the state $| -y \rangle$, i.e. the polarisation of the spin is rotated by 90° about the x -axis.

The influence of an x -pulse is to rotate the magnetic moment about the x -axis through an angle equal to the flip angle of the pulse, β , regardless of the initial state of the spin.

2.3.4 Bloch equations

So far some concepts have been introduced about a single nuclear spin, however real systems consist of many nuclei, therefore it is the macroscopic magnetic properties with the net behaviour of many individual nuclear spins that is of interest.

In the presence of a magnetic field the sample will exhibit a bulk magnetisation M . Considering the Boltzmann distribution, Pierre Curie developed an expression for paramagnetism, which is known as Curie's law [34],

$$M = C \frac{B_z}{T} \quad (2.15)$$

where C is a material-specific Curie constant. Because the magnetisation is proportional to the magnetic field B_z and inversely proportional to temperature T , generally a larger applied magnetic field and a lower temperature will give rise to a larger magnetisation.

The evolution of the bulk magnetisation vector \underline{M} follows the classical equation for a magnetic moment in a magnetic field,

$$\frac{d\underline{M}}{dt} = \gamma \underline{M} \times \underline{B} \quad (2.16)$$

It is similar to the case of a single nuclear spin, but there are some differences between the two cases. For the single nuclear spin the direction of the magnetic moment is quantised, that is, in a discrete number of particular directions depending on its spin quantum number. However in the case of bulk magnetisation, because it is the net magnetisation of a large number of individual spin states populated according to the Boltzmann distribution, it is not quantised. The concept of thermal equilibrium is valid and \underline{M} is always aligned with the magnetic field \underline{B} at thermal equilibrium.

In NMR experiments a 90° pulse can be applied to create a non-equilibrium state of the spin system. Magnetic field fluctuations, arising from molecular motions, such as the rotational motion of methyl groups, play a very important role in driving the system back towards thermal equilibrium. This process can be accounted for by introducing relaxation terms into the equation of motion, Eqn. (2.16). If the equilibrium magnetisation is M_0 , Eqn. (2.16) becomes,

$$\begin{aligned}
\frac{dM_x}{dt} &= \gamma M_y B_z - \frac{M_x}{T_2} \\
\frac{dM_y}{dt} &= -\gamma M_x B_z - \frac{M_y}{T_2} \\
\frac{dM_z}{dt} &= 0 - \frac{M_z - M_0}{T_1}
\end{aligned} \tag{2.17}$$

The expressions in Eqn. (2.17) are known as the Bloch equations, where the second terms of the right-hand side are the relaxation terms. T_1 and T_2 are time constants corresponding to two relaxation processes. T_1 is the spin-lattice relaxation time, and it describes the recovery of the longitudinal magnetisation M_z . This process involves an exchange of energy with the lattice since nuclear spins must be flipped. T_2 is the transverse relaxation time or spin-spin relaxation time, and it governs the recovery of the transverse magnetisation M_x and M_y . This process involves no exchange of energy with the lattice, and it is a redistribution of energy amongst the spins.

2.3.5 Pulsed NMR signal – FID

Usually a resonant 90° x -pulse is applied before the signal acquisition. As discussed above the magnetisation rotates about the x -axis by 90° in response to this pulse. As a result, the state of the system immediately after the pulse is $M_x = 0$, $M_y = M_0$ and $M_z = 0$. The longitudinal magnetisation M_0 is manipulated into the xy -plane. Following this, in the absence of rf irradiation the subsequent evolution of the magnetisation follows the Bloch equations, Eqn. (2.17),

$$\begin{aligned}
M_x &= M_0 \sin(\omega_L t) \exp\left(\frac{-t}{T_2}\right) \\
M_y &= M_0 \cos(\omega_L t) \exp\left(\frac{-t}{T_2}\right) \\
M_z &= M_0 \left[1 - \exp\left(\frac{-t}{T_1}\right)\right]
\end{aligned} \tag{2.18}$$

Therefore, in the xy -plane there is a component of transverse magnetisation precessing about the static magnetic field axis (z -axis) at the Larmor frequency ω_L . The receiver coil has its axis in the xy -plane, typically, along the y -axis. The precession of the transverse magnetisation will induce an electromagnetic field $s(t)$ across the receiver coil. The NMR signal is proportional to M_y ,

$$s(t) \propto M_y = M_0 \cos(\omega_L t) \exp\left(\frac{-t}{T_2}\right). \quad (2.19)$$

This is called the ‘free induction decay (FID)’, and it is illustrated in Fig 2.5. The integrated area of the FID can be measured to obtain information about longitudinal magnetisation of the system.

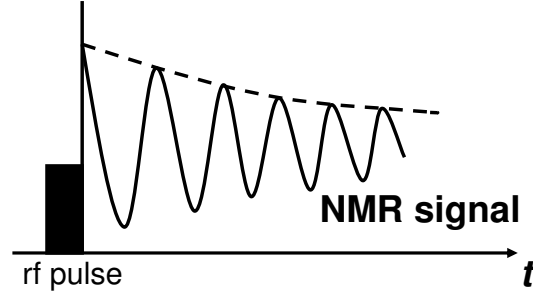


Figure 2.5 rf pulse and the induced NMR signal (FID)

2.3.6 NMR spectrum

Generally it is not convenient to get information from the FID directly, therefore some mathematical operations can be used in order to transform the FID into another form. Combining the first two equations of Eqn. (2.18), a general complex FID signal $s(t)$ is obtained,

$$s(t) = \exp(i\omega_L t) \exp(-t/T_2). \quad (2.20)$$

The transverse components M_x and M_y oscillate at the nuclear Larmor frequency ω_L , and decay with the time constant T_2 . By Fourier transforming Eqn. (2.20) the FID signal $s(t)$ is transformed into the frequency domain,

$$S(\omega) = \int_0^{\infty} s(t) \exp(-i\omega t) dt = \int_0^{\infty} \exp[i(\omega_L - \omega)t] \exp(-t/T_2) dt. \quad (2.21)$$

The real and imaginary parts of $S(\omega)$ are given by,

$$\begin{aligned} \text{Re}[S(\omega)] &= \frac{\lambda}{(\omega - \omega_L)^2 + \lambda^2} \\ \text{Im}[S(\omega)] &= \frac{\omega - \omega_L}{(\omega - \omega_L)^2 + \lambda^2} \end{aligned} \quad (2.22)$$

where $\lambda = 1/T_2$.

The Fourier transform of the FID is called the NMR spectrum. A schematic pattern of the NMR spectrum is demonstrated in Fig. 2.6. The real part of $S(\omega)$ is a Lorentzian peak with half-width at half- maximum amplitude, $\lambda = 1/T_2$.

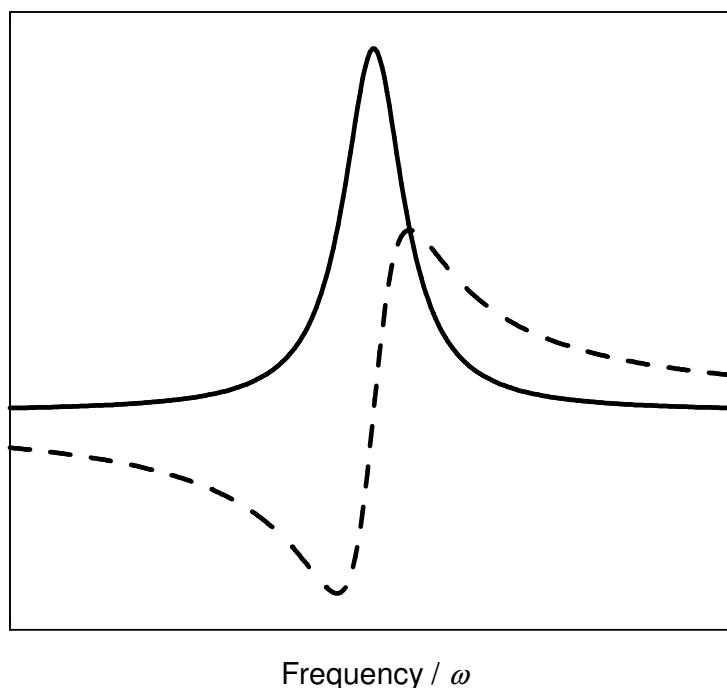


Figure 2.6 Schematic NMR spectrum; real part indicated by the solid line and imaginary part indicated by the dashed line

2.4 Nuclear spin wave functions of the methyl group

Complete wave functions for methyl groups include vibrational, rotational, nuclear spin and electron wave functions. However at low temperature, vibrational wave functions and electron wave functions are in the totally symmetric ground state and hence they need not to be considered in terms of symmetry [20]. Therefore only the rotational wave functions and nuclear spin wave functions need to be considered. The molecular wave functions are constructed from linear combinations of products of rotational and nuclear spin wave functions.

In the methyl group, if the three hydrogen nuclei are numbered 1, 2 and 3, changing the order of numbers arranged in a particular order, as from 123 to 132 , 231 , etc, is called permutation. Odd permutations of two protons (i.e. from 123 to 132 , 213 or 321) require the breaking and forming of the covalent bonds, which need very large energy. However even permutations with rotations (i.e. from 123 to 231 or 312) do not require a breaking or forming of the bonds, so only even permutations need to be considered. As a result the complete wave functions must be totally symmetric (A symmetry). This imposes constraints on the allowable combinations of the rotational and nuclear spin configurations.

The methyl group rotational wave functions have been discussed above and for the ground torsional state, the A and E rotational states are obtained. Transitions that change the symmetry of the rotational wave function also inevitably change the symmetry of the nuclear spin wave functions. Like the rotational wave functions, the nuclear spin wave functions must also transform according to the irreducible representations of the group C_3 . The nuclear spin eigenfunctions of the methyl group may be expressed as $|\psi_S\rangle = |m_I, e\rangle$, where m_I is the nuclear magnetic quantum number and e is the symmetry of the state. Table 2.2 shows the nuclear spin eigenfunctions of the methyl group.

$ 3/2, A\rangle = +++ \rangle$ $ 1/2, A\rangle = \frac{1}{\sqrt{3}} (++-\rangle + +-+\rangle + -++\rangle)$ $ -1/2, A\rangle = \frac{1}{\sqrt{3}} (--+\rangle + --\rangle + +-\rangle)$ $ -3/2, A\rangle = --- \rangle$
$ 1/2, E_a\rangle = \frac{1}{\sqrt{3}} (++-\rangle + \varepsilon +-+\rangle + \varepsilon^* -++\rangle)$ $ -1/2, E_a\rangle = \frac{1}{\sqrt{3}} (--+\rangle + \varepsilon --\rangle + \varepsilon^* +-\rangle)$ $ 1/2, E_b\rangle = \frac{1}{\sqrt{3}} (++-\rangle + \varepsilon^* +-+\rangle + \varepsilon -++\rangle)$ $ -1/2, E_b\rangle = \frac{1}{\sqrt{3}} (-++\rangle + \varepsilon^* --\rangle + \varepsilon +-\rangle)$

Table 2.2 Nuclear spin eigenfunctions of the methyl group; $\varepsilon = \exp(2\pi i/3)$

The complete wave function must have A symmetry as discussed above. Therefore, the allowable symmetry combinations of rotational and nuclear spin eigenfunctions $|\psi_S\rangle$ and $|\psi_R\rangle$ are $|\psi_R^A\rangle|\psi_S^A\rangle$, $|\psi_R^{Ea}\rangle|\psi_S^{Eb}\rangle$ and $|\psi_R^{Eb}\rangle|\psi_S^{Ea}\rangle$. From Table 2.2, it can be identified that each rotational A state with symmetry species $|\psi_R^A\rangle|\psi_S^A\rangle$ is a nuclear spin 3/2 quartet, while the rotational E states with symmetry species $|\psi_R^{Ea}\rangle|\psi_S^{Eb}\rangle$ and $|\psi_R^{Eb}\rangle|\psi_S^{Ea}\rangle$ are nuclear spin 1/2 doublets. When a static magnetic field is applied, these manifolds exhibit the expected pattern of Zeeman splitting as illustrated in Fig. 2.7.

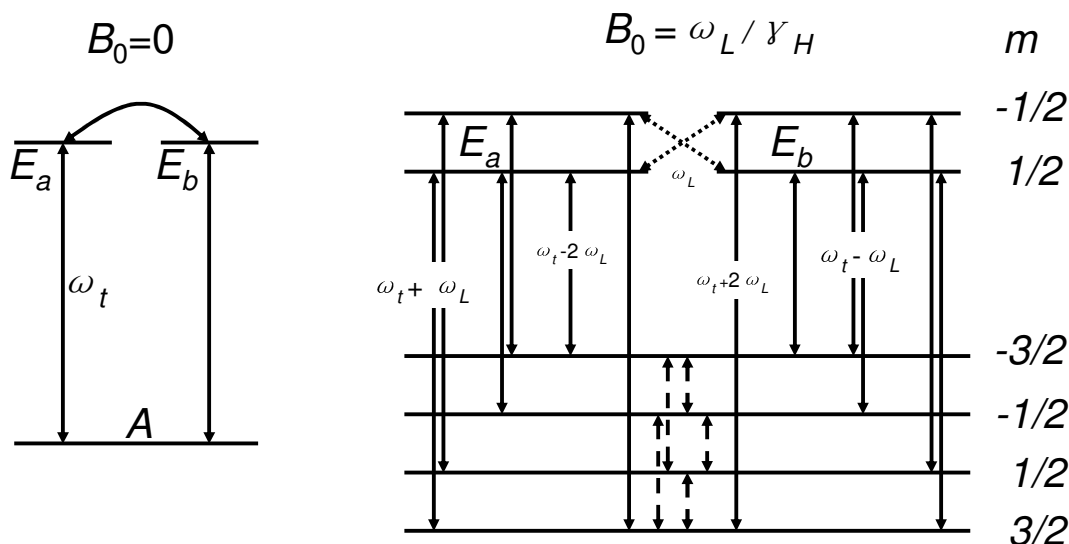


Figure 2.7 Zeeman splittings of the ground torsional state of the methyl group under an applied magnetic field B_0 ; ω_L is the ^1H Larmor frequency and ω_t is the methyl tunnelling frequency

2.5 Methyl group thermodynamics

Associated with the rotational motion of the methyl group, two types of nuclear relaxation can occur [14]. Transitions at angular frequencies $\omega_t + \omega_L$, $\omega_t - \omega_L$, $\omega_t + 2\omega_L$ and $\omega_t - 2\omega_L$ have symmetry changes from A to E type (solid arrows in Fig. 2.7). These transitions all have the tunnelling frequency ω_t as the important energy difference. However transitions from E_a to E_b have the Larmor frequency ω_L as the important energy difference (dashed arrows). Whether transitions occur from A to E , or from E_a to E_b , these nuclear relaxations are associated with a change in symmetry.

Considering the fact that rotational states with A symmetry are nuclear spin $3/2$ quartets, while the rotational states with E symmetry are nuclear spin $1/2$ doublets, the conversion of a rotational state of A symmetry into one of E symmetry involves the change in the spin state simultaneously with the change in the tunnelling state. Therefore the A - E conversion process requires an interaction that couples both spatial and spin degrees of freedom (solid arrows in Fig. 2.7), and the relaxations between the A and E rotational states are very slow. On the other hand, the conversion between A - A (dashed arrows) and E - E require no change in terms of spin degrees of freedom. Consequently, the probability of A - A and E - E conversion is much larger than that of A - E conversion. The relaxations within A or E rotational states are so fast that the torsional states are usually at thermal equilibrium with the lattice.

At low temperature (e.g. $T = 4\text{K}$), $k_B T$ is small compared with the torsional splittings, therefore only the ground torsional state is occupied. Because the A - E conversion is inefficient, the populations of the ground tunnelling states have a very slow response to any changes in the lattice temperature. At low temperature, the A - E conversion time could be as long as many days or weeks.

The populations of the A state and E states can be interpreted by a tunnelling temperature θ_t , and they are governed by,

$$\frac{P(E)}{P(A)} = \exp(-\beta_t \omega_t) \approx 1 - \beta_t \omega_t \quad (2.23)$$

where $P(E)$ and $P(A)$ are the populations of the A and E states, respectively. $\beta_t = \hbar/k_B \theta_t$ is the inverse tunnelling temperature, and ω_t is the tunnelling frequency that is determined by the ground state tunnelling splitting. Associated with the inverse tunnelling temperature, a tunnelling reservoir can be defined, illustrated in Fig. 2.8. Another thermal reservoir, the Zeeman reservoir associated with the inverse Zeeman temperature β_z is defined in a similar way. Usually the magnetic resonance behaviour of the methyl group may be described in terms of Fig. 2.8. The inefficiency of A - E transitions at low temperature means that the tunnelling reservoir may be relatively isolated from the lattice.

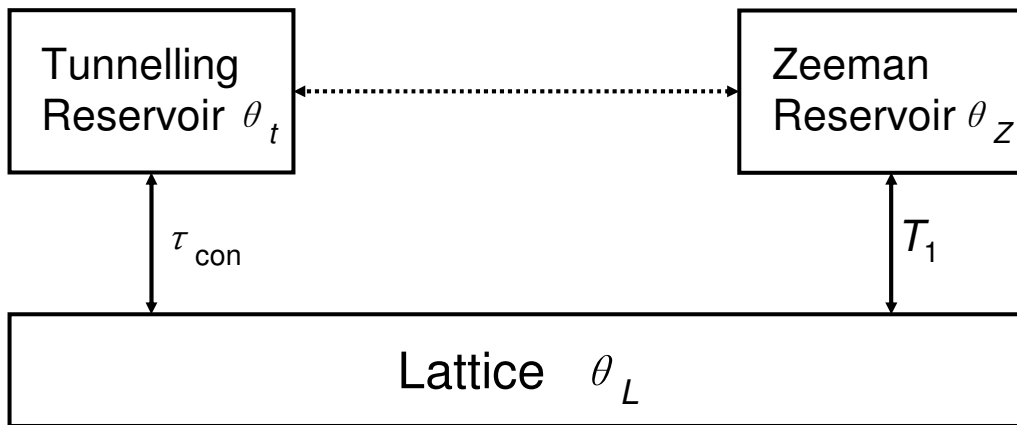


Figure 2.8 Schematic interpretation of methyl group thermodynamics in terms of thermal reservoirs associated with tunnelling and Zeeman energy; T_1 is the spin-lattice relaxation time and τ_{con} is the A - E conversion time constant; the tunnelling reservoir and the Zeeman reservoir can be coupled under the tunnel resonance conditions [6]

2.6 Correlation times and the Haupt equation

2.6.1 Correlation times

In the solid state the motion of atoms and molecules takes place under the influence of a hindering potential. For simplicity, a potential comprising two wells is considered here, as illustrated in Fig. 2.9

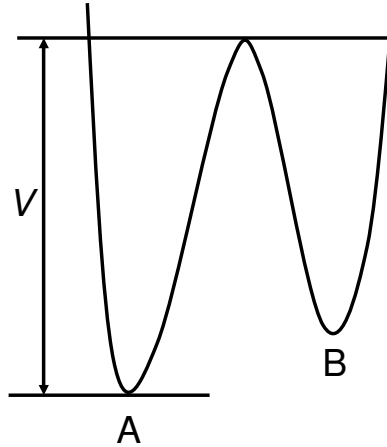


Figure 2.9 Schematic diagram of two potential wells

In order for a particular particle to hop from site A to site B, it requires sufficient energy to overcome the potential barrier of height V . Normally the motion can be characterised by a hopping rate between the wells. If τ_0^{-1} is denoted as the attempt frequency, classically speaking it can be interpreted that how often it attempts hopping over the potential barrier. Because of the interceding barrier only particles with an energy greater than the potential barrier are able to hop over. The fraction of particles follows a Boltzmann factor therefore the hopping rate τ_c^{-1} is obtained and it follows the well known Arrhenius rate law,

$$\tau_c^{-1} = \tau_0^{-1} \exp\left(-\frac{E_{act}}{k_B T}\right). \quad (2.24)$$

The time τ_c is called the correlation time and it defines the mean residence time in a potential well between hops. E_{act} is the activation energy, and it is less than the barrier height V due to the quantum tunnelling effect.

2.6.2 Correlation function

Hopping processes are random, statistical events (stochastic). Therefore, the motion can be characterised in terms of a correlation function. It is assumed that the correlation function follows the monoexponential form,

$$G(\tau) = C \times \exp\left(\frac{-|\tau|}{\tau_c}\right) \quad (2.25)$$

where C is a constant. Experimental evidence from field-cycling NMR relaxometry will later support this assumption. Eqn. (2.25) represents how quickly the system will forget its previous state, having the timescale of τ_c . Apparently the correlation function $G(\tau)$ describes the motion of the system.

The correlation function $G(\tau)$ is in the time domain. Usually it is more convenient for the dynamics to be represented in the frequency domain. This can be obtained by Fourier transforming the correlation function,

$$J(\omega) = \int_{-\infty}^{\infty} G(\tau) \exp(-i\omega\tau) d\tau = C \int_{-\infty}^{\infty} \exp\left(\frac{(-i\omega\tau_c - 1)}{\tau_c} \tau\right) d\tau. \quad (2.26)$$

Therefore,

$$J(\omega) = C \times \frac{\tau_c}{1 + \omega^2 \tau_c^2} \quad (2.27)$$

$J(\omega)$ is a Lorentzian function with half-width at half-maximum amplitude equal to the inverse correlation time τ_c^{-1} , and it describes the motion in the frequency domain, therefore it is called the motional spectrum, or often the spectral density.

2.6.3 Spin-lattice relaxation

In this section, the link between the spin-lattice relaxation time T_1 and molecular dynamics of the system will be established, by relating T_1 to the spectral density function.

Fluctuating magnetic fields play a crucial role in the recovery of magnetisation. Transitions in the spin states are inevitably involved in the recovery of magnetisation. Consider a two spin-state system (Fig. 2.10),

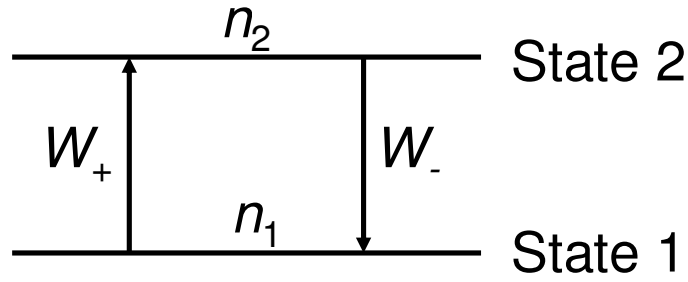


Figure 2.10 Schematic diagram of a two spin-state system

n_1 and n_2 are the populations of the two states, and W_+ and W_- are the transition probabilities per unit time between the two spin states, the population change is,

$$\frac{dn}{dt} = 2W_-n_2 - 2W_+n_1. \quad (2.28)$$

Denote $N = n_1 + n_2$ and $n = n_1 - n_2$ then,

$$\frac{dn}{dt} = N(W_- - W_+) - n(W_- + W_+). \quad (2.29)$$

Let $W = \frac{W_- + W_+}{2}$ and $n_0 = N \frac{W_- - W_+}{W_- + W_+}$, then,

$$\frac{dn}{dt} = 2W(n_0 - n). \quad (2.30)$$

The solution is,

$$n = n_0 + A \exp(-2Wt) \quad (2.31)$$

where A is a constant. The longitudinal magnetisation is proportional to the population difference, i.e. $M_z \propto n$, and the magnetisation at thermal equilibrium M_0 is proportional to

$n_0 = N \frac{W_- - W_+}{W_- + W_+}$, thus Eqn. (2.31) is rewritten as,

$$M_z = M_0 [1 - \exp(-2Wt)]. \quad (2.32)$$

By comparing Eqn. (2.18) and (2.32), it is clear that,

$$T_1^{-1} = 2W. \quad (2.33)$$

The transition probability is related to the motional spectrum by the following [14],

$$W = C_1 \times J(\omega) = C_2 \frac{\tau_c}{1 + \omega^2 \tau_c^2}. \quad (2.34)$$

Combining Eqn. (2.33) and (2.34), the T_1 expression is obtained as,

$$T_1^{-1} = C_0 \frac{\tau_c}{1 + \omega^2 \tau_c^2}. \quad (2.35)$$

Above, the transitions were assumed to be driven by a fluctuating magnetic field. In reality, these transitions are driven by the time-dependent dipole-dipole interaction between nuclei, which can be caused by molecular motions. Consider a system of two interacting spins I and S , the Hamiltonian for the dipole-dipole interaction between them may be written as,

$$\begin{aligned} \hat{H}_{DD} &= \text{Const} \times [A + B + C + D + E + F] \\ A &= \hat{I}_z \hat{S}_z (3 \cos^2 \theta - 1) \\ B &= -\frac{1}{4} [\hat{I}_+ \hat{S}_- + \hat{I}_- \hat{S}_+] (3 \cos^2 \theta - 1) \\ C &= \frac{3}{2} [\hat{I}_z \hat{S}_+ + \hat{I}_+ \hat{S}_z] \sin \theta \cos \theta \exp(-i\phi) \\ D &= \frac{3}{2} [\hat{I}_z \hat{S}_- + \hat{I}_- \hat{S}_z] \sin \theta \cos \theta \exp(+i\phi) \\ E &= \frac{3}{4} \hat{I}_+ \hat{S}_+ \sin^2 \theta \exp(-2i\phi) \\ F &= \frac{3}{4} \hat{I}_- \hat{S}_- \sin^2 \theta \exp(+2i\phi) \end{aligned} \quad (2.36)$$

where the internuclear vector between spins I and S is defined by the spherical polar coordinates (r, θ, ϕ) . Considering a homonuclear system, terms A and B describe a process with zero net change in spin polarisation, whereas spin-operators C and D cause single quantum transitions with an energy of $\hbar\omega_L$, wherein the transition probability W_1 is,

$$W_1 = C_1 \times J_1(\omega_L) = C_2 \frac{\tau_c}{1 + \omega_L^2 \tau_c^2} \quad (2.37)$$

and spin-operators E and F induce double quantum transitions with an energy of $2\hbar\omega_L$, and the corresponding transition probability W_2 is,

$$W_2 = C_1 \times J_2(2\omega_L) = C_2 \frac{4\tau_c}{1 + 4\omega_L^2 \tau_c^2}. \quad (2.38)$$

The inverse spin-lattice relaxation time T_1^{-1} is obtained by a summation over the various transitions,

$$T_1^{-1} = 2(W_1 + W_2). \quad (2.39)$$

Therefore T_1 can be related to the transition probability of the spin states that is mainly governed by the molecular motions as,

$$T_1^{-1} = C_D \left(\frac{\tau_c}{1 + \omega_L^2 \tau_c^2} + \frac{4\tau_c}{1 + 4\omega_L^2 \tau_c^2} \right) \quad (2.40)$$

where the dipolar constant C_D is a function of the geometrical factor in Eqn. (2.36), determined by the internuclear distance and angle with respect to the applied field.

2.6.4 Haupt equation for the methyl group

The rotation of a methyl group causes the dipolar Hamiltonian (Eqn. (2.36)) to be time-dependent, thereby influencing the spin relaxation. The dipolar Hamiltonian may be resolved into two components [14]: an intra-molecular and an inter-molecular contribution. The intra-molecular contribution is due to the interactions within an isolated methyl group whereas the intermolecular contribution is due to the interactions with other protons of the molecule and with protons of different molecules. The nonzero matrix elements of the intra-molecular dipolar Hamiltonian (solid arrows in Fig. 2.7) give rise to transitions at angular frequencies $\omega_i + \omega_L$, $\omega_i - \omega_L$, $\omega_i + 2\omega_L$, and $\omega_i - 2\omega_L$, respectively; these introduce changes in tunnelling state. Transitions within E states (dotted arrows in Fig. 2.7) also occur when the inter-molecular dipolar Hamiltonian is considered, with the influence of one-spin and two-spin operators, this causes nonzero transition probabilities at angular frequencies ω_L and $2\omega_L$. The inverse spin-lattice relaxation time T_1^{-1} is obtained by a summation over the various transitions. By evaluating the transition probabilities, Haupt [12] developed the following expression,

$$\begin{aligned} T_1^{-1} &= (T_1^{-1})_{AE} + (T_1^{-1})_{EE} \\ &= W_{AE} + W_{EE} \\ &= C_{AE} [J(\omega_i + \omega_L) + J(\omega_i - \omega_L) + J(\omega_i + 2\omega_L) + J(\omega_i - 2\omega_L)] \\ &\quad + C_{EE} [J(\omega_L) + J(2\omega_L)] \\ &= C_{AE} \sum_{n=-2}^2 \frac{n^2 \tau_c}{1 + (\omega_i + n\omega_L)^2 \tau_c^2} + C_{EE} \sum_{n=1}^2 \frac{n^2 \tau_c}{1 + n^2 \omega_L^2 \tau_c^2} \end{aligned} \quad (2.41)$$

The second term on the right-hand side is the familiar Bloembergen, Purcell, Pound (BPP) term [8] arising from incoherent pseudo-classical barrier hopping with the correlation time τ_c . C_{EE} is the inter-molecular dipolar constant. The first term on the right-hand side describes resonant features that appear in the field-dependent T_1^{-1} data when $\omega_i = \pm n\omega_L$. The spin symmetry species A and E of the methyl group have the energy splitting $\hbar\omega_i$ in the ground state. C_{AE} is the intra-molecular dipolar constant that arises from those time-dependent dipolar interactions that have the correct symmetry to convert the spin-symmetry species of the

methyl group. The factor $n = 1, 2$ relates to the transitions involving changes in magnetic quantum number $\Delta m = \pm 1$ and $\Delta m = \pm 2$, respectively, and these are mediated by the one-spin and two-spin operators of the dipolar interaction as defined in Ref. [4].

2.6.5 Rate equations in ESR tunnel resonance

The phenomenon of ESR tunnel resonance is used to investigate methyl tunnelling. Therefore in this section we shall introduce the theory determining the interaction between an electron spin and the protons of a tunnelling methyl group.

In section 2.6.4 above, the nuclear spin relaxation mediated by the time-dependent dipole-dipole interaction between nuclei has been shown. Similarly in methyl-group systems with unpaired electrons or free radicals, the nuclear spin relaxation can be influenced by the time-dependent dipole-dipole interaction between electrons and methyl protons. In this section, rate equations for the proton polarisation $\langle I_z \rangle$ and evolutions of methyl tunnelling temperature θ_i will be discussed.

Firstly we denote \underline{r} as the vector from the unpaired electron to the centre of the triangle of methyl protons. The vectors $\underline{r}_i = \underline{r} + \underline{\delta}_i$, $i = 1, 2, 3$, define the positions of the three protons. For simplicity, the three nuclear spin operators \hat{I}_1 , \hat{I}_2 and \hat{I}_3 , may be combined to form basis functions belonging to irreducible representations of the group of cyclic permutations [17],

$$\hat{I}^\lambda = \hat{I}_1 + \lambda \hat{I}_2 + \lambda^* \hat{I}_3 \quad (2.42)$$

where $\lambda = 1, \varepsilon, \varepsilon^*$, with $\varepsilon = \exp(2\pi i/3)$. The operator \hat{P} is introduced to achieve the effect of cyclically permuting the three spin coordinates,

$$\hat{P} \hat{I}^\lambda = \lambda \hat{I}^\lambda \hat{P}. \quad (2.43)$$

The dipolar Hamiltonian \hat{H}_d for the dipole-dipole interaction between the unpaired electron and methyl protons is [35],

$$\hat{H}_d = D r^3 \sum_{i=1}^3 \left[r_i^{-5} (\hat{S} \cdot \underline{r}_i) (\hat{I}_i \cdot \underline{r}_i) - \frac{1}{3} r_i^{-3} (\hat{S} \cdot \hat{I}_i) \right] \quad (2.44)$$

where $D = \hbar g \beta \gamma r^{-3}$ is the strength of the dipolar interaction, and \hat{S} is the electron spin operator.

Under the influence of the dipolar Hamiltonian \hat{H}_d , the density matrix may be approximated at high temperature to be [17],

$$\rho = 1 - k_B^{-1} \theta_L^{-1} \hat{H}_r + k_B^{-1} \theta_Z^{-1} \hbar \omega_n \hat{I}_Z^1 + \frac{1}{3} k_B^{-1} \theta_i^{-1} \hbar \omega_i (\hat{P} + \hat{P}^{-1}) \quad (2.45)$$

where θ_L , θ_Z , θ_t are temperatures of the lattice, nuclear Zeeman reservoir and methyl tunnelling reservoir, respectively. ω_n and ω_t are the nuclear Larmor frequency and tunnelling frequency, respectively. \hat{H}_r is the Hamiltonian for free radicals [35].

By evaluating the following equation [17],

$$\frac{d}{dt}\langle I_0^1 \rangle = \text{Tr}\left(I_0^1 \frac{d\rho}{dt}\right) / \text{Tr}(1) \quad (2.46)$$

the change in the nuclear magnetisation, which is induced as a by-product of the relaxation of tunnelling energy mediated by electron-nuclear dipole-dipole interaction, can be obtained as [17],

$$\frac{d}{dt}\langle I_0^1 \rangle = a(\theta_L^{-1} - \theta_t^{-1})\left[W^{(-)}g(\omega_s - \omega_t - \omega_n) - W^{(+)}g(\omega_s - \omega_t + \omega_n)\right] \quad (2.47)$$

where a is a constant, and ω_s is the electron spin Larmor frequency. $g(\omega_s - \omega_t \pm \omega_n)$ is the normalised ESR spectrum of the system. $W^{(-)}$ and $W^{(+)}$ are transition probabilities per unit time; tunnel resonance occurs when $\omega_s = \omega_t \pm \omega_n$, and the transitions are mediated by the time-dependent electron-nuclear dipole-dipole interaction.

Similarly, by considering,

$$\frac{d}{dt}\text{Tr}[\rho(P + P^{-1})] = \text{Tr}\left[\frac{d\rho}{dt}(P + P^{-1})\right] \quad (2.48)$$

the rate equation for the inverse tunnelling temperature θ_t^{-1} can be obtained as follows [17],

$$\begin{aligned} \frac{d}{dt}(\theta_L^{-1} - \theta_t^{-1}) &= -a_t(\theta_L^{-1} - \theta_t^{-1}) \\ &\times \left[W^{(-)}g(\omega_s - \omega_t - \omega_n) + W^{(+)}g(\omega_s - \omega_t + \omega_n) + W^{(0)}g(\omega_s - \omega_t)\right] \end{aligned} \quad (2.49)$$

where a_t is a constant. $W^{(0)}$ is the transition probability per unit time when $\omega_s = \omega_t$. Here the tunnelling temperature will change at the tunnel resonance condition (i.e. $\omega_s = \omega_t$), but it will not cause the nuclear magnetisation to change (Eqn. 2.47) since no nuclear spin flip is involved.

Chapter 3 Experimental

3.1 Introduction

The vast majority of NMR spectrometers are fixed magnetic field instruments whereby only experiments at a particular magnetic field can be performed. However in many cases, it is desirable to conduct NMR experiments over a wide range of fields (e.g. to map out the spectral density directly). Field-cycling NMR is a powerful technique that enables field-dependent measurements, and this approach has been adopted by our laboratory [4, 36–39].

The Nottingham field-cycling NMR spectrometer has a magnetic field switching rate of 10T/s in the range of magnetic field 0–2.5T. Further, a built-in cryostat provides a wide temperature range 4–325K. Therefore it is able to investigate the magnetic field dependence of the spin-lattice relaxation rate T_1^{-1} in very broad ranges of both the magnetic field B and temperature T . With the broad dynamical spectrum measured using the field-cycling NMR spectrometer, the dynamic properties of a wide range of systems and molecules have been studied (e.g. quantum tunnelling of methyl groups [4] and proton transfer in the hydrogen bond [40]).

A variety of NMR pulse sequences have been designed for different NMR experiments whereby the molecular dynamics and methyl thermodynamics can be revealed in many ways. Additionally the NTNMR software, which is associated with the TecMag NMR spectrometer based on the Windows NT system, allows us to design many intricate pulse sequences. By using the Visual Basic computer language to control the NTNMR software, complete automation of the field-cycling spectrometer has been achieved.

In this chapter, firstly the experimental details of the Nottingham field-cycling spectrometer will be discussed. The pulse sequences utilised will then be reviewed and typical experimental data will be presented. Finally the software that enables automation of the experiments and simulation of results will be introduced.

3.2 Field-cycling NMR spectrometer

All experiments have been conducted using the Nottingham field-cycling NMR spectrometer. The radiofrequency (rf) electronics comprise a TecMag Apollo NMR console, a MITEQ

low-noise pre-amplifier and an AMT 1kW rf pulse amplifier. The magnet system is custom-built and possesses a very low inductance superconducting solenoidal magnet which is housed in a liquid helium bath cryostat. The magnet is permanently connected to its d.c. power supply and the magnetic field experienced by the sample is proportional to the instantaneous current. A variable temperature cryostat for the sample is incorporated into the magnet system which uses liquid helium as the cooling fluid, drawn from the main bath via a needle valve and capillary. The NMR probe has a solenoidal rf coil and this forms part of a tank circuit tuned to the chosen NMR measurement frequency, in our case, 36.8MHz. Sample temperatures are measured using the calibrated Cernox resistance thermometer and are controlled by a LakeShore 331 temperature controller with a resistive heater in a feedback loop.

3.2.1 Magnet and magnet power supply

To achieve the purpose of rapid field cycling and a high magnetic field, a superconducting magnet has been designed with a very low inductance (23mH) superconducting solenoid. Compared with conventional static field NMR magnets that operate in persistent mode, the superconducting solenoid in our field-cycling NMR system has no persistent mode switch and must be permanently connected to an external d.c. magnet power supply by leads. In our system, a CRYOGENIC magnet power supply is employed. It operates at a nominal voltage of 15V and is able to supply a maximum current of 160A. The magnetic field experienced by the sample is proportional to the instantaneous current so that the maximum magnetic field available is 2.5T. With a very low inductance superconducting solenoid and a fast ramping magnet power supply, our system has been designed to achieve the rapid field switches of 10T/s.

3.2.2 Cryostat

As illustrated in Fig. 3.1, the superconducting magnet is situated in a liquid helium bath cryostat with a minimum temperature of 4.2K. The liquid helium reservoir is insulated by a large reservoir of liquid nitrogen (77K). The two reservoirs are separated from each other, and from the outside environment, by high vacuum layers ($< 10^{-6}$ torr) which effectively reduce the heat exchanges between different baths. A variable temperature insert (VTI), which uses liquid helium as the cooling fluid, drawn from the main liquid helium bath via a needle valve and capillary, is housed inside the sample space to provide a variable temperature environment for the sample. A resistive heater controlled by the LakeShore 331 temperature controller is employed to stabilise the temperature of the sample. Sample temperatures can be

adjusted in the range $4.2\text{K} < T < 300\text{K}$. Thermal stability is better than 0.05K at low temperatures.

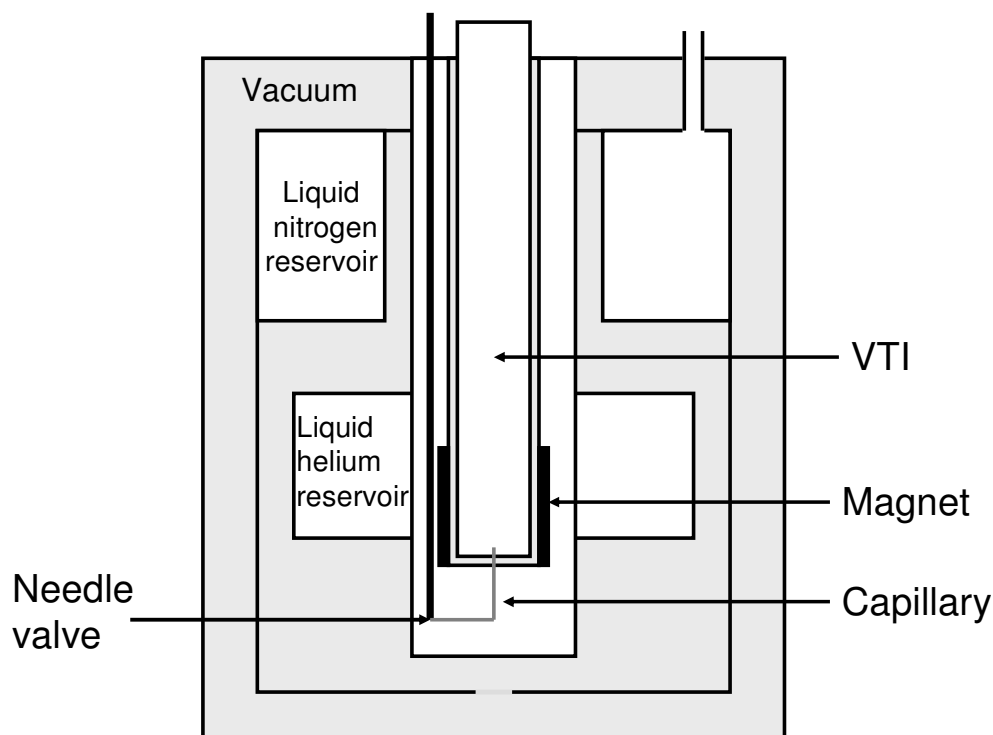


Figure 3.1 Schematic diagram of the magnet and cryostat

3.2.3 Spectrometer

First the operation of the NMR spectrometer (Fig. 3.2) is described by tracing the rf pulse and the NMR signal, and this is followed by a detailed discussion of the key components of our system.

Two radiofrequency waves are generated by the synthesizer (1) at angular frequencies ω_i and $\omega_i + \omega_{\text{ref}}$, where ω_{ref} is called the carrier frequency and it is set to match the Larmor frequency ω_L in the majority of cases. ω_i is known as the intermediate frequency which is fixed at a value of tens of MHz. The two waveforms are combined in the mixer (2), and an rf wave at a single frequency ω_{ref} is obtained. Pulses of rf waves of a finite duration and angular frequency ω_{ref} are created by the pulse gate (3), controlled by the pulse programmer (4). The rf pulse is diverted into the probe through the duplexer (6) after enhancement by the AMT 1kW amplifier (5). In the presence of the magnetic field applied by the magnet, an NMR signal (FID) is induced. The NMR signal is diverted towards the receiver section of the spectrometer by the duplexer (6). The signal is enhanced by the MITEQ preamplifier (7) and then combined with a radiofrequency wave of angular frequency $\omega_i + \omega_{\text{ref}}$ in the mixer (8). The

frequency of the FID is shifted to $\omega_i + \Omega_L$, where the relative Larmor frequency $\Omega_L = \omega_{\text{ref}} - \omega_L$. The FID then passes through a narrow-band amplifier (9), and its frequency is then down-shifted to Ω_L (~MHz) by the mixer (10). The signal is then ready to be recorded by the quadrature receiver (11) and ADCs (12).

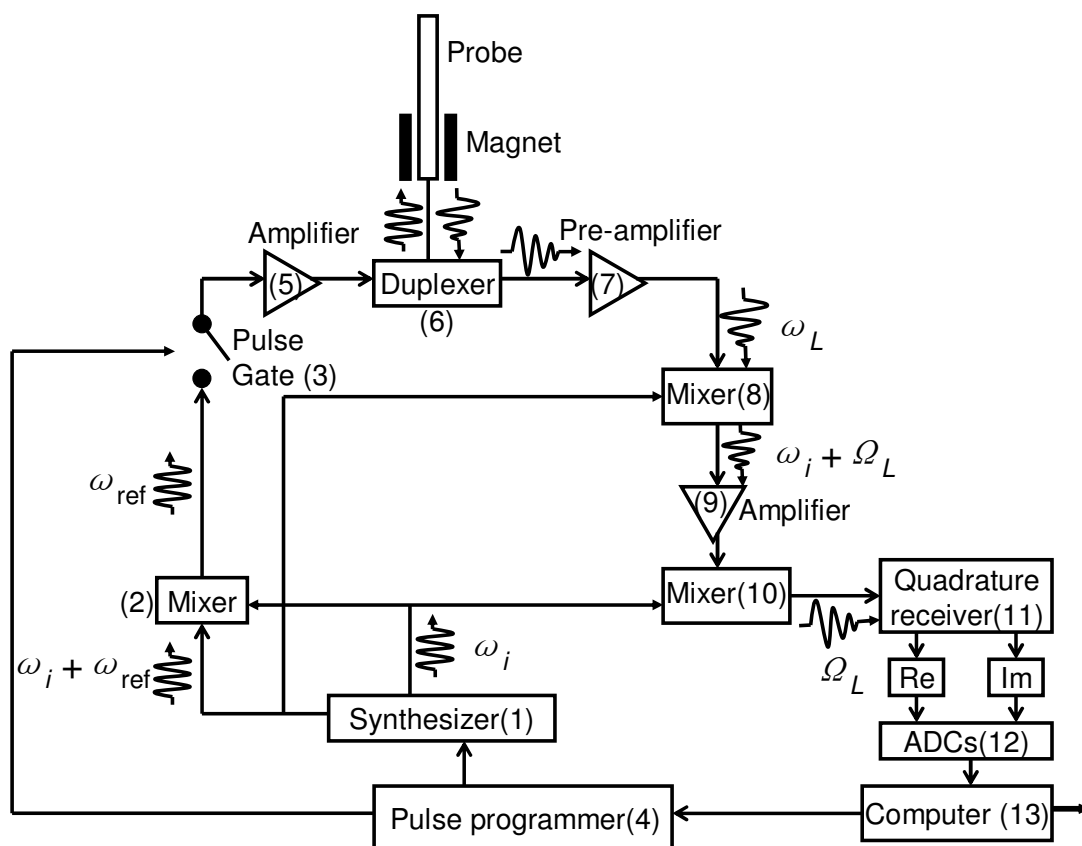


Figure 3.2 Schematic overview of the heterodyne NMR spectrometer

3.2.4 Apollo NMR Console

In our field-cycling NMR system, an Apollo NMR Console manufactured by TecMag is employed. It mainly consists of two rf transmitters and an integrated pulse programmer. One transmitter is used to generate the resonant rf pulse, and the principle of the resonant rf pulse transmitter has been discussed above. The resonant rf pulse is then amplified by the AMT 1kW rf amplifier that can amplify the signal at a frequency in the range 10–150MHz. Another transmitter is used to generate a secondary rf irradiation, which has a very wide range of frequency 5kHz–450MHz, amplified by a broadband AR CW amplifier that has a power of 100W. The secondary rf irradiation is only applied in some specific experiments (e.g. low-field dipole-dipole driven experiments).

3.2.5 Duplexer

The rf pulse generated by the transmitter is a large signal whereas the NMR signal generated by the sample is much smaller [29]. Because it is the same rf coil mounted in the probe that is used in both transmitting rf pulses to the sample and detecting the oscillating NMR signal, in order to distinguish these two different oscillating signals, a duplexer is employed between the transmitter, the receiver and the coil.

The essential elements in the duplexer are the crossed silicon diodes (Fig. 3.3). The crossed diodes operate as a good conductor to a large signal whereas they are a poor conductor to a very small signal.

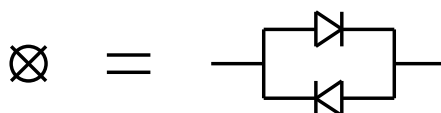


Figure 3.3 Schematic diagram of the crossed diodes

The duplexer has the ability to distinguish different signals, diverting the strong rf pulse to the sample and the small NMR signal to the receiver. The duplexer circuit is illustrated in Fig. 3.4.

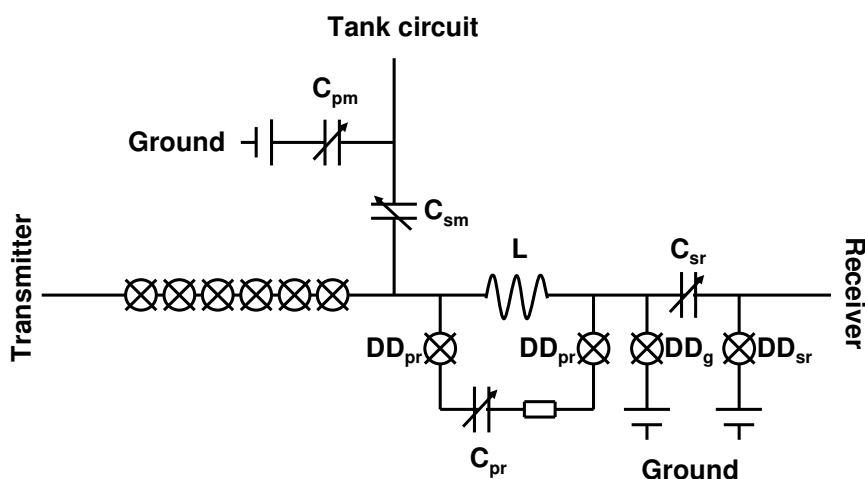


Figure 3.4 Schematic diagram of the duplexer circuit

The transmitted rf pulse is a high voltage (hundreds of volts) signal. Compared with the impedance of the NMR probe tank circuit, the parallel LC_{pr} resonant circuit has a much higher impedance. Therefore the receiver is protected from the high voltage signal, and the rf pulse is diverted to the sample. The crossed diodes DD_g and DD_{sr} provide further protection for the

receiver since any fraction of the transmitted rf pulse that may break through the parallel LC_{pr} circuit, will be diverted to earth. The induced NMR signal is a low voltage ($\sim mV$) signal. The six crossed diodes in series isolate the NMR signal from the transmitter, and minimise the breakthrough of noise from the transmitter. The crossed diodes DD_{pr} , DD_g and DD_{sr} ensure that the NMR signal is diverted into the receiver through the series LC_{sr} resonant circuit. Additionally, the duplexer is matched to the 50Ω impedance of the co-axial rf line by adjustment of the variable matching capacitors C_{sm} and C_{pm} .

3.2.6 Probe

An NMR probe is designed to locate the sample in the centre of the superconducting magnet where there is a homogeneous magnetic field. It also allows the rf pulse to irradiate the sample as well as detection of the induced oscillating NMR signal. Additionally it is able to control the temperature of the sample. Therefore our NMR probe comprises a tank circuit including a resonant rf coil, a secondary rf coil, a wire heater and a thermometer. The picture of the NMR probe is shown in Fig. 3.5.

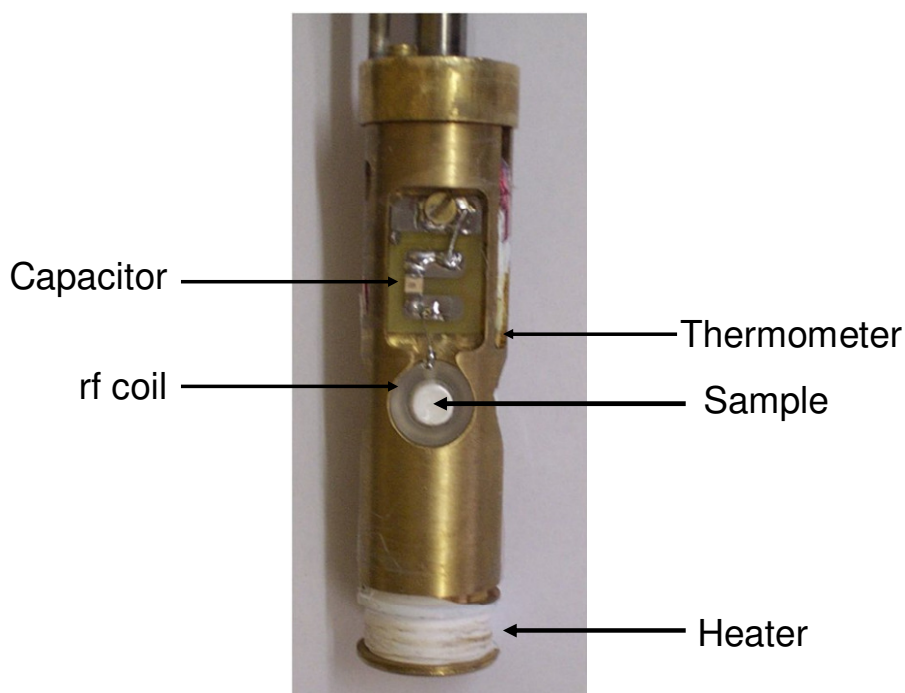


Figure 3.5 Picture of the NMR probe

There is a 5mm diameter bore in the probe, where a glass NMR tube containing the sample is placed. The rf coil is made by winding wire tightly on a KEL-F former. Connecting this rf coil and a capacitor forms a tank circuit with a well defined resonant frequency.

In the probe a series tank circuit is used, and the configuration is illustrated in Fig. 3.6. It comprises an rf coil and two capacitors: the tuning capacitor C_T and the matching capacitor C_M . The tuning capacitor changes the resonant frequency of the rf coil and enhances the current in the coil by electromagnetic resonance, whereas the matching capacitor matches the impedance of the loaded probe to that of the 50 Ω cable coming from the spectrometer. The series configuration gives rise to a broad frequency response about the resonant frequency (i.e. lower Q -factor). The broad frequency response is beneficial in our field-cycling NMR experiments since a broad frequency dependence is required to minimise the effect due to field drifts. The disadvantage of reduced sensitivity is not a major issue in our ^1H NMR experiments where ^1H is abundant.

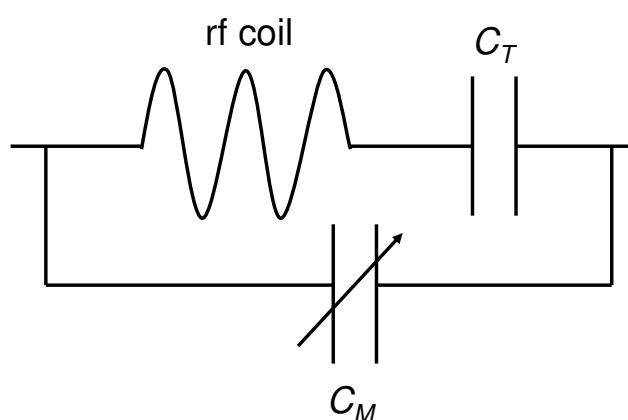


Figure 3.6 Schematic diagram of the series tank circuit

For practical reasons the matching capacitor is placed outside the cryostat, connected with the rf coil by a 50 Ω semi-rigid coaxial rf line of approximate length 1m. The resonant frequency is determined by the inductance L of the rf coil and the capacitance of the tuning capacitor C_T ,

$$\nu = \frac{1}{2\pi\sqrt{LC_T}}. \quad (3.1)$$

In our experiments, the probe was designed with a resonant frequency $\nu = 36.8\text{MHz}$.

In addition to the resonant rf coil, a secondary rf coil has been incorporated into the probe for the purpose of low-field NMR experiments. It is placed perpendicular to the resonant rf coil on both sides. In order to minimise the noise introduced down the cable during the secondary rf irradiation in the low-field NMR experiments, a relay is introduced between the coil and the transmitter. The relay is switched on under digital logic control of the pulse programmer only during sample irradiation.

A resistive heater is mounted at the bottom of the probe to control the temperature of the sample. Additionally, a calibrated CERNOX resistance thermometer is placed next to the sample bore in good thermal contact with the sample whereby a temperature range 4K to 325K can be measured.

3.2.7 Receiver

A schematic diagram of the quadrature receiver is illustrated in Fig. 3.7.

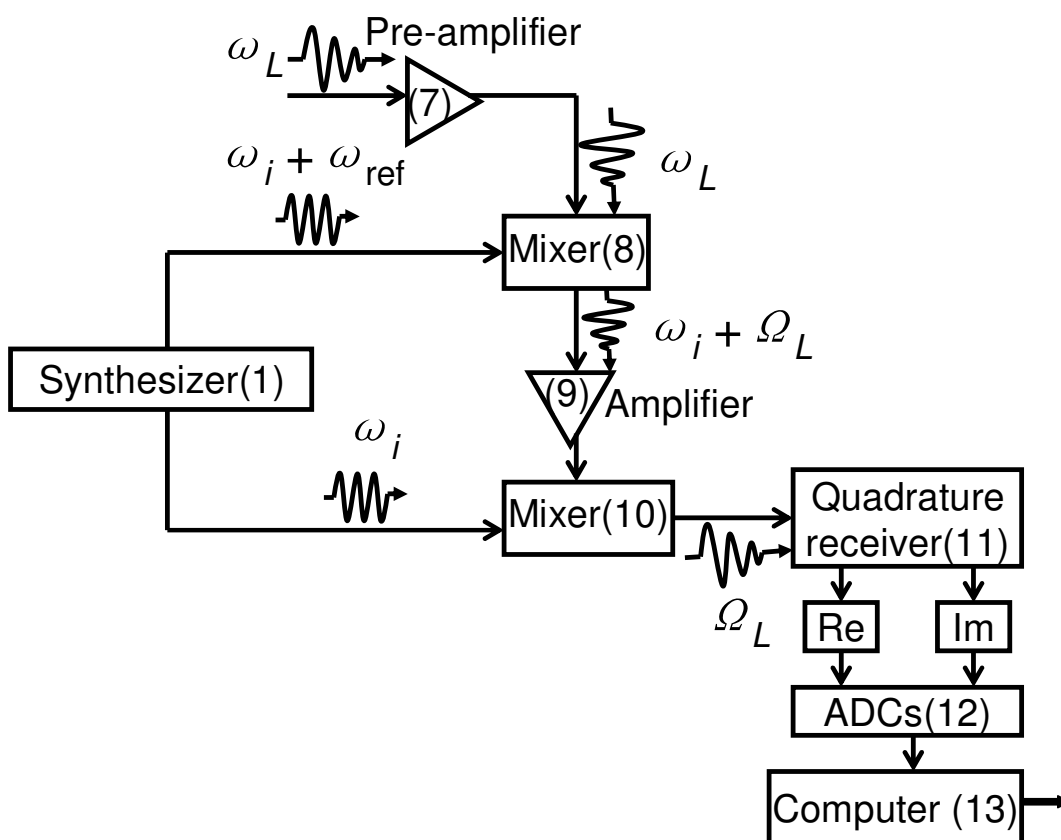


Figure 3.7 Schematic diagram of the quadrature receiver

Before the radiofrequency NMR signal is diverted to the receiver, it passes through a 32dB preamplifier (7) in order to enhance the NMR signal up to a convenient level. In this process the noise is also enhanced because this preamplifier is a broad band amplifier. To maximise the signal-to-noise ratio, the heterodyne spectrometer system employs an intermediate frequency (i.e. ω_i) rf wave. The signal is combined in the mixer (8) with an rf wave generated by the synthesizer (1) at angular frequency $\omega_i + \omega_{ref}$, and the frequency of the NMR signal is transformed from ω_L to $\omega_i + \Omega_L$, where the relative Larmor frequency is,

$$\Omega_L = \omega_{ref} - \omega_L \quad (3.2)$$

Because the relative Larmor frequency Ω_L is about 10kHz–100kHz, much smaller than the intermediate frequency ω_i which is tens of MHz, a narrow band amplifier (9) can be employed to enhance the signal at angular frequency ω_i . The signal is then combined with an rf wave of angular frequency ω_i in the mixer (10), and the NMR signal is transformed into an oscillating electrical current at a lower frequency Ω_L from the higher frequency $\omega_i + \Omega_L$.

In order to distinguish the relative sign of the NMR signal, it is necessary to record the complex FID, i.e. the quadrature receiver records two signals, separated by 90° of phase,

$$\begin{aligned} s_x(t) &= \sin(i\Omega_L t) \exp(-t/T_2) \\ s_y(t) &= \cos(i\Omega_L t) \exp(-t/T_2) \end{aligned} \quad (3.3)$$

where $S_x(t)$ and $S_y(t)$ are the real and imaginary components of the complex FID, respectively.

The NMR signal is an oscillating electrical current. However for the purpose of computer interpretation, it is necessary to convert this analogue signal into digital form. This process is accomplished by specialised electronic circuits called analogue-to-digital converters (ADCs) (12). After being converted into digital form by the ADCs, the NMR signal is transferred to the computer (13) for further interpretation.

3.3 Pulse sequences

3.3.1 Tuning experiments

As discussed in Chapter 2, 90° pulses are very important in NMR experiments, therefore once the sample is loaded it is necessary to find an appropriate 90° pulse by adjusting the width and duration of the rf pulse. This can be achieved by the ‘tuning experiments’. The pulse sequence is illustrated in Fig. 3.8.

A resonant rf pulse with an amplitude A and a duration τ_p is introduced before the induced NMR signal is acquired at the resonant magnetic field B_{nmr} . As discussed in Chapter 2 the effect of an rf pulse is to rotate the longitudinal magnetisation towards the xy -plane with a flip angle that is proportional to the product of the amplitude and duration of the pulse. The NMR signal is proportional to the magnetisation component M_{xy} in the xy -plane, and a 90° pulse corresponds to a pulse that results in the maximum signal. In the tuning experiment, by plotting the signal as a function of the product of the rf pulse amplitude A and duration τ_p , it is possible to find the values of these parameters which give rise to the maximum signal. In our experiments pulse duration was typically $\tau_p = 2\mu\text{s}$.

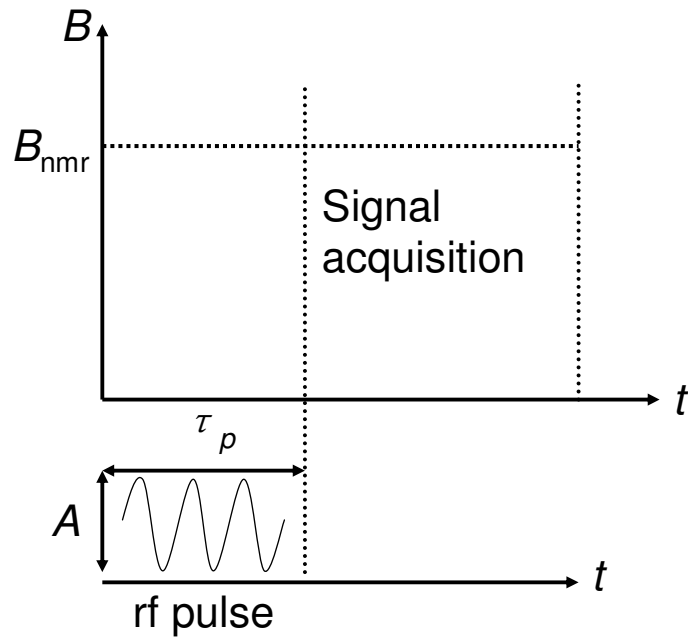


Figure 3.8 Pulse sequence of the tuning experiment without saturation

Apart from the measurement of the NMR signal, a process called saturation also employs 90° pulses. Before the measurement pulse, it employs another resonant rf pulse, and this is used to reduce the longitudinal magnetisation M_z to zero with a saturation of spin-up and spin-down states, therefore this is normally called the saturation pulse. The experimental pulse sequence is illustrated in Fig. 3.9

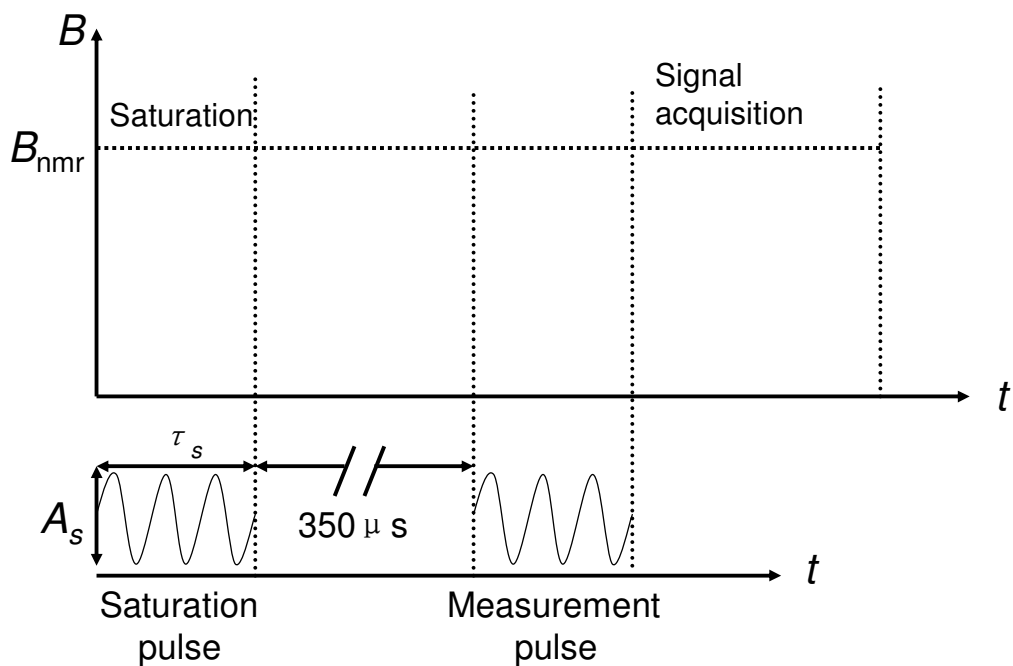


Figure 3.9 Pulse sequence of the tuning experiment with saturation

It is worth noting that it is necessary to set an appropriate time interval τ_{interval} between the two pulses, which allows the transverse magnetisation to decay completely [29], and τ_{interval} must be much shorter than the spin-lattice relaxation time T_1 , but longer than the spin-spin relaxation time T_2 . In our solid-state NMR experiments a value of $\tau_{\text{interval}} = 350\mu\text{s}$ was used. The procedure of finding the appropriate values for amplitude A_s and duration τ_s for the saturation 90° pulse is similar to that of finding the parameters for the measurement 90° pulse. Because the 90° pulse gives rise to a zero value for the longitudinal magnetisation M_z , the signal after measurement should be zero. The amplitude of the saturation pulse is expected to be the same as that of the measurement pulse. However in practise, a slightly smaller amplitude of the saturation pulse gives rise to a better result since the rf pulse generated by the transmitter is not with an ideal waveform.

NMR signals are acquired after the measurement pulse, and this procedure is illustrated in Fig. 3.10. By Fourier transforming the FID, the NMR signal is transformed into the frequency domain, with a random phase. The phase of the signal is then shifted to zero by a phase correction algorithm that is programmed in the NTNMR software. Finally the proton magnetisation is obtained by integrating the real part of the NMR signal within an appropriate, fixed window (dashed lines).

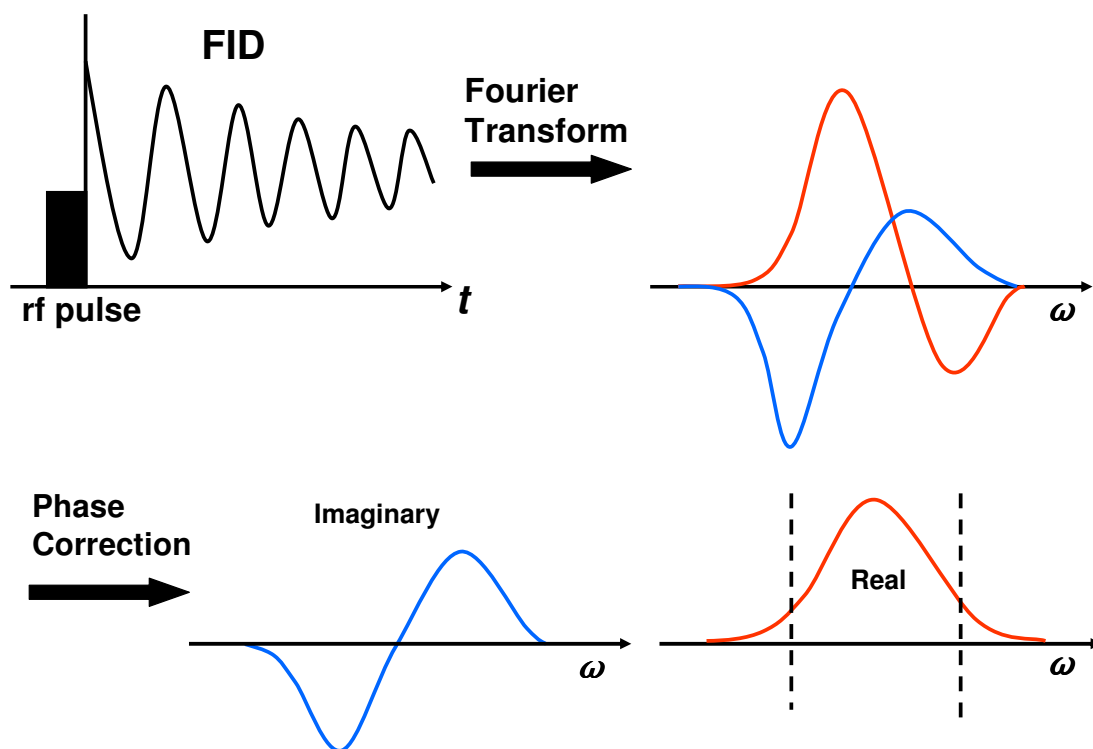


Figure 3.10 Schematic diagram of the NMR signal acquisition

3.3.2 Calibration curve

In field-cycling experiments the rapid field switching between different fields gives rise to a small but distinguishable, systematic field drift. The field drift is predictable as it depends on the initial and final magnetic field, the time spent at the recovery field, and the field switching rate. Generally, the field drift is of the order of 1mT. The effect of the field drift on the NMR signal can be minimised by comparing the signal with a calibration curve, which describes the response of the signal as a function of magnetic field. In NMR, magnetic fields correspond to frequencies, therefore a calibration curve in the frequency domain is obtained using the following pulse sequence (Fig. 3.11).

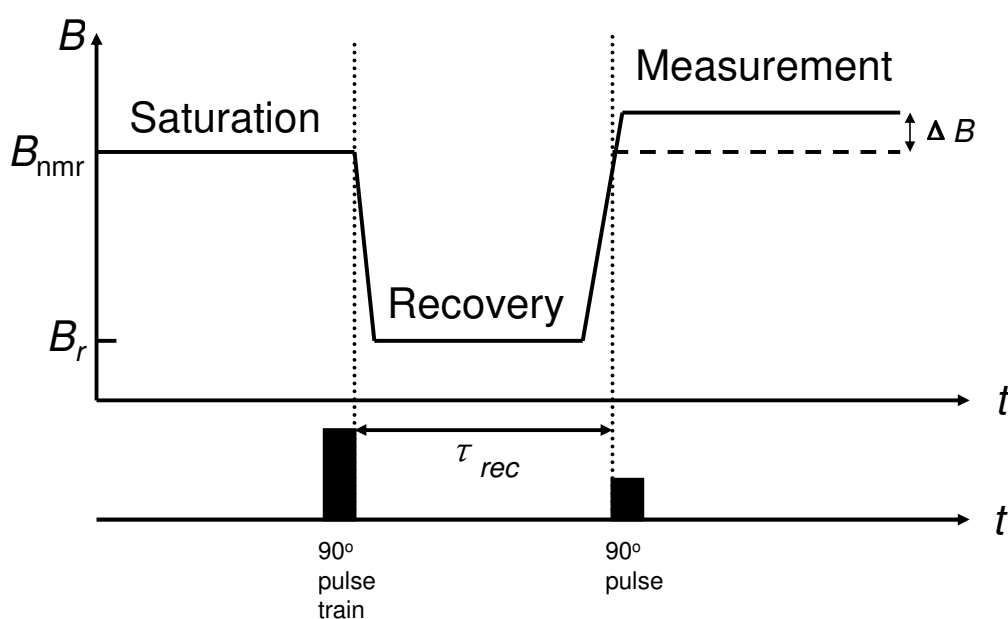


Figure 3.11 Pulse sequence of the probe calibration experiment

Firstly the proton magnetisation is saturated with a train of 90° rf pulses. Theoretically a single 90° pulse can rotate the longitudinal magnetisation M_z completely into the xy -plane. However in practise, the rf field is not perfectly homogenous. Therefore a train of 90° pulses is employed to reinforce the saturation of the longitudinal magnetisation M_z . A train of 12 pulses was found to be sufficient for saturating the magnetisation in our experiments. The magnetisation then relaxes at a recovery field B_r , and some longitudinal magnetisation builds up during a fixed time interval τ_{rec} . Finally the NMR signal is acquired at a slightly off-resonant field $B_{nmr} + \Delta B$. The corresponding signal is expected to be smaller than that measured at the resonant field B_{nmr} . By incrementing the magnetic field offset ΔB from a negative value to a positive value, a plot of the NMR signal as a function of ΔB is achieved,

and it effectively describes the profile of the signal response to the field drift. A typical normalised calibration curve in the magnetic field domain is illustrated in Fig. 3.12.

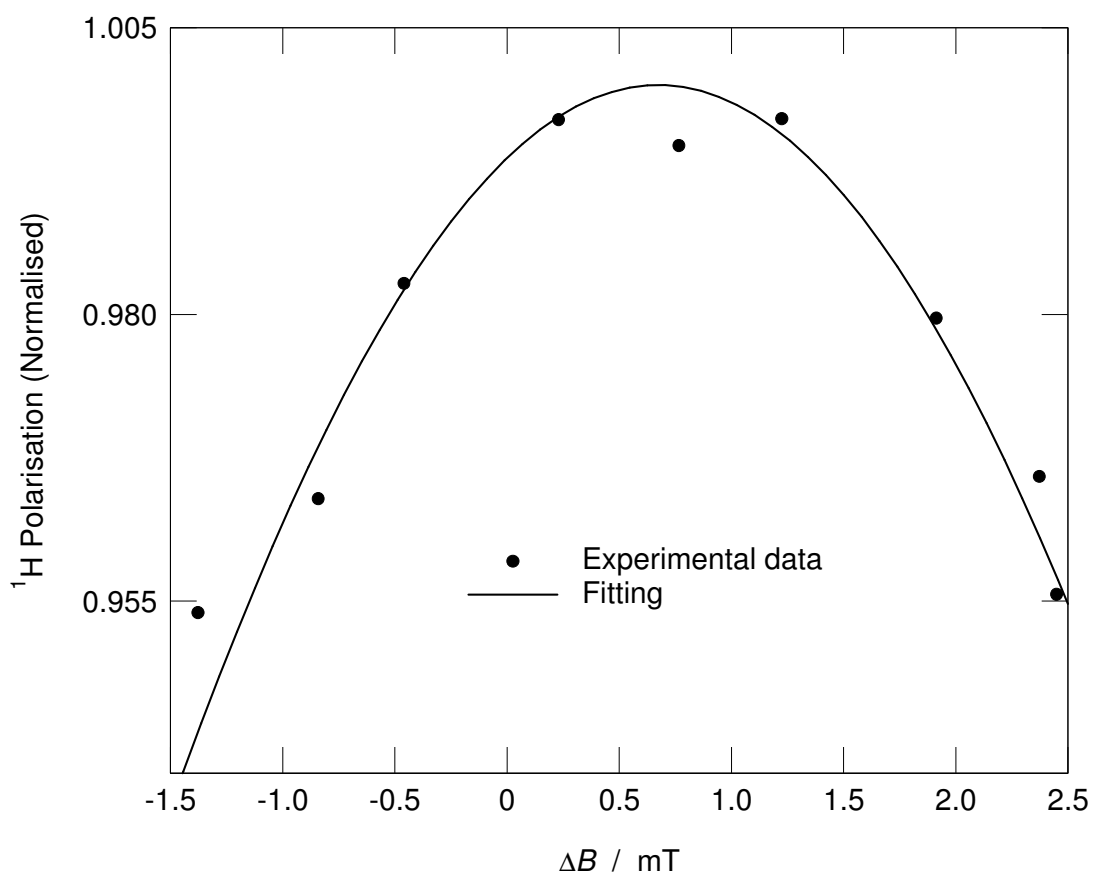


Figure 3.12 Normalised calibration curve; the data were recorded at the off-resonant field $B_{\text{nmr}} + \Delta B$

With the calibration curve, the experimental data are calibrated to the resonant field to minimise the effect of field drift.

Furthermore, because the field drift is a systematic function of the fields and times that define the response, the field and time-dependence of field offsets have been determined, and programmed into the Visual Basic programme to minimise these effects [41, 42].

3.3.3 Field-cycling T_1 experiments

The accurate measurement of spin-lattice relaxation time T_1 is crucial to the study of molecular dynamics via NMR. Two methods for doing so are described here. Normally the standard ‘saturation-recovery’ pulse sequence (Fig 3.13) is employed, whereas at low

magnetic fields, an alternative ‘polarisation-recovery’ pulse sequence (Fig. 3.15) is used when the signal is relatively small.

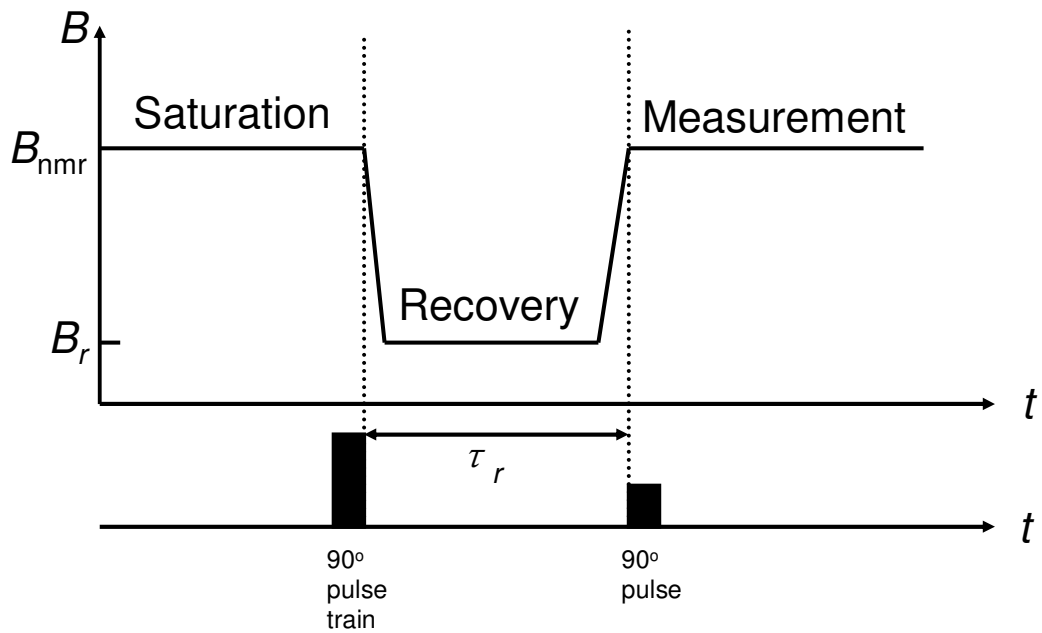


Figure 3.13 Pulse sequence of the saturation-recovery experiment

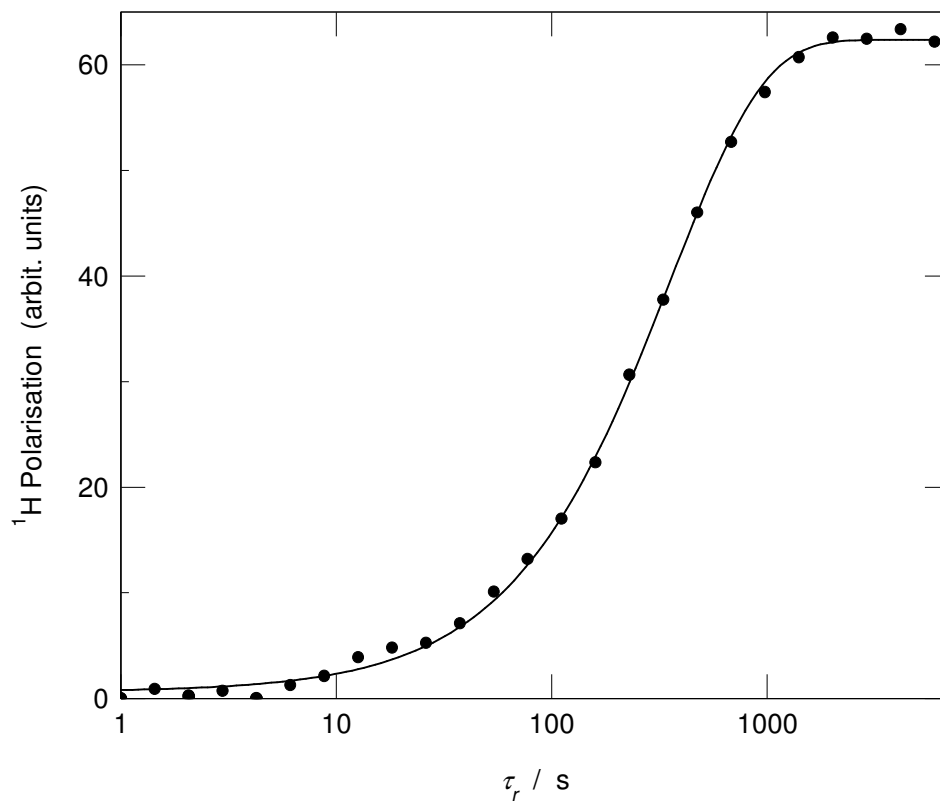


Figure 3.14 Saturation-recovery experimental data of the spin-lattice relaxation time T_1 for ^1H in sodium acetate trihydrate recorded at $T = 7.45\text{K}$ and $B_r = 0.0375\text{T}$; the solid line was obtained from the curve fitting; $T_1 = 357 \pm 7$ s

As shown in Fig. 3.13, the magnetisation is saturated with a train of resonant 90° rf pulses at the resonant field B_{nmr} . This is followed by a rapid switch of the magnetic field to the recovery field B_r , at which the magnetisation is allowed to recover towards thermal equilibrium for a given period of time τ_r . Finally after a rapid switch back to the resonant field B_{nmr} , the magnitude of the recovered magnetisation is measured with a 90° pulse. With logarithmic increments of the recovery time τ_r up to a value $\tau_r > 5T_1$, measurements of the longitudinal magnetisation as a function of the recovery time τ_r reveals the relaxation curve.

A typical saturation-recovery T_1 curve is plotted on a semi-logarithmic graph in Fig. 3.14. The calibrated experimental data (filled circles) are fitted well to the third equation of Eqn. (2.18), which describes the recovery of magnetisation from zero magnetisation. From the best fit parameter the experimental value of spin-lattice relaxation time $T_1 = 357 \pm 7$ s is obtained.

The saturation-recovery experiment is very common, and can be used when B_0 is large. However at low magnetic field when the magnetisation at thermal equilibrium is very small, it can be difficult to accurately measure T_1 by fitting the saturation-recovery T_1 curve. In this case the polarisation-recovery pulse sequence (Fig. 3.15) may be employed.

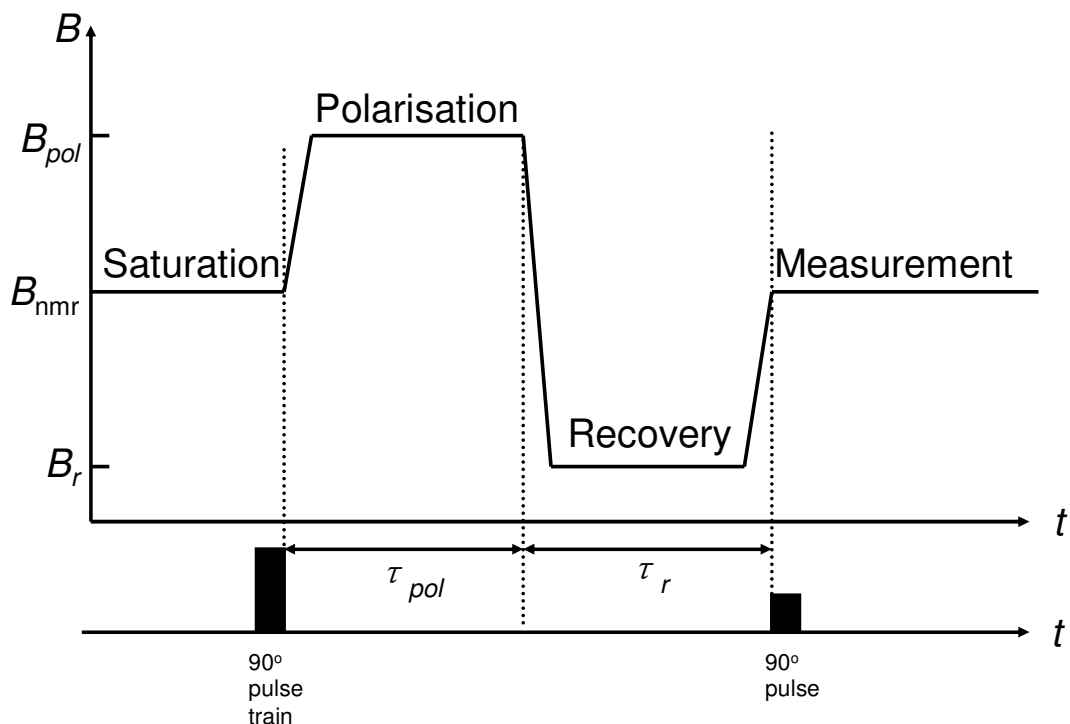


Figure 3.15 Pulse sequence of the polarisation-recovery experiment

In Fig. 3.15, the difference from the saturation-recovery pulse sequence is the high field polarisation step before the recovery period. The magnetisation is initially saturated with a

train of resonant 90° rf pulses at the resonant field B_{nmr} . The magnetic field is then switched rapidly to a high polarisation field B_{pol} , where a large non-equilibrium magnetisation is built up for a fixed period of time τ_{pol} . After a rapid switch to the recovery field B_r , the magnetisation recovers towards thermal equilibrium for a given period of time τ_r . Finally after a rapid switch back to B_{nmr} , the recovered magnetisation is measured with a 90° pulse. As with the saturation-recovery experiment, the recovery time τ_r is incremented logarithmically, and a typical polarisation-recovery T_1 curve is presented in Fig. 3.16.

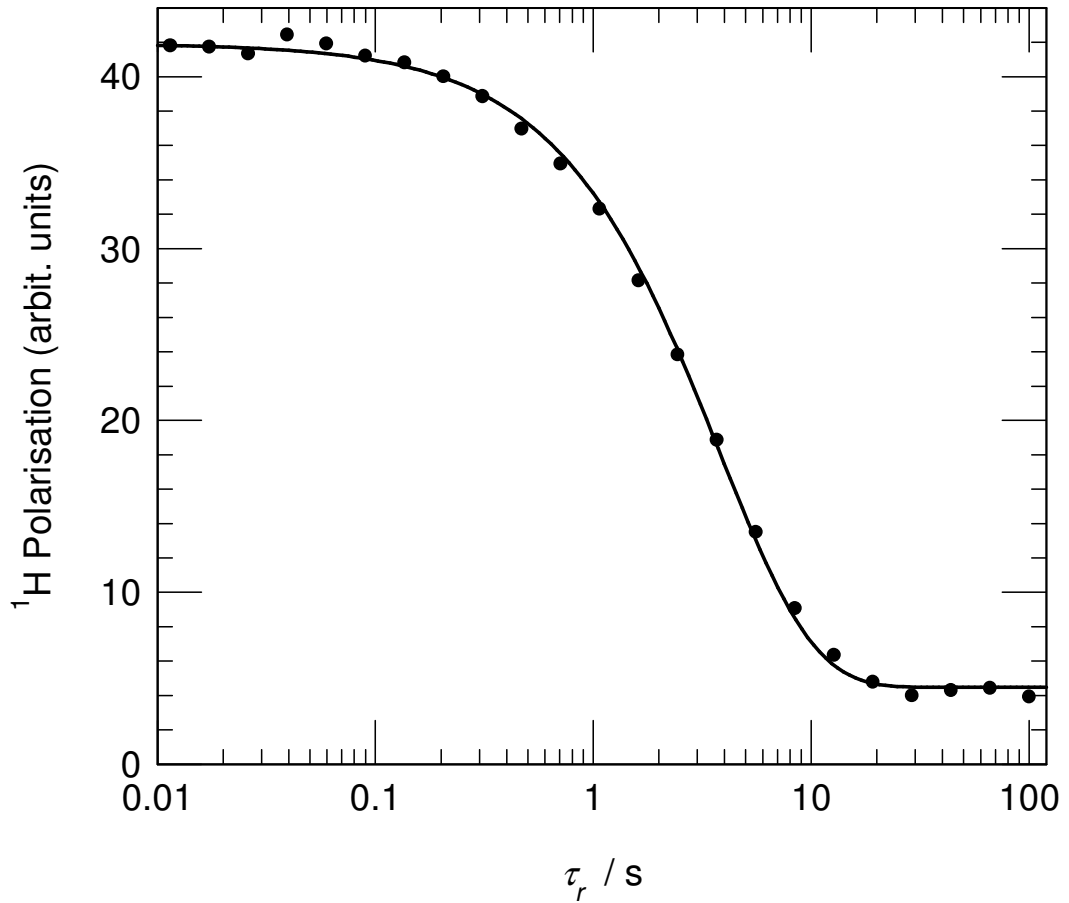


Figure 3.16 Polarisation-recovery experimental data of the spin-lattice relaxation time T_1 for ^1H in sodium acetate trihydrate recorded at $T = 57\text{K}$ and $B_r = 0.0375\text{T}$; the ^1H spin was polarised at $B_{\text{pol}} = 0.863\text{T}$ for $\tau_{\text{pol}} = 10\text{s}$; the solid line was obtained from the curve fitting; $T_1 = 3.77 \pm 0.08 \text{ s}$

The spin-lattice relaxation time $T_1 = 3.77 \pm 0.08 \text{ s}$ is obtained, by fitting the experimental data (filled circles) to Eqn. (3.4),

$$M_z = M_0 + (M_{\text{pol}} - M_0) \exp\left(\frac{-t}{T_1}\right) \quad (3.4)$$

which is simply the solution to the Bloch equations with an initial magnetisation of $M_{\text{pol}} > M_0$.

3.3.4 Tunnel resonance level-crossing experiment

The study of methyl group dynamics and its associated tunnelling reservoir is aided significantly by the manipulation of the tunnelling reservoir via NMR. This is a central topic of this thesis. In the presence of a static magnetic field, a Zeeman reservoir associated with the Larmor frequency is established. Under some appropriate circumstances the tunnelling reservoir can be coupled with the Zeeman reservoir. Consequently some unique phenomena associated with the tunnelling reservoir are exhibited, from which information of the methyl molecular dynamics may be determined.

In 1958 the tunnel resonance phenomenon was first anticipated by Stejskal and Gutowsky [6]. The first actual tunnel resonance experiment was conducted by Van Hecke and Janssens [21]. For methyl groups when the Larmor frequency matches the tunnelling frequency, a strong, anomalous change in the nuclear spin-lattice relaxation rate T_1^{-1} can occur. This phenomenon is called tunnel resonance.

In order to study tunnel resonance, several kinds of level-crossing experiments have been developed. The typical level-crossing pulse sequence used in this work is illustrated in Fig.3.17.

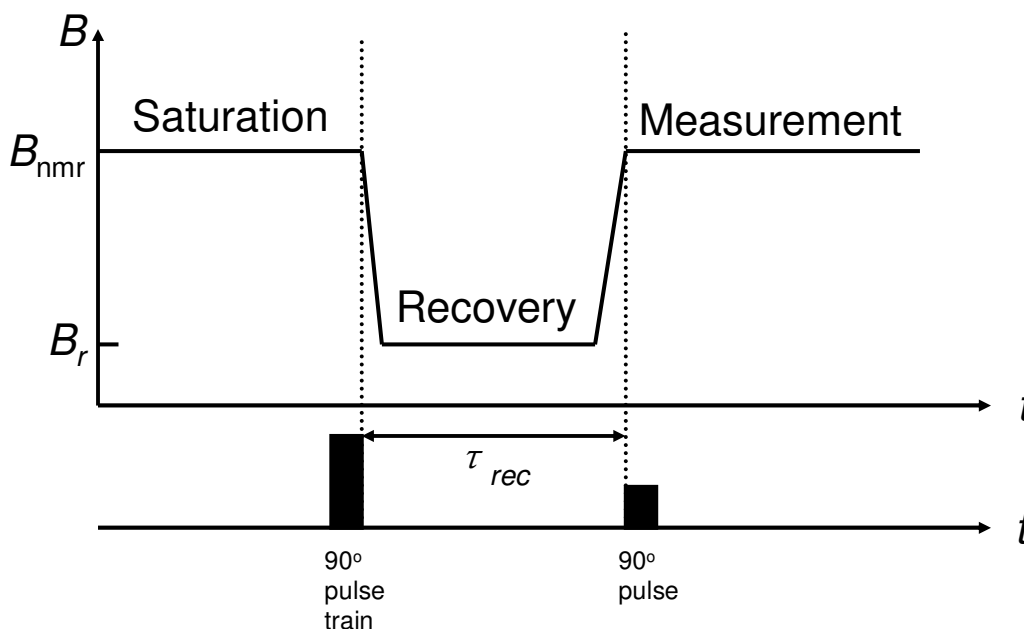


Figure 3.17 Level-crossing pulse sequence of the tunnel resonance experiment

The pulse sequence is similar to that of saturation-recovery experiments. However in the level-crossing experiments, the recovery field B_r is incremented rather than the recovery time τ_{rec} . Because the tunnel resonance effect can only occur when the Larmor frequency is close to the tunnelling frequency, it is necessary that the increment of B_r passes through the resonant field associated with the tunnelling frequency. One example of a tunnel resonance spectrum conducted using the level-crossing pulse sequence is presented in Fig. 3.18.

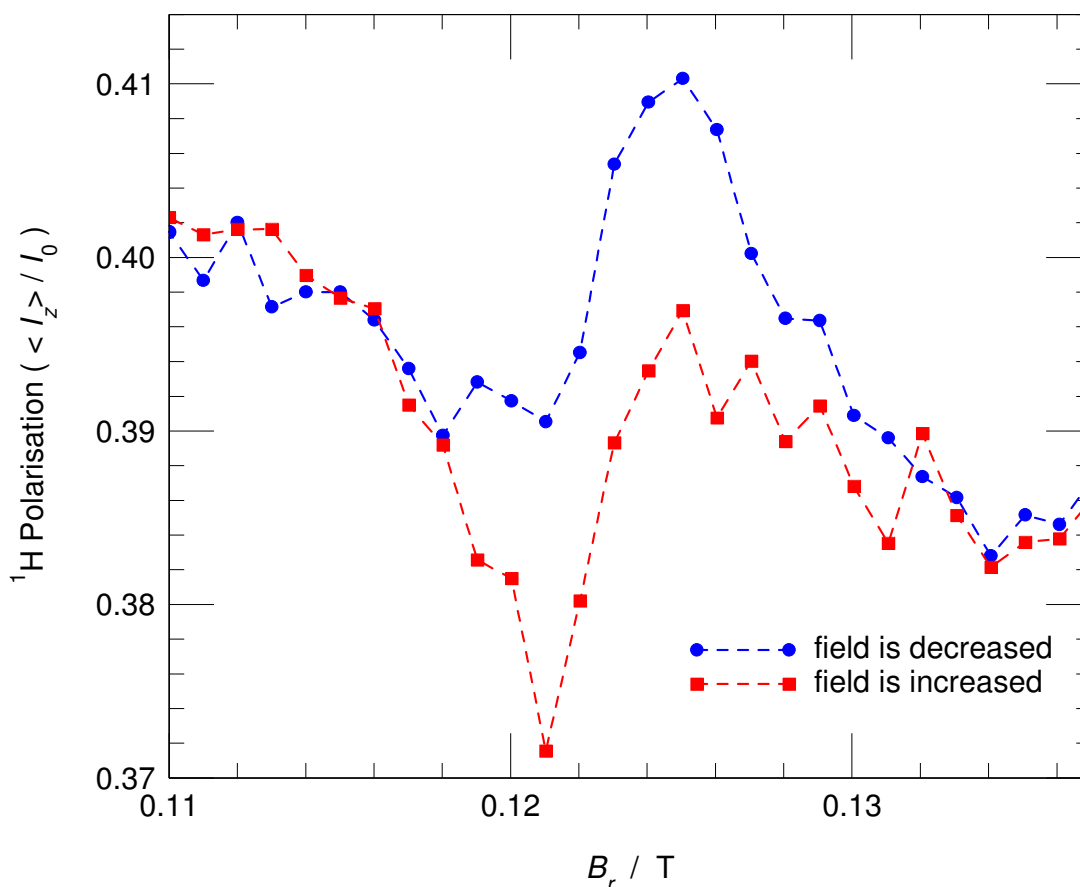


Figure 3.18 Tunnel resonance spectra of m-xylene doped with DPPH radicals recorded at $T = 4.2\text{K}$; both field scan directions have been conducted

3.3.5 Low-field dipole-dipole driven experiment

Field-cycling NMR allows direct measurements of the tunnelling frequency in the range from few kHz to several MHz [43–46]. Measurements are undertaken at low field in the presence of rf irradiation.

According to the Selection Rules, particular transitions are symmetry forbidden at high magnetic fields, in particular there are no $\Delta m = 0$ transitions (e.g. in Fig. 2.7 there are no transitions between states $|+1/2, A\rangle$ and $|+1/2, E\rangle$ or between $|-1/2, A\rangle$ and $|-1/2, E\rangle$).

However at low magnetic field, the conditions are changed and the Selection Rules are dramatically modified since the wave functions become mixtures of the A and E species. As a result the $\Delta m = 0$ transitions, which are symmetry forbidden at high magnetic field, become allowed. Consequently at low field, and in the presence of rf irradiation the nuclear magnetisation change associated with $\Delta m = 0$ transitions can occur. Additionally, the methyl tunnelling sidebands (solid arrows in Fig. 2.7) are strongly enhanced since the tunnelling reservoir is effectively coupled with the Zeeman reservoir mediated by the rf irradiation.

Experiments that reveal this low-field NMR phenomenon are called the low-field dipole-dipole driven experiments, or simply the low-field NMR experiments. In order to reveal the change in the nuclear magnetisation, it is necessary to polarise the sample at a high field before allowing it to evolve at low field. Fig. 3.19 shows the pulse sequence of such a low-field dipole-dipole driven experiment.

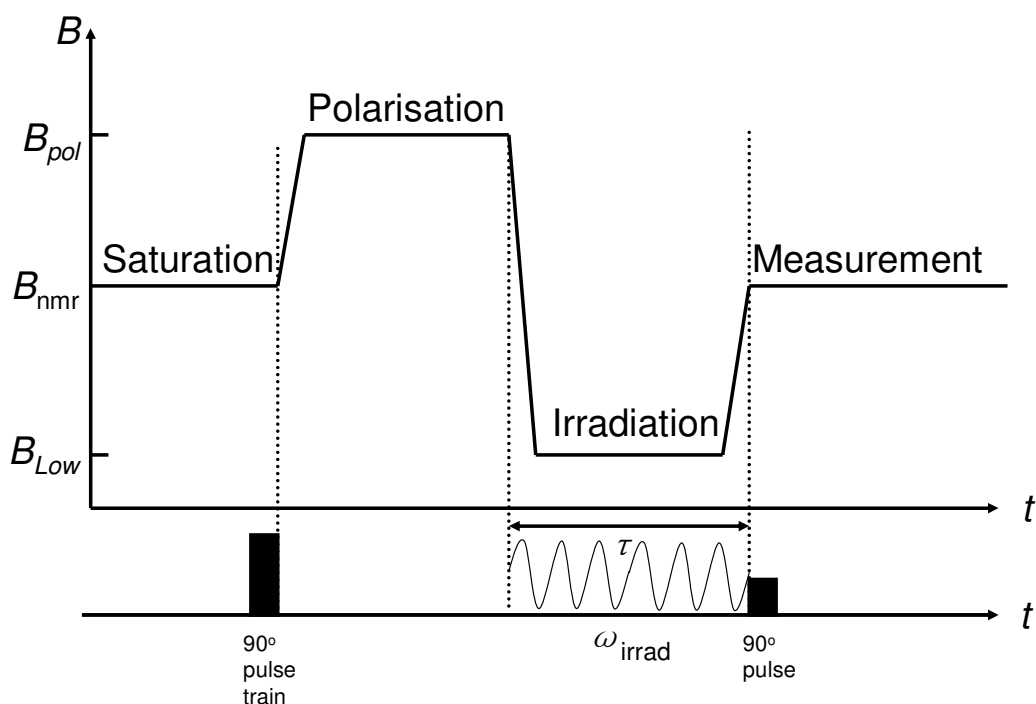


Figure 3.19 Pulse sequence of the low-field dipole-dipole driven experiment

The magnetisation is saturated with a train of 90° pulses, and the sample is polarised at B_{pol} , for a fixed period of time. After a large ^1H polarisation builds up, a rapid field switch brings the sample to the low magnetic field B_{low} . In the presence of the secondary rf irradiation at angular frequency ω_{irrad} , the magnetisation evolves at B_{low} for a period of time τ . Finally the magnetisation is measured with a 90° pulse after a rapid field switch back to the resonant field B_{nmr} . By incrementing the frequency ω_{irrad} of rf irradiation, the low-field NMR spectrum is

obtained. It is important that ω_{irrad} is passed through the tunnelling frequency so that the $\Delta m = 0$ transitions can be revealed. An example of the spectrum measured by the low-field NMR pulse sequence is given in Fig. 3.20.

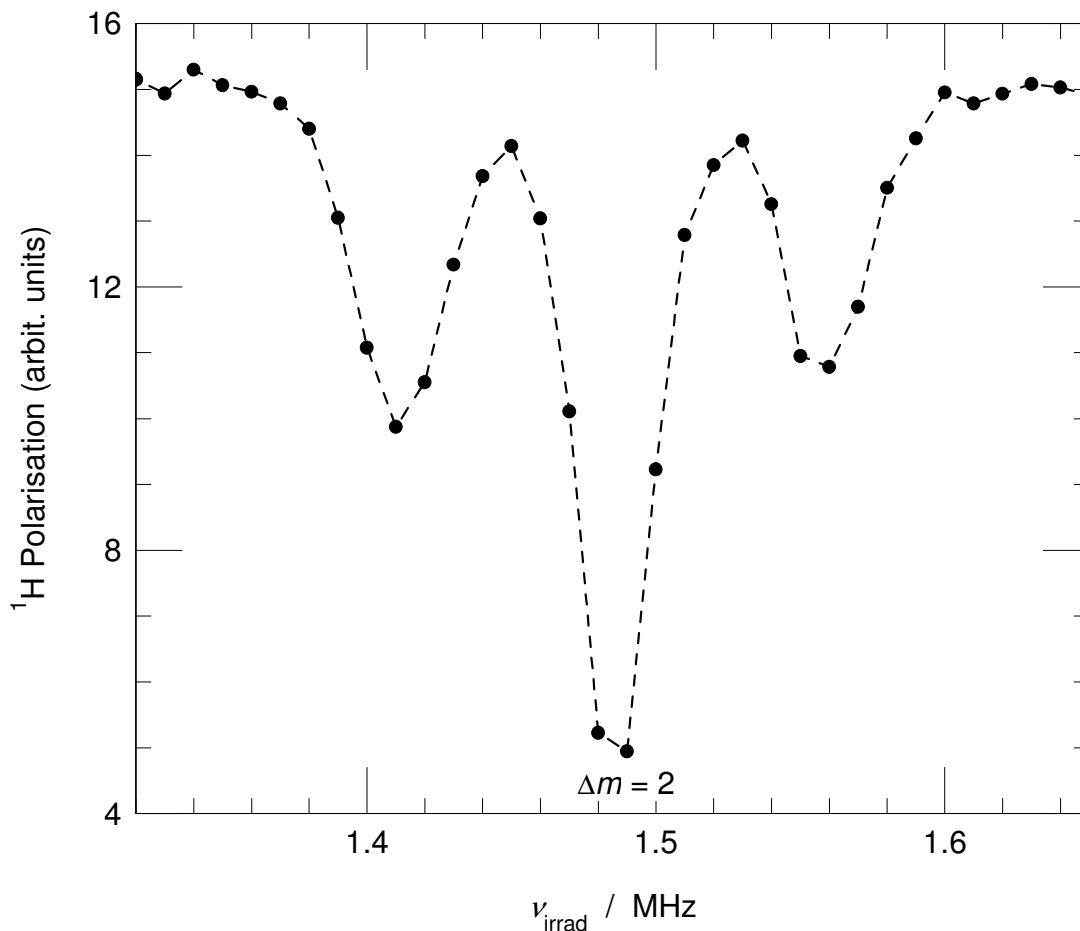


Figure 3.20 Low-field NMR spectrum of methylmalonic acid recorded at $T = 4.2\text{K}$ and $B_{\text{low}} = 0.175\text{T}$

As illustrated, when the frequencies of the rf irradiation matches those associated with the transitions that involve a change in nuclear magnetisation, the prepared magnetisation is reduced, hence such a negative-peak spectrum is obtained.

3.4 Software

In order to improve the automation of the NMR spectrometer system, to increase the efficiency and accuracy of the analysis of the experimental data, and to achieve the theoretical modelling computation, a variety of software has been employed in this work. The ‘NTNMR’ software was used to control the NMR spectrometer system and to design different pulse sequences [41, 47]. The ‘Visual Basic’ software was utilised to automate the control of the

NTNMR software. In order to build the theoretical model, the computational software 'Matlab' was used for the numerical simulation and theoretical analysis.

Generally speaking, the NTNMR software is the NMR spectrometer controlling software based on the Windows NT system. It is mainly responsible for the communication between the computer and the NMR spectrometer. Through two PCI cards it allows the computer to exchange data with the NMR spectrometer as well as to control the NMR spectrometer. For instance, during saturation process it allows parameters for an rf pulse (e.g. angular frequency ω and irradiation time τ) to upload to the spectrometer, and it then controls the spectrometer to generate this rf pulse.

Within the NTNMR software, a variety of pulse sequences that operate different experiments has been designed [41, 42]. It also allows a further automation of the system by combining with the computer language Visual Basic. Additionally, some data analysis can be achieved by using the NTNMR software, such as the Fourier transform of the FID signal.

The numerical computational software Matlab has been utilised extensively in this work. It was used for modelling experimental data, and for numerical calculations. For instance, it was used to simulate the ^1H magnetisation relaxation due to methyl molecular dynamics, and to study the tunnelling properties of the methyl group.

Chapter 4 Low-field dipole-dipole driven experiments on methylmalonic acid and methyl ethyl ketone

4.1 Introduction

As discussed in Chapter 2, according to the Selection Rules, some tunnelling transitions from rotational states A to E are symmetry forbidden at high magnetic field. For example, transitions from state $(A, 1/2)$ to $(E, 1/2)$ or from $(A, -1/2)$ to $(E, -1/2)$ are not allowed since the $\Delta m = 0$ transitions are forbidden. However at low magnetic field, the Selection Rules are dramatically modified since the states are not pure A or E states, therefore transitions that are symmetry forbidden at high field may become allowed. Moreover the methyl tunnelling sideband transitions, which are the tunnelling transitions with angular frequencies of $\omega_t + \omega_L$, $\omega_t - \omega_L$, $\omega_t + 2\omega_L$ and $\omega_t - 2\omega_L$ (solid arrows in Fig. 2.7), are strongly enhanced since the transition probabilities are increased when the tunnelling reservoir is coupled with the Zeeman reservoir in the presence of the appropriate rf irradiation.

Since the first measurements of the tunnelling frequency of the methyl group at low magnetic field using field-cycling NMR, a variety of low-field dipole-dipole driven experiments have been developed to study methyl tunnelling [43–46, 48–51]. However, one disadvantage of traditional low-field NMR experiments is that tunnelling sidebands are very weak since transitions may be constrained because of saturation of the rotational states [52]. In order to avoid this saturation problem, a technical method known as the double sideband irradiation was developed by McDonald [53].

In this thesis, some modifications of the double sideband irradiation method have been made, and the technique has been adapted to the Nottingham field-cycling NMR spectrometer. In this chapter pulse sequences of the stirring low-field NMR experiments will be discussed. The low-field NMR experiments conducted on methylmalonic acid and methyl ethyl ketone will be introduced. Finally the experimental results will be presented and discussed.

4.2 Theoretical

In low-field dipole-dipole driven NMR spectra, there are several sideband peaks that correspond to the tunnelling transitions $h(\omega_t + \omega_L)$, $h(\omega_t - \omega_L)$, $h(\omega_t + 2\omega_L)$ and $h(\omega_t - 2\omega_L)$ (Fig. 2.7). These sidebands are labelled a+, a-, b+ and b-, respectively. Sometimes the intensity of the sideband is very small because the populations of the states associated with

the transitions can be easily saturated. As a result the transitions can be constrained, thereby preventing further changes in ^1H polarisation.

The thermodynamic model of the methyl rotor discussed in Chapter 2 is recalled here. In the tunnelling reservoir, populations of the A state and E states are characterised by the tunnelling temperature θ_t , and the population of the rotational states is governed by,

$$\frac{P(E)}{P(A)} = \exp(-\beta_t \omega_t) \approx 1 - \beta_t \omega_t \quad (4.1)$$

with $\beta_t = h/(k_B \theta_t)$. $P(E)$ and $P(A)$ are the populations of the A and E states, respectively. ω_t is the tunnelling frequency that is determined by the ground state tunnelling splitting.

For simplicity, a quantum number for tunnelling states may be defined as follows, $n = 1/2$ for the E states while $n = -1/2$ for the A state. Thus with constants being discarded in Eqn. (4.1) it may be rewritten as [52],

$$P_n = -n\beta_t \omega_t. \quad (4.2)$$

A similar treatment applies to the Zeeman reservoir, where the population for each Zeeman state is given by,

$$P_m = -m_l \beta_z \omega_z. \quad (4.3)$$

Here m_l denotes the nuclear spin magnetic quantum number. $\beta_z = h/(k_B \theta_z)$ with θ_z is the Zeeman temperature. ω_z is the Larmor frequency. Considering the quantum number $m_l = \pm 1/2$ for the E species while $m_l = \pm 1/2$ and $\pm 3/2$ for the A species, the populations of the system are,

$$P_{nm} = -n\beta_t \omega_t - m_l \beta_z \omega_z \quad (4.4)$$

where P_{nm} represents the population of the state with tunnelling species n and Zeeman state m_l . For example, $P_{+1/2+1/2}$ is the population of the E species with a Zeeman state $+1/2$.

β_z and β_t may be written as,

$$\beta_z = -\frac{\sum_{n,m_l} m_l P_{nm}}{\omega_z \sum_m m_l^2}$$

$$\beta_t = -\frac{\sum_{n,m_l} n P_{nm}}{\omega_t \sum_n n^2}. \quad (4.5)$$

If a particular transition from the state (n, m_l) to (n', m_l') is driven, the populations of these two states will change until they are equal to each other, thus causing the change in ^1H

polarisation to be zero, and this is called the transition saturation. Therefore the saturation condition is given by,

$$P_{nm} = P_{n'm'}. \quad (4.6)$$

Substituting Eqn. (4.4) in Eqn. (4.6), we obtain,

$$\frac{\beta_z}{\beta_t} = -\frac{\omega_t \Delta n}{\omega_{zt} \Delta m} \quad (4.7)$$

where $\Delta n = n - n'$ and $\Delta m = m_t - m_t'$ that depend on the transitions.

It is very convenient to imagine the evolution of the system in the $\beta_t - \beta_z$ space. The $\beta_t - \beta_z$ space and the saturation conditions are illustrated in Fig. 4.1. Four solid lines are the saturation conditions for the four sideband transitions at angular frequencies $\omega_t + \omega_L$, $\omega_t - \omega_L$, $\omega_t + 2\omega_L$ and $\omega_t - 2\omega_L$. Additionally, the dashed line coincident with the y-axis is the saturation condition for the A-E conversions with $\Delta n = 1$ and $\Delta m = 0$, which are forbidden at high field but can be allowed at low field.

The initial state of the system can be interpreted as a point (β_t, β_z) in the $\beta_t - \beta_z$ space. The evolution of the system can be described by the movement of the point (β_t, β_z) in the $\beta_t - \beta_z$ plane. The direction of the movement is determined by $d\beta_z/d\beta_t$.

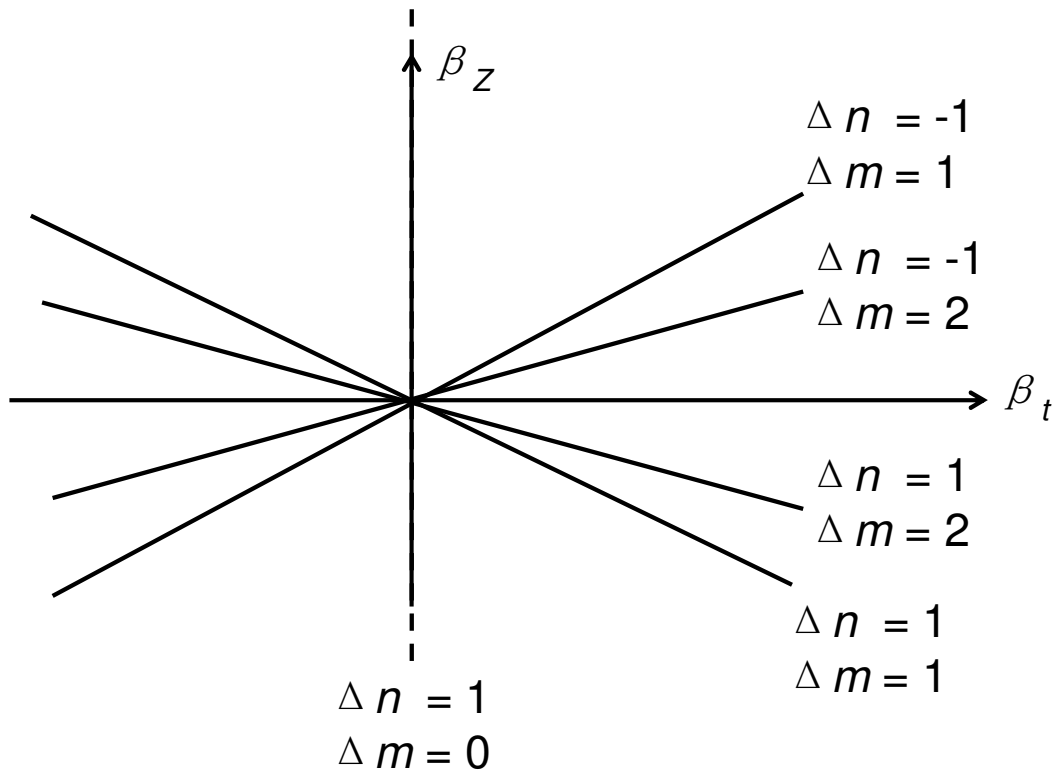


Figure 4.1 Saturation conditions of the tunnelling transitions in the $\beta_t - \beta_z$ space

For each transition the net change in populations of the two states must be zero. Therefore, for the transition from the state (n, m_l) to (n', m_l') , the population change is,

$$\Delta P_{nm} = -\Delta P_{n'm'} \quad (4.8)$$

Substituting Eqn. (4.8) in Eqn. (4.5), we obtain,

$$\begin{aligned} \Delta\beta_z &= -\frac{\Delta m \Delta P_{nm}}{\omega_z \sum_{m_l} m_l^2} \\ \Delta\beta_t &= -\frac{\Delta n \Delta P_{nm}}{\omega_t \sum_n n^2}. \end{aligned} \quad (4.9)$$

Therefore the direction the system evolves in the $\beta_t - \beta_z$ space is obtained,

$$\frac{d\beta_z}{d\beta_t} = \frac{\Delta m}{\Delta n} \frac{\omega_t \sum_n n^2}{\omega_z \sum_{m_l} m_l^2}. \quad (4.10)$$

By integrating Eqn. (4.10) the trajectory in the $\beta_t - \beta_z$ space is obtained from,

$$\frac{\beta_z}{\beta_t} = \frac{\Delta m}{\Delta n} \frac{\omega_t \sum_n n^2}{\omega_z \sum_{m_l} m_l^2} + Const. \quad (4.11)$$

The coordinates β_t and β_z are the powers in the exponential function for the Boltzmann distribution, therefore the evolution of the real system decays exponentially as the point (β_t, β_z) approaches the saturation conditions.

According to Eqn. (4.11), the trajectory defining the evolution of the system depends on the transition with particular Δn and Δm , which is generated by the frequency of the secondary rf irradiation at low field. Thus the trajectory of the population evolution can be controlled by applying rf irradiation with different frequencies, and the saturation conditions can be avoided by applying rf irradiation at two alternating frequencies. Therefore, enhanced sideband peaks can be obtained in the low-field dipole-dipole driven experiments. Taking the transition $\Delta n = -1$ and $\Delta m = 1$ for example, the angular frequency associated with this transition is $\omega_t - \omega_L$. The trajectories of evolutions for both cases of single and double rf irradiation are illustrated in Fig. 4.2. In the case of single rf irradiation, with the angular frequency of $\omega_t - \omega_L$, indicated by the dotted arrow in Fig. 4.2, the transition approaches rather rapidly towards its saturation condition. As a result the corresponding sideband peak observed in the experimental spectrum can be rather small.

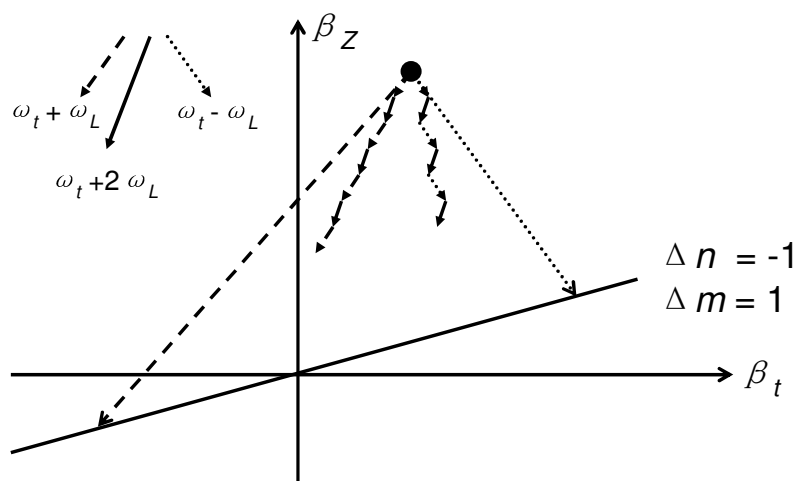


Figure 4.2 Schematic illustration of the population evolution of the Zeeman and tunnelling reservoirs in the low-field NMR experiment

However if the sample is irradiated at two frequencies (i.e. $\omega_t - \omega_L$, the frequency of the tunnelling sideband a- transition, and $\omega_t + \omega_L$, the frequency of the b- transition), the alternating change in the direction of the trajectory controlled by double rf irradiation enables the transition to evolve without meeting its saturation condition. Therefore, a much stronger sideband peak can be observed in the spectrum.

4.3 Experimental

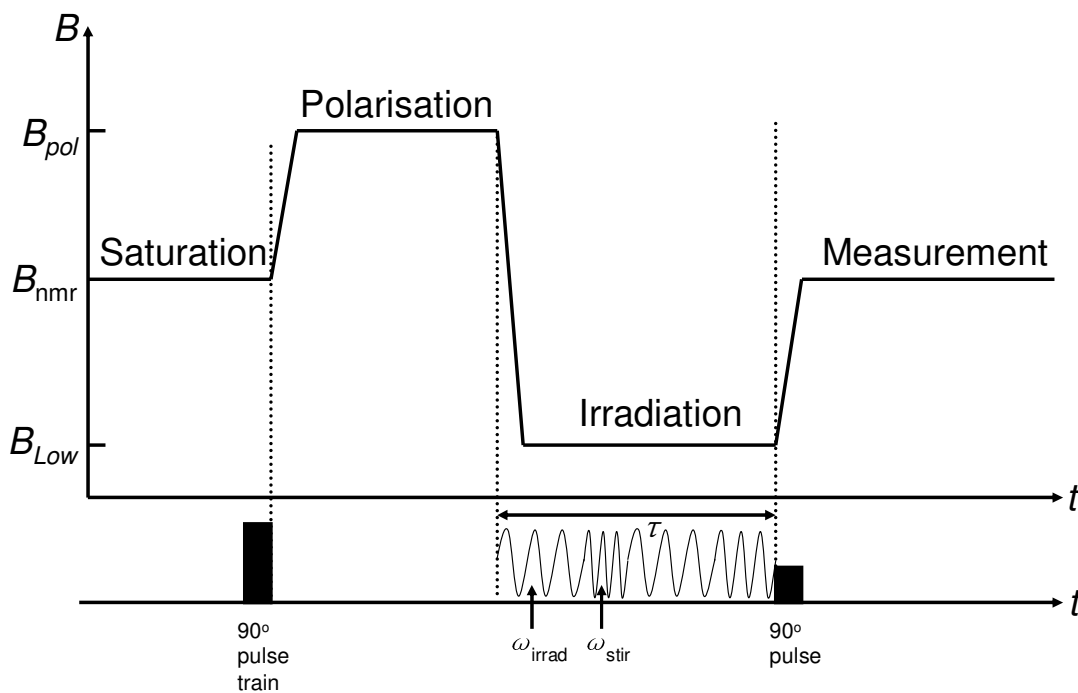


Figure 4.3 Pulse sequence of the stirring low-field NMR experiment; a loop of two-frequency rf irradiation was utilised

In this work a variety of low-field dipole-dipole driven experiments with double rf irradiation have been conducted. The pulse sequence of the sideband stirring low-field NMR experiment (Fig 4.3) was similar to that of the conventional low-field NMR experiment. The sample was irradiated at two frequencies that alternate. One was the scanning frequency, labelled ω_{irrad} or ω_{rf} , which was incremented during the experiment. The other was called the stirring frequency, labelled ω_{stir} , which was normally set to be the same as one of the tunnelling sideband frequencies.

In this chapter, numerical simulations of low-field NMR were made. Given the tunnelling frequency and the initial tunnelling temperature, the nuclear polarisation in low-field NMR was calculated by using Eqn. (4.2)–(4.11).

4.4 Results and discussion

4.4.1 Methylmalonic acid

Firstly a conventional low-field dipole-dipole driven experiment was conducted on methylmalonic acid, by using the pulse sequence of the low-field NMR experiment (Fig. 3.19), and the corresponding low-field NMR spectrum is presented in Fig. 4.4. The ^1H spins were polarised at $B_{\text{pol}} = 1\text{T}$ for 120s before the sample was irradiated at ν_{rf} for 1s. On the right-hand side of the spectrum, three discrete peaks are observed. The middle peak, labelled B, is measured at the frequency of $\nu_{\text{rf}}^{(\text{B})} = 1.563 \pm 0.001 \text{ MHz}$. This is consistent with the characteristic frequency of the $\Delta m = 2$ transition at the field $B_{\text{low}} = 0.0183\text{T}$. Therefore, it is evident that this peak arises from the decrease of the ^1H polarization during the transition between the Zeeman levels with a splitting of $2h\nu_L$ (dashed arrows in Fig. 2.7), mediated by the dipole-dipole interaction. On the left-hand side a rather large negative peak, labelled A, is observed at the frequency $\nu_{\text{rf}}^{(\text{A})} = 0.7815 \pm 0.001 \text{ MHz}$, and this is consistent with the transition between the Zeeman levels with a splitting of $h\nu_L$ ($\Delta m = 1$).

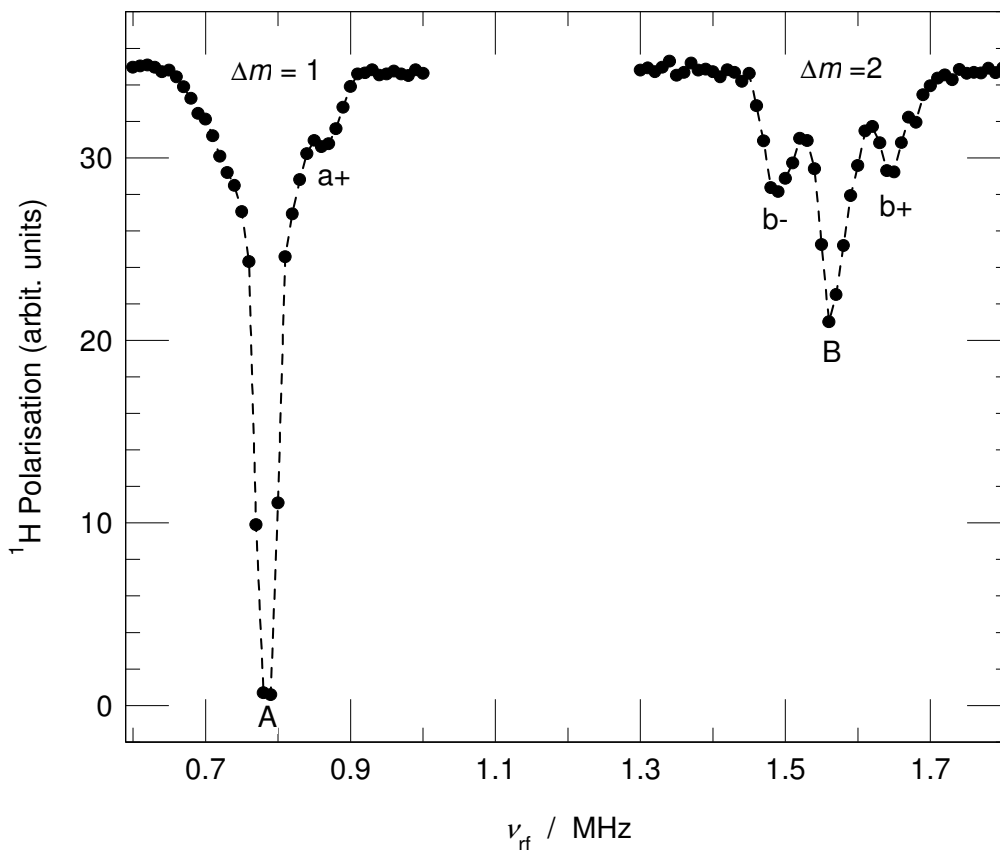


Figure 4.4 Low-field NMR spectrum of methylmalonic acid recorded at $T = 4.2\text{K}$ and $B_{\text{low}} = 0.0183\text{T}$

Surrounding peak B, two smaller sideband peaks, labelled b- and b+, are observed. The frequencies are directly measured to be $\nu_{\text{rf}}^{(\text{b-})} = 1.486 \pm 0.001$ MHz and $\nu_{\text{rf}}^{(\text{b+})} = 1.640 \pm 0.001$ MHz. The difference in frequency between peaks B and b-, $\Delta\nu = \nu_{\text{rf}}^{(\text{B})} - \nu_{\text{rf}}^{(\text{b-})} = 77 \pm 1$ kHz, is the same as that between peaks b+ and B, $\Delta\nu = \nu_{\text{rf}}^{(\text{b+})} - \nu_{\text{rf}}^{(\text{B})} = 77 \pm 1$ kHz. This difference in frequency has been determined to be field independent by experiments conducted at different fields. This shows that the difference in frequency, $\Delta\nu = 77 \pm 1$ kHz, is the characteristic tunnelling frequency of the methyl group, i.e. $\nu_t = 77 \pm 1$ kHz, and this is consistent with the value in the literatures [50, 52, 54]. Therefore, it is clear that $\nu_{\text{rf}}^{(\text{b-})} = \nu_{\text{rf}}^{(\text{B})} - \Delta\nu = 2\nu_L - \nu_t$ and $\nu_{\text{rf}}^{(\text{b+})} = \nu_{\text{rf}}^{(\text{B})} + \Delta\nu = 2\nu_L + \nu_t$. This reveals that the sideband b- and b+ peaks arise from the change in ^1H polarisation during the tunnelling transitions of $h(2\nu_L - \nu_t)$ and $h(2\nu_L + \nu_t)$.

Similar to the $\Delta m = 2$ sideband b- and b+ peaks, two sideband peaks associated with the tunnelling transitions $h(\nu_L - \nu_t)$ and $h(\nu_L + \nu_t)$ are expected in the $\Delta m = 1$ region. However, only weak sideband peaks are observed in the $\Delta m = 1$ region. The observed weak peak, labelled a+ shows that the $\Delta m = 1$ tunnelling sideband transitions are easily saturated as

discussed above. This saturation problem can be avoided by employing the stirring low-field NMR technique.

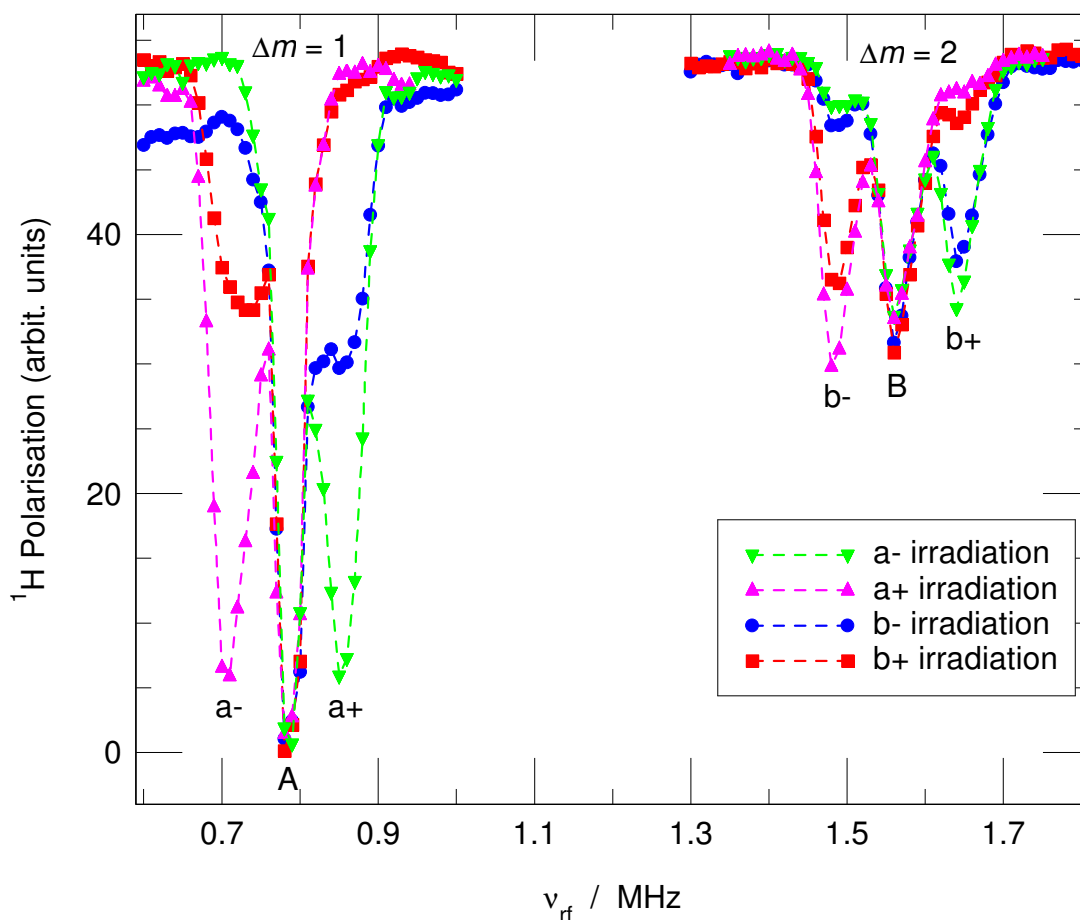


Figure 4.5 Stirling low-field NMR spectra of methylmalonic acid recorded at $T = 4.2\text{K}$ and $B_{\text{low}} = 0.0183\text{T}$

A number of experiments have been conducted with double rf irradiation at different sideband frequencies, by using the pulse sequence of the stirring low-field NMR technique (Fig. 4.3), and the corresponding spectra are presented in Fig. 4.5. The stirring rf frequency ν_{stir} was set to be a-, a+, b- and b+, respectively. In the $\Delta m = 1$ region the sideband peaks, labelled a- and a+, are observed at the frequencies $\nu_{\text{rf}}^{(a-)} = 0.7045 \pm 0.001$ MHz and $\nu_{\text{rf}}^{(a+)} = 0.8585 \pm 0.001$ MHz. The difference in frequency between peaks A and a- is 77 ± 1 kHz, the same as that between peaks A and a+, and this is consistent with the tunnelling frequency obtained in the $\Delta m = 2$ region. Therefore, this shows that peaks a- and a+ arise from the tunnelling transitions $h(\nu_L - \nu_t)$ and $h(\nu_L + \nu_t)$, respectively. Different from the conventional low-field NMR spectrum (Fig. 4.4), a very clear asymmetric sideband pattern is observed. When the stirring frequency is set to be either of the frequencies associated with transitions a- or b- (i.e. $\nu_{\text{stir}} = \nu_t - \nu_L$ or $\nu_{\text{stir}} = \nu_t - 2\nu_L$), both a+ and b+ peaks are substantially enhanced (green inverted

triangles and blue circles). When the sample is stirred at either of a+ or b+ (i.e. $\nu_{\text{stir}} = \nu_t + \nu_L$ or $\nu_{\text{stir}} = \nu_t + 2\nu_L$), peaks a- and b- are hugely enhanced (purple triangles and red squares). It is evident that with rf irradiation stirred at a+ or b+, the expected $\Delta m = 1$ tunnelling sideband transition $h(\nu_L - \nu_t)$ is revealed, by using rf irradiation stirred at either of the frequencies $\nu_{\text{stir}} = \nu_t + \nu_L$ or $\nu_{\text{stir}} = \nu_t + 2\nu_L$.

The substantial enhancement of the sideband peaks in the presence of the stirring rf irradiation may be explained by using the model of methyl thermodynamics illustrated above (Fig. 4.2). In Fig. 4.2 taking the $\Delta m = 1$ tunnelling sideband transitions of $h(\nu_t \pm \nu_L)$ for example, the evolution of the system when irradiated at the frequencies of $\nu_t - \nu_L$ or $\nu_t + \nu_L$ is indicated by the dotted arrow and dashed arrow, respectively. Without stirring rf irradiation, before the system meets its saturation condition, the trajectory for the transition associated with the frequency of $\nu_t - \nu_L$ is shorter than that of $\nu_t + \nu_L$. Therefore peak a- is expected to be smaller than peak a+. This is revealed in the conventional low-field NMR spectrum (Fig. 4.4) where peak a+ is weakly observed whereas the presence of peak a- is not evident. The direction of the system evolution when under the influence of stirring frequency $\nu_t + 2\nu_L$ is indicated by the solid arrow in Fig. 4.2. Different from the case without the stirring rf irradiation, where the system evolves in only one direction under the scanning frequency $\nu_{\text{rf}} = \nu_t - \nu_L$ or $\nu_{\text{rf}} = \nu_t + \nu_L$, in the case of double rf irradiation, the trajectory of the transition alternates direction as the scanning frequency $\nu_{\text{rf}} = \nu_t - \nu_L$ or $\nu_{\text{rf}} = \nu_t + \nu_L$, and the stirring frequency $\nu_{\text{stir}} = \nu_t - 2\nu_L$ are switched. As a result the trajectory becomes longer for the transition associated with the frequency of $\nu_t - \nu_L$, whereas it is shorter for the transition with the frequency of $\nu_t + \nu_L$ (Fig. 4.2). This can give rise to a large a- peak and a small a+ peak. This effect of the stirring rf irradiation on the tunnelling transitions is revealed in the spectrum (red squares, $\Delta m = 1$ regime in Fig. 4.5) where a significant a- peak is observed, and peak a+ is smaller than that in Fig. 4.4.

Consequently, with the stirring frequency of $\nu_{\text{stir}} = \nu_t + \nu_L$ or $\nu_{\text{stir}} = \nu_t + 2\nu_L$ (labelled a+ or b+), peaks a- and b- can be enhanced. Similarly, peaks a+ and b+ can be increased in the presence of the stirring frequency of either a- or b-. This enhancement effect of the sideband peaks is clearly demonstrated in Fig. 4.5. This is consistent with the results of numerical simulations (Fig. 4.6) of the stirring low-field NMR experiments at $B_{\text{low}} = 0.0183\text{T}$, where the frequency of the stirring rf irradiation was set to be either b- or b+.

It is also observed in Fig. 4.5 that peaks a- and b- under the influence of rf irradiation at a+ (purple triangles) are more strongly enhanced than those under the rf irradiation at b+ (red squares). Similarly, peaks a+ and b+ irradiated with rf radiation at a- (green inverted triangles)

are more largely enhanced than those under irradiation at b- (blue circles). This result is because the probabilities of transitions associated with $\Delta m = 1$ are larger than those with $\Delta m = 2$, therefore the effect of the rf irradiation at $a\pm$ on the transitions is stronger than that at $b\pm$. Consequently, peaks $a\mp$ and $b\mp$ are more strongly enhanced under the influence of rf irradiation at $a\pm$ than those at $b\pm$.

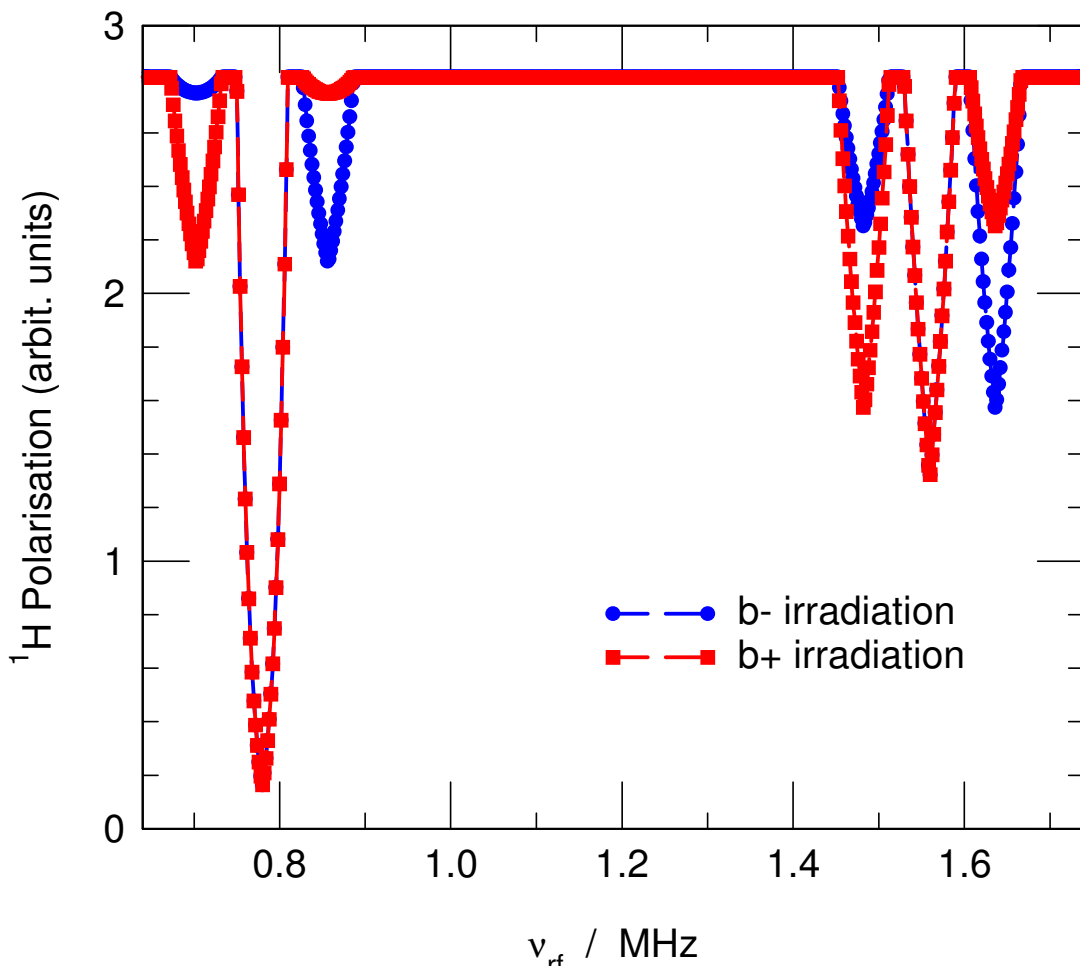


Figure 4.6 Results from numerical simulations of the stirring low-field NMR spectra of methylmalonic acid at $B_{\text{low}} = 0.0183\text{T}$; $\nu_t = 77\text{kHz}$

Above it has been demonstrated that the tunnelling transitions can be controlled by using the sideband stirring low-field NMR technique. Furthermore, the irradiation time-dependence of the asymmetric sideband spectrum has also been studied, and the irradiation time-dependence of the stirring low-field NMR spectra is presented in Fig. 4.7 with the stirring frequency of $\nu_{\text{stir}}^{(b-)} = 1.486\text{MHz}$. The data were recorded at three irradiation times, i.e. $\tau_{\text{irrad}} = 0.1\text{s}$, 0.5s and 1s . Simulations of the irradiation time-dependence of stirring low-field NMR was also made (Fig. 4.8), by using the simulation procedure discussed in section 4.3, with the same stirring frequency of $\nu_{\text{stir}}^{(b-)} = 1.486\text{MHz}$. Good agreement with Fig. 4.7 is shown qualitatively.

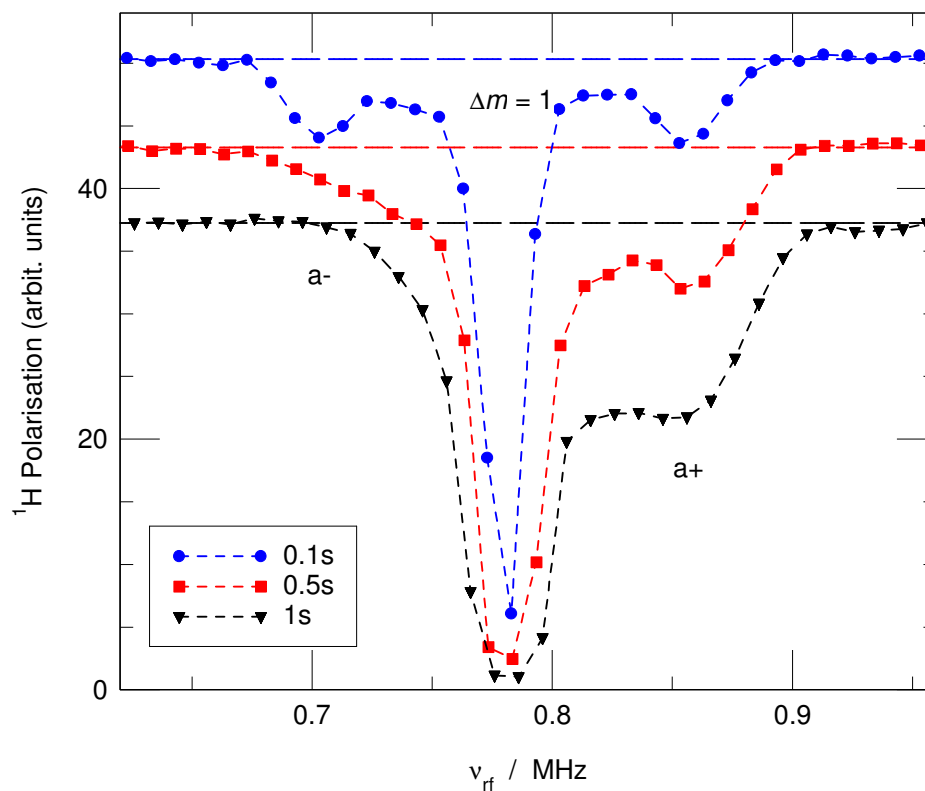


Figure 4.7 Irradiation time-dependence of the stirring low-field NMR spectra of methylmalonic acid recorded at $T = 4.2\text{K}$ and $B_{\text{low}} = 0.0183\text{T}$

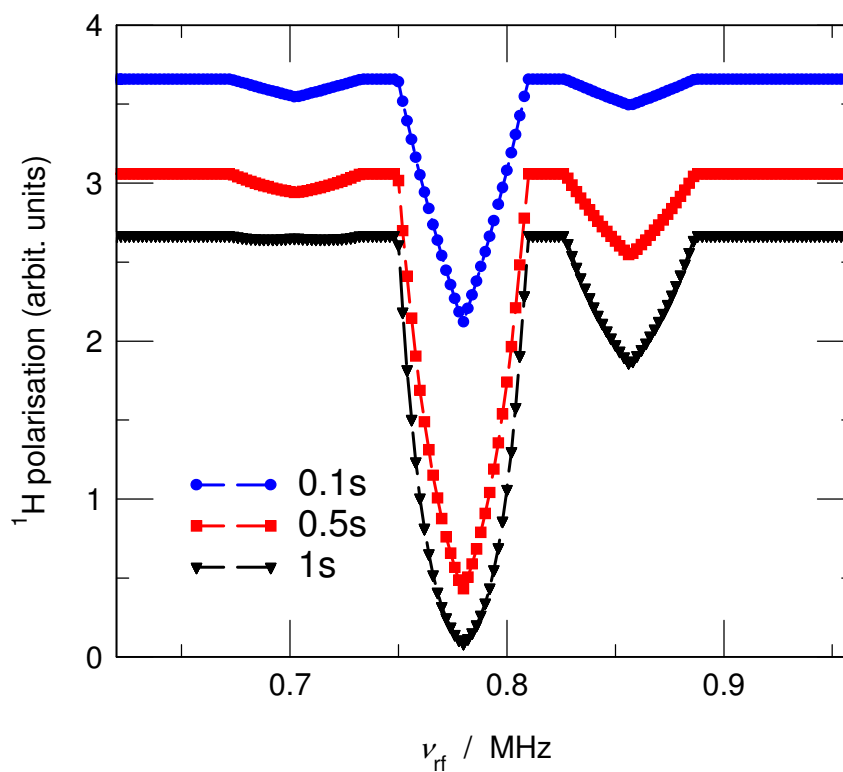


Figure 4.8 Results from numerical simulations of irradiation time-dependence of the stirring low-field NMR spectra of methylmalonic acid at $B_{\text{low}} = 0.0183\text{T}$

In Fig. 4.7, the baselines for each spectrum are different (flat dashed lines) because they depended on the irradiation time wherein the ^1H spins relax due to the spin-lattice relaxation. It is evident that the baseline is smaller when the irradiation time is longer. This is because the ^1H polarisation recovers further towards thermal equilibrium with time. In order to eliminate the complexity due to the baseline, and to investigate the effect of the irradiation time on the spectrum, a plot of the relative change in the ^1H polarisation $\Delta I_z / I_z$ as a function of irradiation time τ_{irrad} is presented in Fig. 4.9 for the tunnelling sideband a- and a+ peaks, where ΔI_z is the difference in ^1H polarisation between the baseline and the negative peak, and I_z is the ^1H polarisation of the baseline.

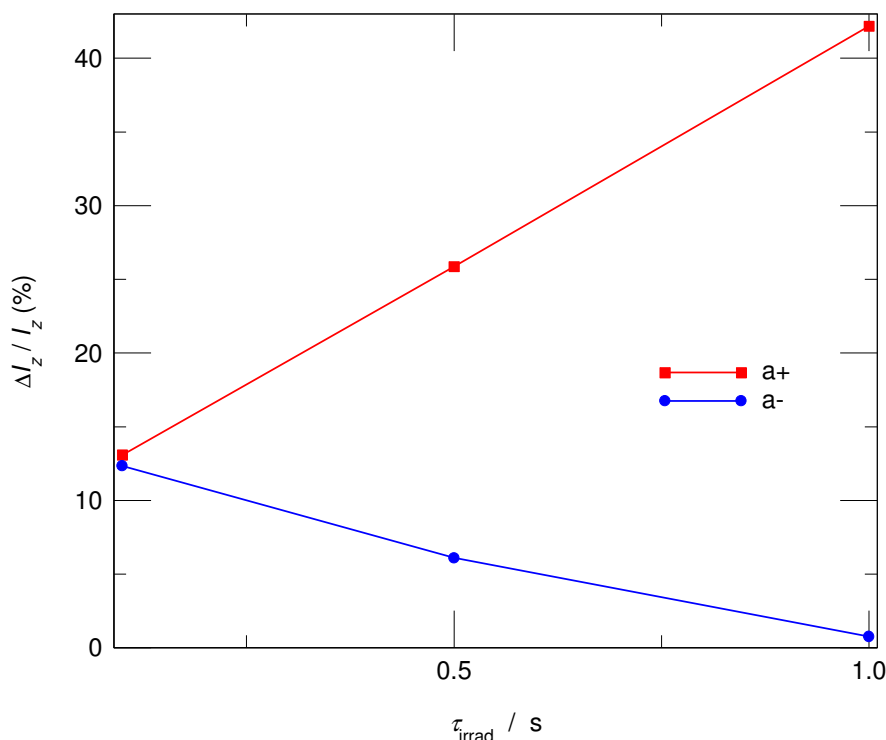


Figure 4.9 Irradiation time-dependence of the relative change in ^1H polarisation, $\Delta I_z / I_z$, at the a- and a+ tunnelling transitions in methylmalonic acid at $B_{\text{low}} = 0.0183\text{T}$

It is clear that in the presence of the stirring rf irradiation at frequency $\nu_{\text{stir}}^{(b-)} = 1.486\text{MHz}$, with increasing the irradiation time τ_{irrad} , the sideband a+ peak (red squares) is substantially enhanced while peak a- (blue circles) is reduced. In the $\beta_t - \beta_z$ space (Fig. 4.1 and 4.2) rf irradiation stirred at b- allows the tunnelling transition a+ to evolve without reaching the saturation condition. Therefore by increasing τ_{irrad} , the ^1H spin system evolves further, consequently the change in the relative ^1H polarisation is increased. However for the tunnelling transition a-, the effect of the b- rf irradiation is to make this transition saturate more easily. The decrease of the relative ^1H polarisation in Fig. 4.9 (blue circles) with increasing τ_{irrad} shows that the saturation condition is reached sooner.

It should be noted that in all low-field NMR experiments on methylmalonic acid, the tunnelling peak associated with the tunnelling transition $\Delta m = 0$ (solid arrows, $B_0 = 0$ in Fig. 2.7) has not been observed at the expected frequency $\nu_{\text{rf}} = 77\text{kHz}$. This shows that for methylmalonic acid, the Selection Rules may not be modified enough to make this high-field forbidden transition allowed at low field. The modification of the Selection Rules varies in different samples, and this can be revealed in the low-field NMR spectra of methyl ethyl ketone, which is discussed in the following section.

4.4.2 Methyl ethyl ketone

Similar to methylmalonic acid, both conventional and stirring low-field NMR experiments have been conducted on methyl ethyl ketone. Especially at the very low field $B_{\text{low}} = 0.00234\text{T}$, a very clear spectrum characteristic of methyl tunnelling has been revealed. The conventional low-field NMR spectrum at 0.00234T is presented in Fig. 4.10, and the stirring low-field NMR spectra conducted at the field $B_{\text{low}} = 0.0143\text{T}$ are presented in Fig. 4.11.

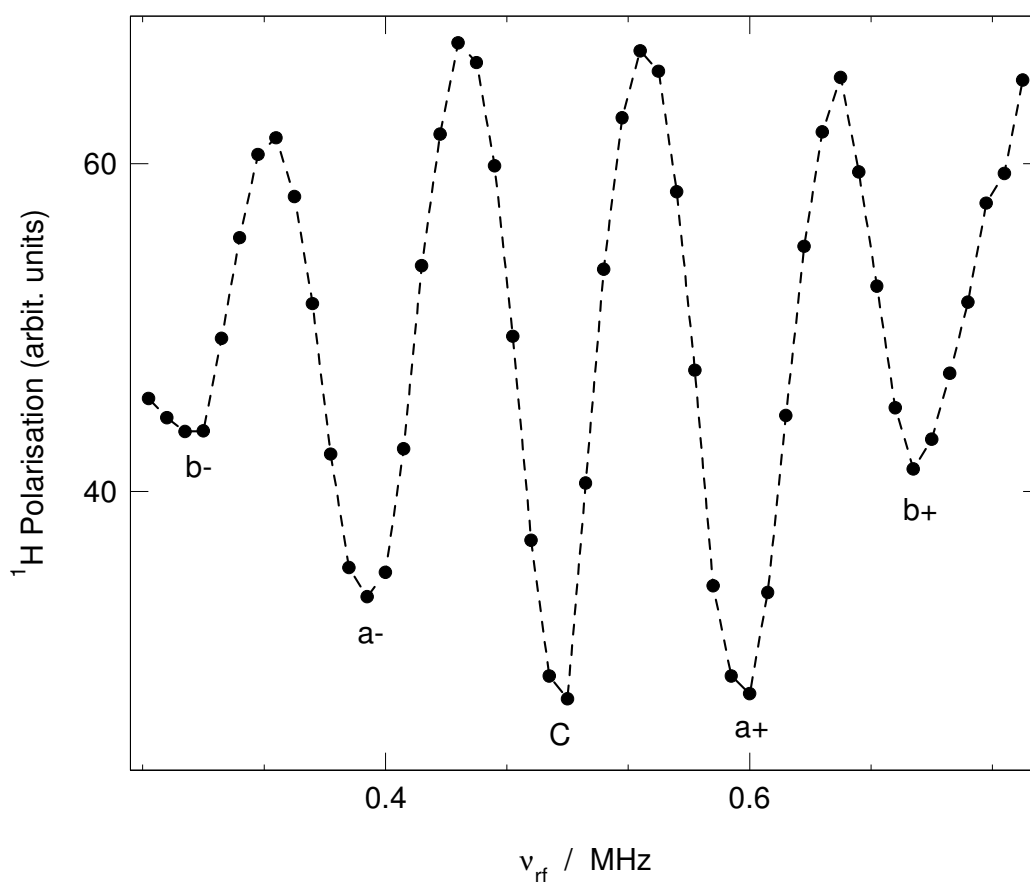


Figure 4.10 Low-field NMR spectrum of methyl ethyl ketone recorded at $T = 4.2\text{K}$ and $B_{\text{low}} = 0.00234\text{T}$

In Fig. 4.10 five negative peaks are observed. The middle peak, labelled C, has been determined to be field independent by experiments conducted at different fields. Therefore, peak C arises from the $\Delta m = 0$ tunnelling transition associated with the characteristic tunnelling frequency ν_t . It is measured to be $\nu_t = 494 \pm 1$ kHz, and this is consistent with the literature data [44]. The observation of the tunnelling peak C at low field reveals a dramatic modification of the Selection Rules, which ensure that this $A-E$ conversion is symmetry forbidden at high field. Surrounding peak C, two pairs of sideband peaks are also observed at frequencies $\nu_{\text{rf}}^{(a-)} = 0.3945 \pm 0.001$ MHz and $\nu_{\text{rf}}^{(a+)} = 0.5935 \pm 0.001$ MHz; $\nu_{\text{rf}}^{(b-)} = 0.295 \pm 0.001$ MHz and $\nu_{\text{rf}}^{(b+)} = 0.693 \pm 0.001$ MHz. The differences in frequency between peak C and each pair of the sideband peaks are measured to be $\nu_{\text{rf}}^{(a+)} - \nu_{\text{rf}}^{(C)} = \nu_{\text{rf}}^{(C)} - \nu_{\text{rf}}^{(a-)} = 99.5 \pm 1$ KHz and $\nu_{\text{rf}}^{(b+)} - \nu_{\text{rf}}^{(C)} = \nu_{\text{rf}}^{(C)} - \nu_{\text{rf}}^{(b-)} = 199 \pm 1$ kHz. The former is consistent with the ^1H nuclear Larmor frequency at $B_{\text{low}} = 0.00234\text{T}$, i.e. $\nu_t = \gamma_H B_{\text{low}} = 99.7\text{kHz}$. The latter is twice the Larmor frequency, which is $2\nu_t = 199.4\text{kHz}$. Therefore, the pair of peaks $a\pm$ arises from the tunnelling transitions with frequencies $\nu_t \pm \nu_L$, whereas the pair of peaks $b\pm$ is associated with the transitions $h(\nu_t \pm 2\nu_L)$.

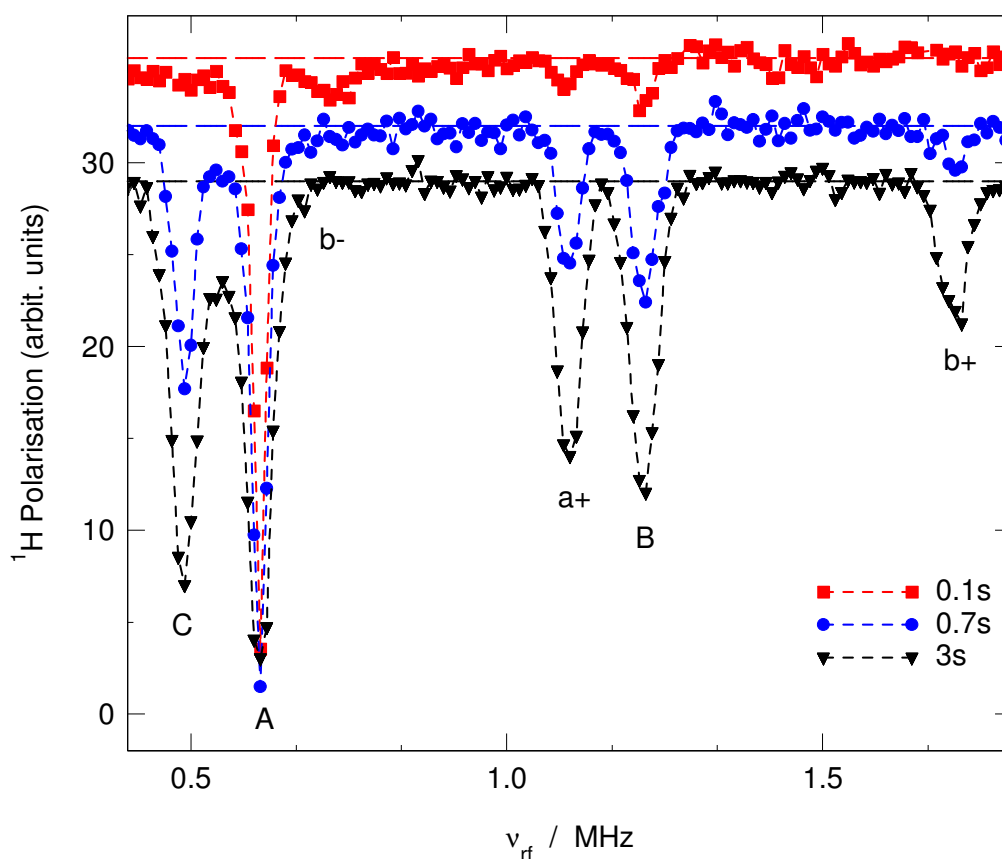


Figure 4.11 Irradiation time-dependence of the stirring low-field NMR spectra of methyl ethyl ketone recorded at $T = 4.2\text{K}$ and $B_{\text{low}} = 0.0143\text{T}$ with $\nu_{\text{stir}}^{(b-)} = 724\text{kHz}$

The stirring low-field spectra (Fig. 4.11) were measured at a slightly higher field $B_{\text{low}} = 0.0143\text{T}$, with the stirring frequency $\nu_{\text{stir}}^{(\text{b-})} = 724\text{kHz}$, which is associated with the tunnelling transition of $h(\nu_t - 2\nu_L)$. The data were recorded at three irradiation times, i.e. $\tau_{\text{irrad}} = 0.1\text{s}$, 0.7s and 3s , respectively. Six peaks, labelled A, B, C, a+ and b \pm are observed. The field-independent peak C is also observed at $\nu_{\text{rf}} = 494 \pm 1\text{ kHz}$, which arises from the $\Delta m = 0$ tunnelling transition with the frequency of $\nu_t = 494\text{kHz}$. The measured frequencies of A and B peaks are $\nu_{\text{rf}}^{(\text{A})} = 609 \pm 1\text{ kHz}$ and $\nu_{\text{rf}}^{(\text{B})} = 1218 \pm 1\text{ kHz}$. The former is consistent with the Larmor frequency at $B_{\text{low}} = 0.0143\text{T}$, i.e. $\nu_L = 609\text{kHz}$. The latter is the same as double the Larmor frequency, which is $2\nu_L = 1.218\text{MHz}$. It is clear that peaks A and B arise from the transitions associated with the $\Delta m = 1$ and $\Delta m = 2$ Zeeman splittings. Peaks a+ and b \pm are observed at the frequencies $\nu_{\text{stir}}^{(\text{a+})} = 1.103 \pm 0.001\text{ MHz}$, $\nu_{\text{stir}}^{(\text{b-})} = 724 \pm 1\text{ kHz}$ and $\nu_{\text{stir}}^{(\text{b+})} = 1.712 \pm 0.001\text{ MHz}$, and these are consistent with the tunnelling sideband transitions with frequencies $\nu_t + \nu_L$, $\nu_t - 2\nu_L$ and $\nu_t + 2\nu_L$, respectively. It is evident that with increasing the irradiation time, peak b- is decreased whereas peaks a+ and b+ are enhanced. This reveals that under rf irradiation stirred at b-, the b- transition approaches its saturation condition with increasing irradiation time, whereas stirring at this frequency causes the saturation of the a+ and b+ transitions to be delayed, and therefore the corresponding peaks are enhanced.

4.5 Conclusions

The modification of the Selection Rules at low field has been revealed, and the tunnelling frequencies of methyl groups have been precisely measured, by utilising field-cycling low-field NMR techniques. The characteristic frequencies of methyl tunnelling in two samples have been obtained, i.e. $\nu_t = 77 \pm 1\text{ kHz}$ for methylmalonic acid and $\nu_t = 494 \pm 1\text{ kHz}$ for methyl ethyl ketone. The measurements reveal that methyl groups in methylmalonic acid are much more hindered than that in methyl ethyl ketone since the former have a smaller tunnelling frequency.

It has been demonstrated that the tunnelling transitions can be manipulated by using stirring low-field NMR. The tunnelling a+ and b+ transitions can be enhanced with rf irradiation stirred at a- or b-, and vice versa. It has also been shown that tuning the irradiation time can be another method whereby tunnelling transitions are manipulated and revealed, by using stirring low-field NMR.

Chapter 5 Quantum dynamics and tunnelling of the methyl rotor in sodium acetate trihydrate and sorbic acid

5.1 Introduction

There are several molecular rotor systems that have sufficiently low mass to exhibit quantum tunnelling behaviour. Among them are two systems that have been extensively studied; methyl group (CH_3) rotation [4, 55] and concerted double proton transfer in the hydrogen bond [40, 56–60]. The methyl rotor has a high degree of spatial symmetry and the molecular dynamics are substantially influenced by the requirements of spin symmetry, and this is an example of coherent tunnelling whereby the probability of finding the protons oscillates among the three symmetric potential wells. However, proton transfer in the hydrogen bond has less symmetry, but the delocalisation of the wave function can also provide tunnelling pathways through the potential barrier. This is an example of incoherent tunnelling. In systems that have one or more such molecular groups, the motion will play a role as a relaxation centre which influences spin-lattice relaxation, especially at low temperature.

In NMR experiments, molecular quantum dynamics and tunnelling are often investigated through experiments that probe the nuclear spin relaxation properties. By measuring the spin-lattice relaxation time T_1 as a function of temperature and magnetic field, information regarding the correlation times for the motion can be obtained [61, 62]. In more complex systems where more than one dynamical system may contribute to T_1 , multiple components are expected in the spectral density. A detailed investigation of the magnetic field dependence of spin-lattice relaxation time can permit the different spectral density components to be resolved. Moreover, by tuning the magnetic field, which in turn changes the energy splitting of the Zeeman reservoir, the corresponding Larmor frequency can be made to match the tunnelling frequency with which molecular rotors undergo coherent tunnelling oscillations at this condition, an exotic resonant behaviour arises, called tunnel resonance [21–23].

In this chapter, quantum dynamics and tunnelling of methyl rotors have been studied, by measuring the temperature dependence of T_1 , and by determining the spectral density. Additionally, low-field NMR and tunnel resonance experiments have been used to study the tunnelling frequencies. Two samples have been investigated; the first sample, sodium acetate trihydrate, has a relatively large methyl tunnelling frequency at low temperature [15, 61, 63], significantly larger than the proton Larmor frequency. With increasing temperature, the tunnelling frequency is reduced and broadened due to thermal fluctuations and population of

the excited tunnelling states, which is revealed in the spectral density. The second sample, sorbic acid, has a much smaller methyl tunnelling frequency at low temperature, and resonant features characteristic of the ground tunnelling state are observed. Additionally, the spin-lattice relaxation components arising from the concerted proton transfer in the hydrogen bonds of the carboxylic acid dimer are also observed.

5.2 Theoretical

5.2.1 Methyl groups

As discussed in Section 2.6.4, the spin-lattice relaxation time T_1 arising from the methyl group tunnelling and reorientation has been determined by Haupt [12],

$$T_1^{-1} = C_{AE} \sum_{n=1}^2 \left(\frac{n^2 \tau_c}{1 + (\omega_t + n\omega_L)^2 \tau_c^2} + \frac{n^2 \tau_c}{1 + (\omega_t - n\omega_L)^2 \tau_c^2} \right) + C_{EE} \sum_{n=1}^2 \frac{n^2 \tau_c}{1 + n^2 \omega_L^2 \tau_c^2} \quad (5.1)$$

where C_{AE} and C_{EE} are the dipolar constants, $\omega_L = \gamma_H B_z$ is the proton Larmor frequency, ω_t is the methyl tunnelling frequency and τ_c is the correlation time.

Based on Eqn. (2.24), in order to describe the temperature dependence of the inverse correlation time τ_c^{-1} for methyl rotation, a phenomenological expression comprising the first two terms in the following equation proposed by Müller-Warmuth [14] has been employed,

$$\tau_c^{-1} = \tau_{0H}^{-1} \exp\left(\frac{-E_H}{k_B T}\right) + \tau_{0L}^{-1} \exp\left(\frac{-E_L}{k_B T}\right) + \tau_{0I}^{-1} \exp\left(\frac{-E_I}{k_B T}\right) \quad (5.2)$$

The first term, labelled H , characterises the high temperature Arrhenius behaviour with activation energy E_H . The second term, labelled L , describes the low temperature regime behaviour with activation energy E_L , which is usually observed to be close to the energy E_{01} , i.e. the ground to first excited state torsional splitting of the methyl group. This is consistent with the methyl thermometer model developed by Clough [64]. Additionally in Eqn. (5.2) a term labelled I is introduced to accommodate an intermediate temperature regime which is a precursor to the high temperature limit.

With increasing temperature, as the first excited torsional state becomes populated, the observed tunnelling frequency becomes a thermal average of the ground and first excited state tunnelling frequencies, $\omega_t^{(0)}$ and $\omega_t^{(1)}$. This gives rise to temperature dependent behaviour of the tunnelling frequency ω_t . This is an important characteristic of the methyl dynamical spectrum. An expression for the thermal average tunnelling frequency is proposed by Allen [46, 65] as,

$$\omega_t^{obs}(T) = \frac{\omega_t^{(0)} - \omega_t^{(1)} \exp(-E_{01}/k_B T)}{1 + \exp(-E_{01}/k_B T)} \quad (5.3)$$

As mentioned in Chapter 2, E states are lower than the A state in the first excited torsional state; in the ground state the opposite is true. Therefore there is a change in sign in the numerator in Eqn. (5.3). It is clear that the tunnelling frequency is decreased with increasing temperature.

As shown in section 2.2.3, the rotational Hamiltonian of the methyl group is time-independent,

$$\hat{H}_R = \frac{-\hbar^2}{2I} \frac{\partial^2}{\partial \phi^2} + V(\phi) \quad (5.4)$$

where the hindering potential may be written as a Fourier series consisting of three-fold, six-fold and higher harmonics,

$$V(\phi) = \sum \frac{V_{3l}}{2} [1 - \cos(3l(\phi + \chi_{3l}))]. \quad (5.5)$$

In the matrix representation, matrix elements for this Hamiltonian may be determined by,

$$H_R^{jk} = \langle \psi_j | \hat{H}_R | \psi_k \rangle \quad (j, k = 3l) \quad (5.6)$$

where free rotor wave functions may be used as the basis $\{\psi_j\}$ [61, 64]. Considering the three-fold symmetry of methyl groups, this Hamiltonian matrix may be transformed into two irreducible sub-matrices of symmetry groups A and E . Therefore, given the hindering potential V_{3l} , the rotational eigenvalues can then be calculated by diagonalising each Hamiltonian sub-matrix [61, 64].

5.2.2 Hydrogen bonds

It is well known that there is concerted double proton transfer in the hydrogen bonds of the carboxylic acid dimer [40]. By analogy with the model system benzoic acid, this motion can be modelled by the Skinner-Trommsdorff model [60], and the spin-lattice relaxation time arising from proton transfer in the hydrogen bonds has been determined by,

$$T_1^{-1} = C_D \operatorname{sech}^2 \left(\frac{A}{2k_B T} \right) \left(\frac{\tau_c}{1 + \omega_L^2 \tau_c^2} + \frac{4\tau_c}{1 + (2\omega_L)^2 \tau_c^2} \right) \quad (5.7)$$

where C_D is a dipolar constant and A is the energy asymmetry that characterises the double well potential for the proton in the hydrogen bonds in the dimer. The inverse correlation time, τ_c^{-1} , can be determined by,

$$\tau_c^{-1} = k_0 \coth\left(\frac{A}{2k_B T}\right) + \tau_0^{-1} \exp\left(\frac{-\Delta E_{act}}{k_B T}\right). \quad (5.8)$$

The first term in this expression arises from incoherent tunnelling in the ground state with k_0 equal to the rate of one-phonon emission at 0K, and this term dominates at low temperature. The second term is an Arrhenius expression representing pseudo-classical barrier hopping with activation energy ΔE_{act} , and this term dominates at high temperature.

5.3 Experimental

Measurements of proton T_1 as a function of both temperature and magnetic field were made using the field-cycling NMR spectrometer. For low fields $B \leq 0.4\text{T}$, the polarisation-recovery pulse sequence (Fig. 3.15) was employed; otherwise the saturation-recovery pulse sequence (Fig. 3.13) was used to measure T_1 .

By tuning the magnetic field, when the Zeeman reservoir is brought into resonant contact with the methyl tunnelling reservoir the phenomenon of tunnel resonance can occur and anomalies in the ^1H polarisation can be observed. For sorbic acid the tunnel resonance spectra were obtained using the tunnel resonance level-crossing pulse sequence (Fig. 3.17).

At high field the transitions between A and E tunnelling states are forbidden due to the Selection Rules. However, as discussed in Chapter 4, at low field, and in the presence of secondary rf irradiation, the Selection Rules can be modified and hence such transitions can be allowed. For samples with a small tunnelling splitting, it is likely to measure the tunnelling frequency associated with such transitions. In this chapter for sorbic acid, whose methyl tunnelling frequency is relatively small, the methyl tunnelling frequency was measured using the pulse sequence of the low-field dipole-dipole driven experiments (Fig. 3.19).

5.4 Results and discussion

5.4.1 Sodium acetate trihydrate

The inverse ^1H spin-lattice relaxation time T_1^{-1} is plotted as a function of inverse temperature in Fig. 5.1. The data were recorded at seven magnetic fields in the range $0.0375\text{T} \leq B_z \leq 2.0\text{T}$. For each field two maxima are observed in T_1^{-1} ; one maximum appears in the region $T^{-1} = 0.025\text{K}^{-1}$, and it is independent of the magnetic field. The other maximum emerges at lower temperature, and it is strongly dependent on the applied magnetic field and hence the ^1H

Larmor frequency. The latter has the classic BPP form of the EE term in Eqn. (5.1), whereas the field independent maximum arises from the AE term in Eqn. (5.1), and it is often called the ‘Haupt maximum’. At the temperature $T = 40.0\text{K}$, where the Haupt maximum occurs, the methyl tunnelling frequency is resonant with the ^1H Larmor frequency,

$$\omega_t^{(obs)}(T) \cong \pm n\omega_L = \pm n\gamma_H B_z \quad (5.9)$$

where $n = 1$ or 2 .

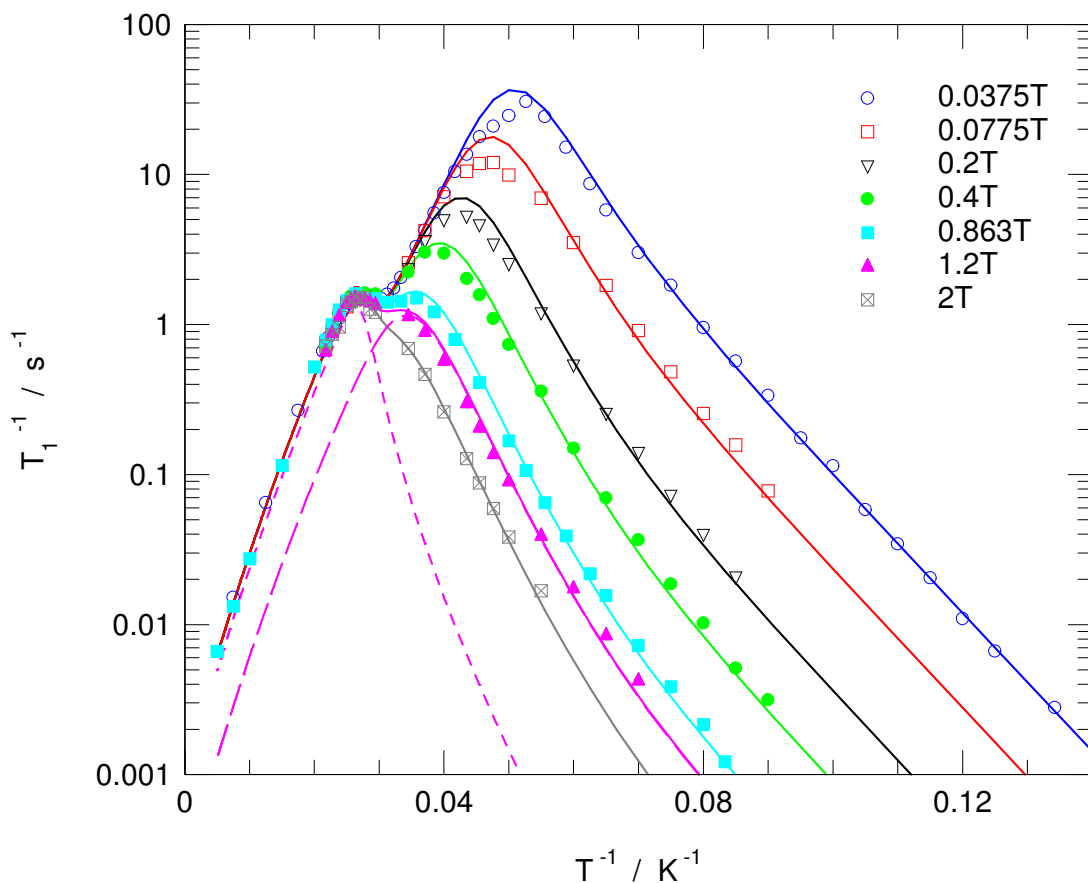


Figure 5.1 Inverse temperature dependence of the inverse spin-lattice relaxation time T_1^{-1} for ^1H in sodium acetate trihydrate; solid lines were obtained from simulations (EE components in the long-dash line and AE in the short-dash line)

By measuring the inverse spin-lattice relaxation time T_1^{-1} as a function of magnetic field the spectral density functions have been plotted. The data were recorded at a variety of temperatures in the range $11.1\text{K} \leq T \leq 46.0\text{K}$. The spectral density results are presented in Fig. 5.2 in two temperature ranges: (a) $11.1\text{K} \leq T \leq 29.0\text{K}$ and (b) $34.0\text{K} \leq T \leq 46.0\text{K}$, which correspond to the temperature regions where the two maxima are observed in the $T_1^{-1}(1/T)$ curve (Fig. 5.1). The low temperature data in Fig. 5.2a are reflected about the $B_z = 0$ axis in order to emphasise the Lorentzian characteristic of the spectral density components. The high temperature data in Fig. 5.2b are presented in two dimensions, T_1^{-1} and B_z .

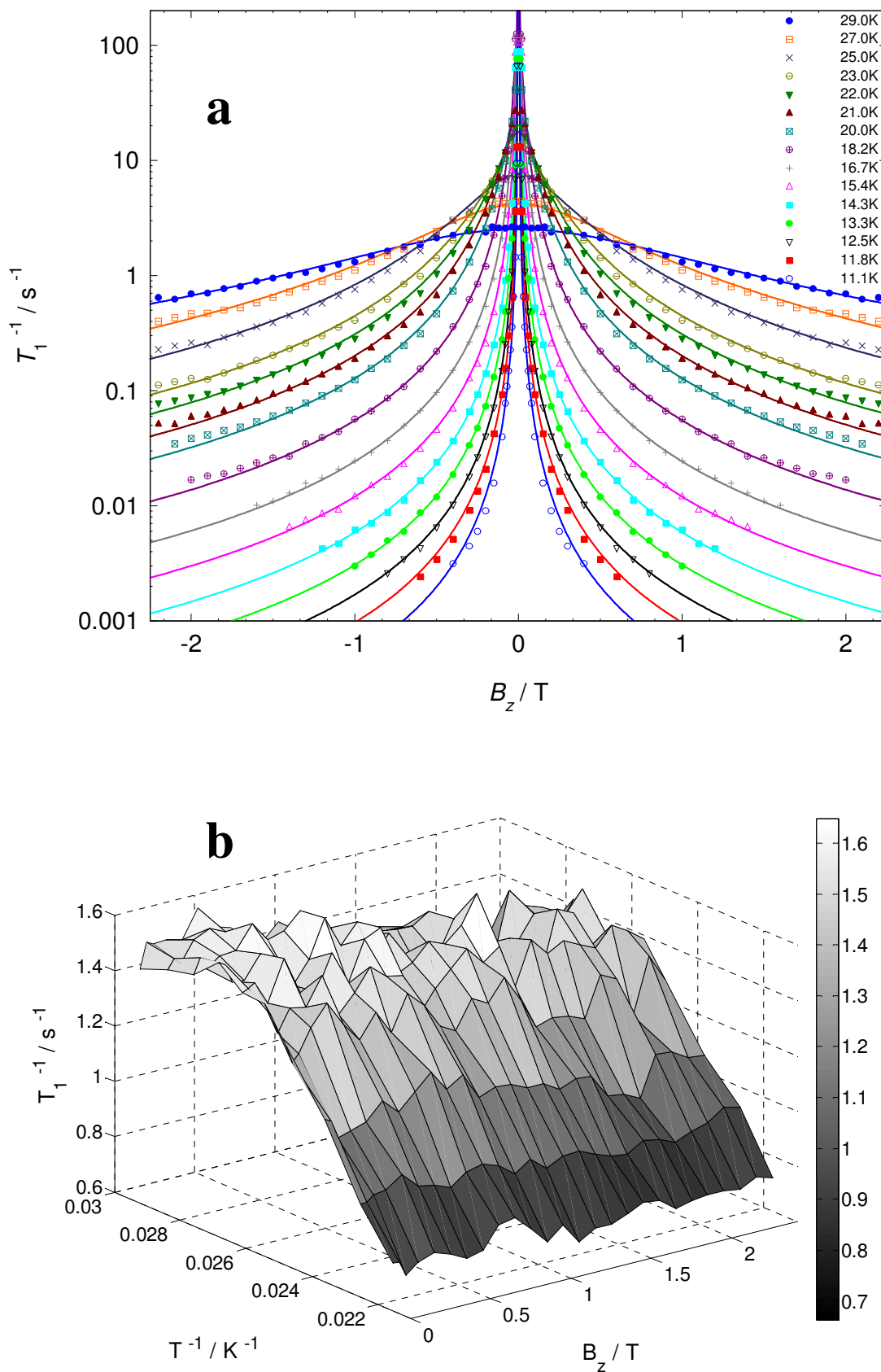


Figure 5.2 Spectral densities of sodium acetate trihydrate recorded at (a) $11.1\text{K} \leq T \leq 29.0\text{K}$ and (b) $34.0\text{K} \leq T \leq 46.0\text{K}$; solid lines in (a) were obtained from curve fittings

In Fig. 5.2a it is evident that the spectral density broadens as temperature increases, since the inverse correlation time τ_c^{-1} that characterises the methyl reorientation is increased with increasing temperature. It is clear that the spectral density function is centred at zero field. This reveals that T_1^{-1} is dominated by the EE term in Eqn. (5.1) in low temperature range $11.1\text{K} \leq T \leq 29.0\text{K}$. This is consistent with the temperature dependence plot of T_1^{-1} in Fig. 5.1, where the field dependent EE maximum occurs at low temperatures.

In Fig. 5.2b in the relatively high temperature range $34.0\text{K} \leq T \leq 46.0\text{K}$, wherein the Haupt maximum ($T = 40.0\text{K}$) appears, the corresponding AE components in Eqn. (5.1) are expected to reveal themselves as discrete peaks offset from $B_z = 0$ in the spectral density plots $T_1^{-1}(B_z)$. However, no such peaks are observed in the B_z dimension within the magnetic field window studied. Instead for each temperature, a broad spectrum is observed, and this broad feature moves through in the temperature dimension. This reveals that in this temperature range the system is more likely to be in the fast-motion limit where τ_c^{-1} is very large so that,

$$\tau_c^{-1} \gg \omega_t, \omega_L. \quad (5.10)$$

Eqn. (5.1) can then be simplified into,

$$T_1^{-1} = (10C_{AE} + 5C_{EE})\tau_c. \quad (5.11)$$

Eqn. (5.11) shows that T_1^{-1} has a flat pattern of the spectral density in the fast-motion limit where the Lorentzian linewidth is much broader than the dynamic range defined by the B_z -window studied. As a result the resonant AE term in $T_1^{-1}(B_z)$ is not observed as discrete peaks, but very broad resonant features.

Further, the correlation time can be studied. In Fig. 5.1 it is evident that the AE term in T_1^{-1} will only make a significant contribution at temperatures above the Haupt maximum. Therefore the spectral density data at $T \leq 29.0\text{K}$ in Fig. 5.2a can be fitted with only the EE term in Eqn. (5.1). The data are fitted well by a single correlation time at all temperatures (solid lines in Fig. 5.2a), and the best fit inverse correlation times τ_c^{-1} are determined for the temperatures $11.1\text{K} \leq T \leq 29.0\text{K}$, and are plotted in Fig. 5.3 (red circles) as a function of the inverse temperature. The mean value of the dipolar constant for the EE term is found to be $C_{EE} = 2.6 \times 10^8 \text{s}^{-2}$. In Fig. 5.3 for temperatures $T < 10.5\text{K}$, additional values of τ_c^{-1} are determined (blue triangles) from the $T_1^{-1}(1/T)$ data recorded at the lowest magnetic field $B_z = 0.0375\text{T}$ (blue circles in Fig. 5.1), by inverting the EE term in Eqn. (5.1) using the best fit value $C_{EE} = 2.6 \times 10^8 \text{s}^{-2}$.

It can be shown by simple algebra that $\omega_t \tau_c = 1$ at the turning point of Eqn. (5.1). Using this, and the value of T_1^{-1} at the Haupt maximum, the dipolar constant C_{AE} can be estimated to be

$C_{AE} = 5 \times 10^8 \text{s}^{-2}$, by inverting Eqn. (5.1). Together with $C_{EE} = 2.6 \times 10^8 \text{s}^{-2}$, further values of τ_c^{-1} (green squares in Fig. 5.3) are determined for temperatures $T \geq 57.1 \text{K}$, from the $T_1^{-1}(1/T)$ data in Fig. 5.1, by inverting Eqn. (5.1). In Fig. 5.3 a change in gradient at $T^{-1} \approx 0.06 \text{K}^{-1}$ is observed. This reveals a continuous transition from low temperature motion to higher temperature motion. The data are fitted to Eqn. (5.2) (solid line in Fig. 5.3) and the best fit pre-exponential factors and activation energy parameters are presented in Table 5.1.

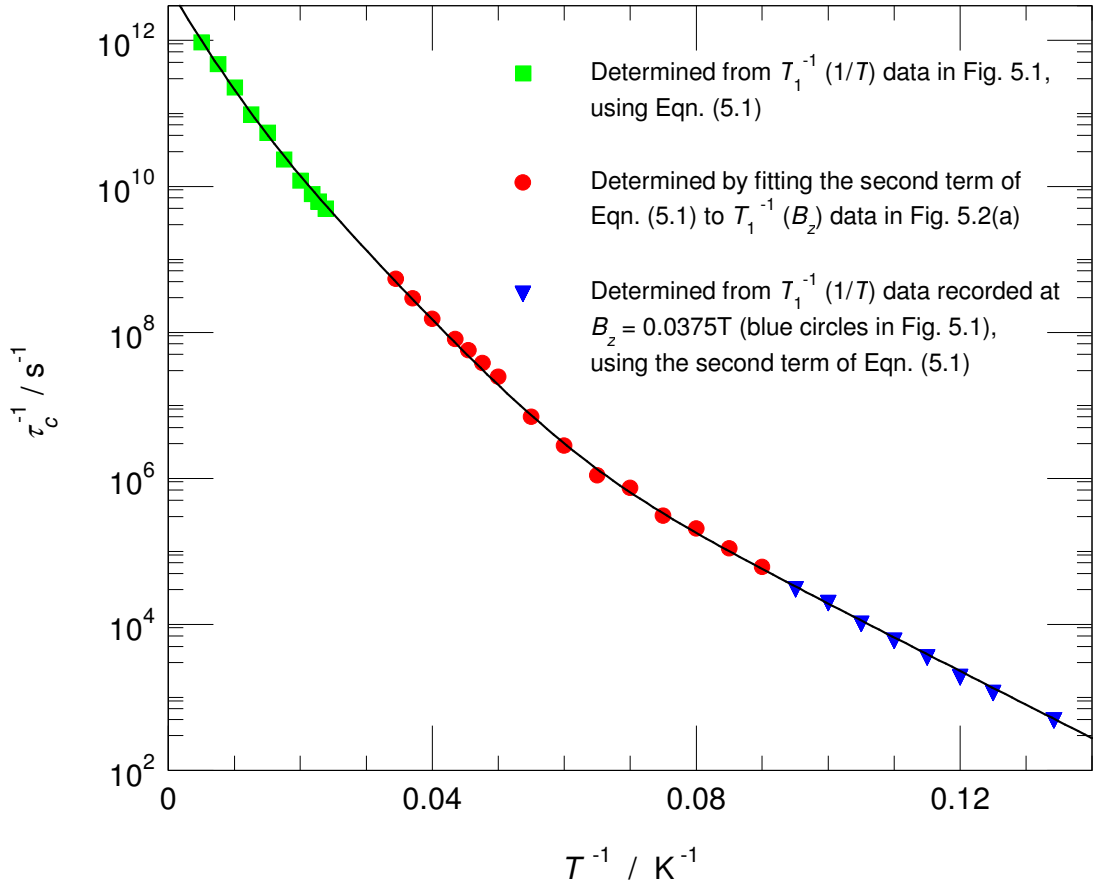


Figure 5.3 Inverse temperature dependence of the inverse correlation time τ_c^{-1} in sodium acetate trihydrate; the solid line indicates the fitting

The tunnelling splitting $\hbar\omega_t$ and ground to first excited state torsional splitting E_{01} in sodium acetate trihydrate have been measured by neutron scattering [15]: $\hbar\omega_t = 5.7 \mu\text{eV}$ and $E_{01}/k_B = 115 \text{K}$. As discussed above, the hindering potential may be written as Fourier series consisting of three-fold, six-fold and higher harmonics (Eqn. (5.5)), in practise only the first few terms need to be considered. Both Clough [63] and Müller-Warmuth [61] have shown the neutron scattering observations in sodium acetate trihydrate are incompatible with a purely three-fold hindering barrier, and significant six-fold contributions are required to explain the experimental data. Therefore Eqn. (5.5) for the hindering barrier may be rewritten as,

$$V = \frac{V_3}{2}(1 - \cos 3\phi) + \frac{V_6}{2}(1 - \cos 6\phi). \quad (5.12)$$

As discussed in section 5.2.1, the rotational eigenvalues can be calculated by diagonalising the Hamiltonian, using free rotor wave functions as the basis [61, 64]. From such calculations the values $V_3/k_B = 496 \pm 10$ K and $V_6/k_B = -137 \pm 5$ K result in values of ω_i and E_{01} that approximate the neutron scattering measurements. From this, estimates of the ground to second excited state torsional splitting $E_{02}/k_B = 256 \pm 5$ K and the activation energy $E_{act}/k_B = 450 \pm 10$ K are also obtained.

From Fig. 5.3 and Table 5.1 it is evident that the low temperature gradient of the $\tau_c^{-1}(1/T)$ curve $E_L/k_B = 106 \pm 5$ K is consistent with the ground to first excited state torsional splitting $E_{01} = 115$ K. This reveals that the methyl tunnelling dominates at low temperature. At higher temperatures, the best fit parameter $E_I/k_B = 220 \pm 5$ K is consistent with the ground to second excited state torsional splitting $E_{02}/k_B = 256 \pm 5$ K calculated by the model potential above. This shows the population of the second excited torsional state with increasing temperature. At the highest observed temperatures, the correlation rate curve has a steeper gradient $E_H/k_B = 370 \pm 10$ K. It is apparent that the classical limit is not yet reached in the observed temperature range since it is smaller than the activation energy $E_{act}/k_B = 450 \pm 10$ K calculated by the model potential.

Further in Fig. 5.1, the inverse spin-lattice relaxation times $T_1^{-1}(1/T)$ are calculated using Eqn. (5.1) and the parameters in Table 5.1. The results are presented as solid lines in Fig. 5.1 (EE components in long-dash lines and AE in short-dash lines), and good agreement with the data is obtained. A satisfactory fit in the region of the Haupt maximum is achieved by modelling the tunnelling frequency $\omega_i^{obs}(T)$, using the Allen model (Eqn. (5.3)) with the measured values of $\hbar\omega_i^{(0)}$ and E_{01} , together with the first excited state tunnelling splitting $\hbar\omega_i^{(1)} = 0.1 \pm 0.01$ meV. It should be noted that the latter is 50% larger than that predicted by the model potential above ($\hbar\omega_i^{(1)(model)} = 0.068 \pm 0.01$ meV). This may be because $\omega_i^{obs}(T)$ changes very rapidly in the temperature region of Haupt maximum so that its behaviour is sensitive to small changes in $\hbar\omega_i^{(1)}$. Therefore it is likely for such a discrepancy to occur. Additionally as discussed above, apart from a three-fold barrier V_3 , the model barrier also includes an out of phase six-fold component V_6 . Compared with a three-fold barrier, this model barrier is characterised by a broader well and narrower barrier region that gives rise to a larger excited state tunnelling splitting $\hbar\omega_i^{(1)}$, which is consistent with the observation above.

5.4.2 Sorbic acid

As shown in Table 1.2, sorbic acid forms a carboxylic acid dimer whereby the two molecules are connected by pairs of hydrogen bonds. The methyl group occupies the position at the opposite end of the main carbon chain. Therefore multiple components in the spectral density function are expected due to the motions of different molecular groups.

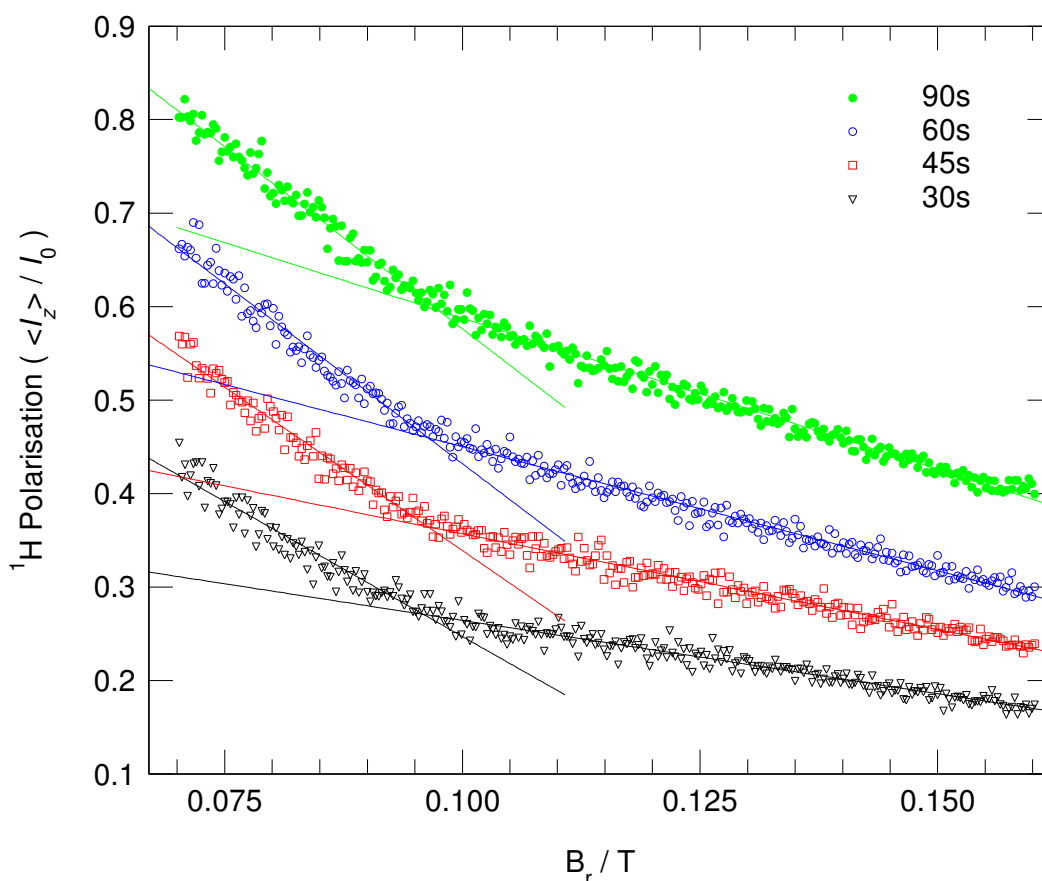


Figure 5.4 Tunnel resonance spectra of sorbic acid recorded at $T = 34.8\text{K}$; solid lines are guides to the eye

To estimate the tunnelling frequency, tunnel resonance experiments were conducted by employing the level-crossing pulse sequence (Fig. 3.17), and the corresponding tunnel resonance spectra are presented in Fig. 5.4. The data were measured at four recovery times $t_{rec} = 30\text{s}$, 45s , 60s and 90s at $T = 34.8\text{K}$. The ^1H polarisation $\langle I_z \rangle$ was scaled to the magnetisation at thermal equilibrium I_0 at the corresponding field B_r . For all spectra, there is a significant change in gradient observed at the field $B_r = 0.096 \pm 0.001\text{ T}$. It is evident that this change in gradient arises from the tunnel resonance phenomenon since the tunnel resonance is always traversed during the field-cycling switch from the measurement field $B_{nmr} = 0.863\text{T}$ to the lower field values. For all fields $\gamma B_z < \omega_l$ in the spectrum, the proton relaxation is affected

by tunnel resonance and hence the measured nuclear polarisation is affected, however there is no such effect for the fields $\gamma B_z > \omega_t$. Because the gradient changes at the tunnel resonance condition where $\omega_t = \omega_L$, the methyl tunnelling frequency is estimated as $\nu_t = 4.10 \pm 0.04$ MHz. A more direct measurement of the tunnelling frequency was made by utilising the low-field NMR technique.

Low-field dipole-dipole driven experiments were conducted at $T = 30.0\text{K}$, and the low-field NMR spectra are presented in Fig. 5.5. The data were recorded at low fields $B_r = 0.0375\text{T}$ and 0.0425T . For each field, three negative peaks are observed. It is evident that two peaks, labelled $\Delta m = 1, 2$, are field dependent. This arises from transitions associated with $\Delta m = 1, 2$ Zeeman splittings. It is also clear that the peak, labelled $\Delta m = 0$, is independent of the field. This reveals that it arises from the $\Delta m = 0$ tunnelling transition so that the methyl tunnelling frequency is directly measured to be $\nu_t = 4.10 \pm 0.04$ MHz. This is consistent with the estimate of ν_t from tunnel resonance experiments.

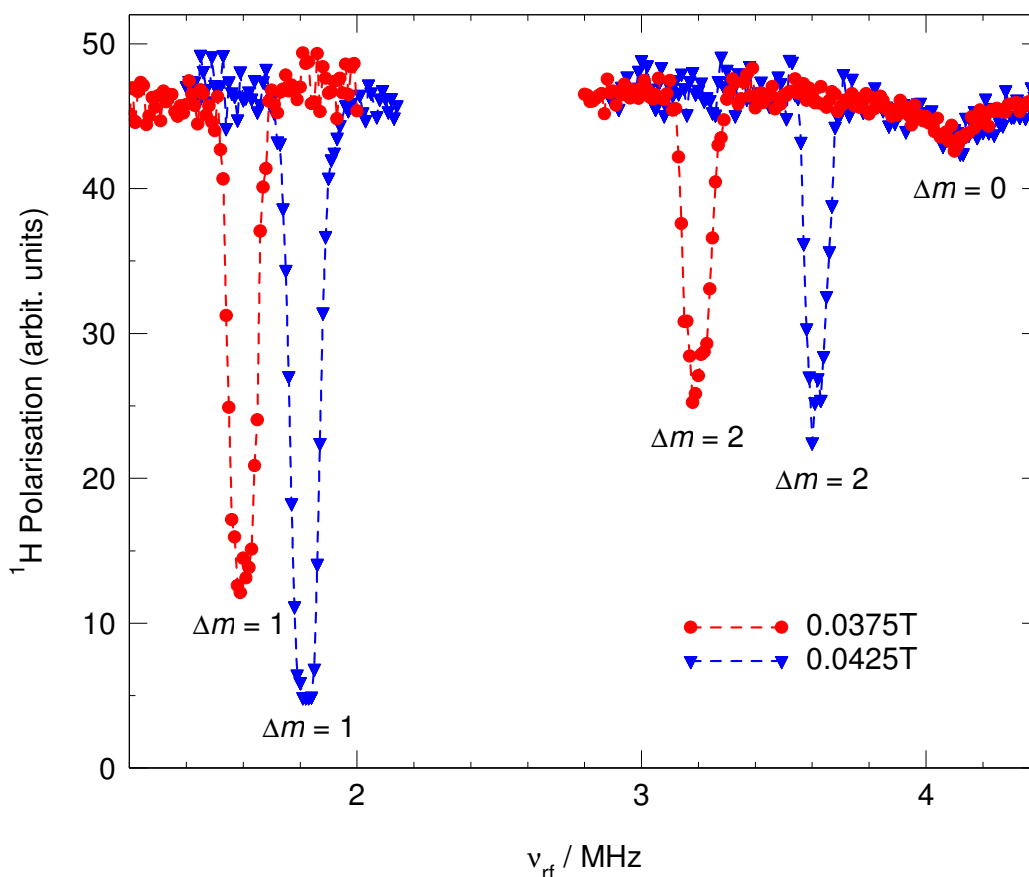


Figure 5.5 Low-field NMR spectra of sorbic acid recorded at $T = 30.0\text{K}$

To investigate molecular dynamics, the inverse temperature dependence of T_1^{-1} was measured, and is presented in Fig. 5.6. The data were recorded at four different magnetic fields. At the

two highest fields 2.3T and 0.863T, field-dependent maxima centred at approximately 100K and 92K are observed. At much lower magnetic fields 0.0375T and 0.0075T, a new feature emerges at low temperature as the gradient of the T_1^{-1} data changes substantially.

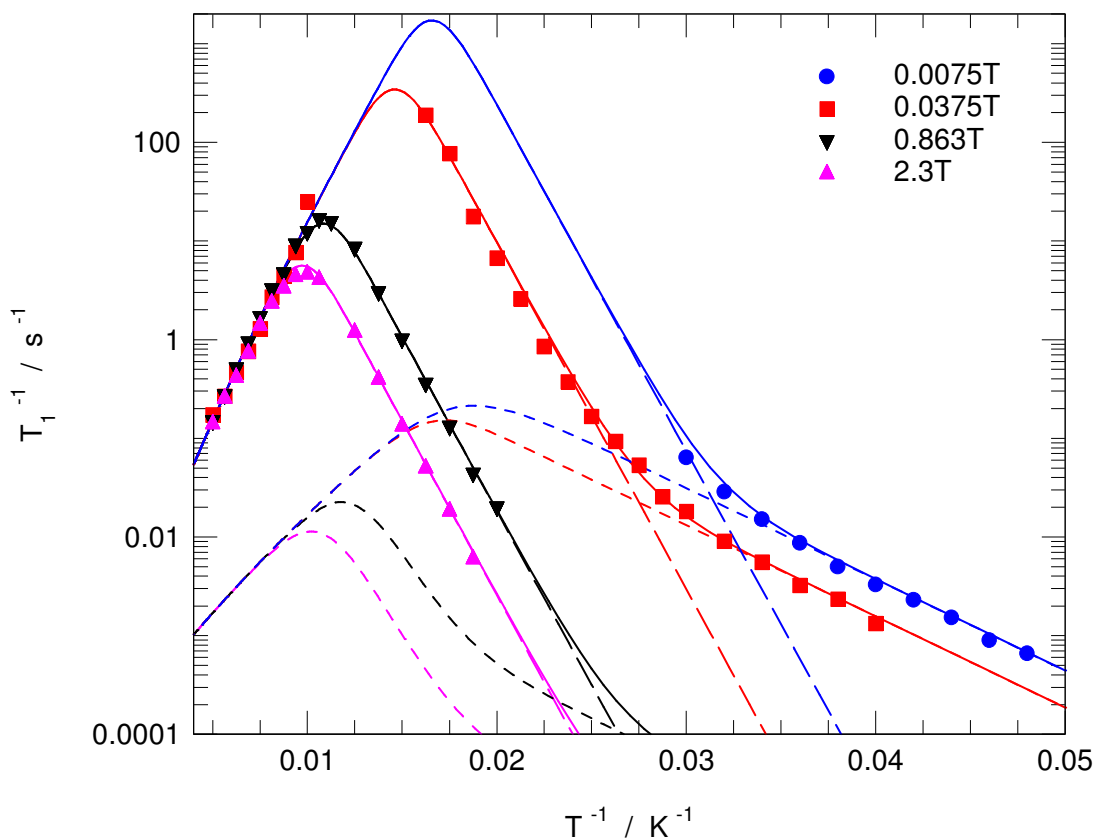


Figure 5.6 Inverse temperature dependence of the inverse spin-lattice relaxation time T_1^{-1} for ^1H in sorbic acid; solid lines were obtained from simulations (components arising from proton transfer are indicated by dashed lines)

This relaxation behaviour may indicate that there are multiple dynamical processes present other than a single process characterised by a single correlation time. In order to fully investigate, measurements of T_1^{-1} as a function of magnetic field were conducted. The data were recorded at seven different temperatures. The spectral densities of the four highest temperatures $50.0\text{K} \leq T \leq 61.5\text{K}$ are presented in Fig. 5.7a (the data have been reflected about the $B_z = 0$ axis). The low temperature spectral densities ($33.3\text{K} \leq T \leq 40.0\text{K}$) are presented in Fig. 5.7b.

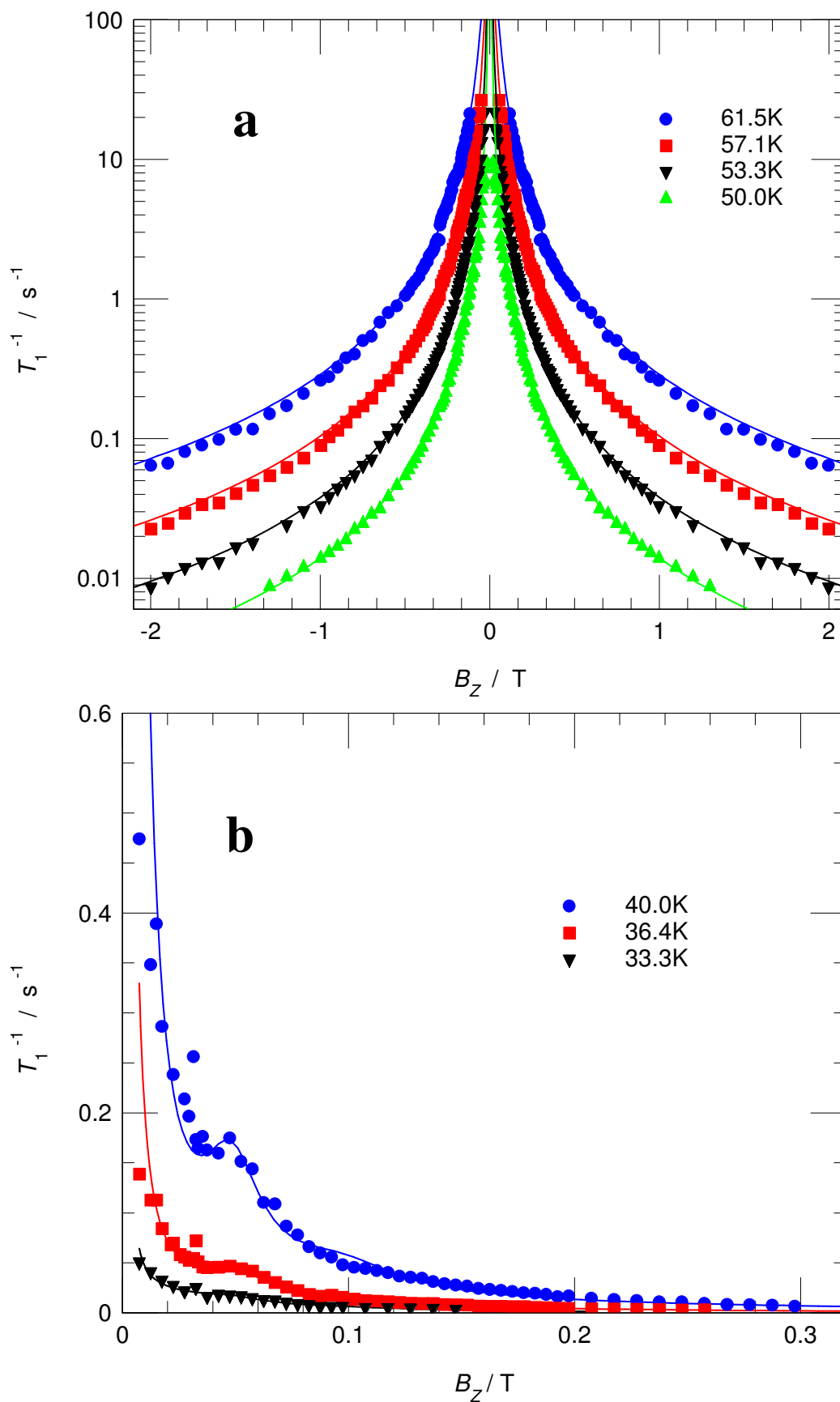


Figure 5.7 Spectral densities of sorbic acid recorded at (a) $50.0\text{K} \leq T \leq 61.5\text{K}$ and (b) $33.3\text{K} \leq T \leq 40.0\text{K}$; solid lines in (a) were obtained from curve fittings; solid lines in (b) represent simulations

In Fig. 5.7a, good agreement is achieved by fitting the data to the EE term in Eqn. (5.1) (solid lines). This reveals that the process at high temperature is dominated by methyl reorientation. However at the three lowest temperatures (Fig. 5.7b), satisfactory fits to the spectral densities can only be achieved by introducing a second dynamical process characterised by a second correlation time. At the three lowest temperatures, T_1 becomes excessively long for magnetic fields greater than 0.3T. Therefore in practice, it was only possible to record reliable data for at $B_z \leq 0.3T$. In Fig. 5.7b it is evident that there is a substantial overlap between different spectral density components (i.e. Lorentzian functions with a narrow width and a broad width) relating to two processes. Additionally, a small reproducible peak is observed at $B_z = 0.048T$. This discrete peak (offset from $B_z = 0$) is fitted well to the AE components in Eqn. (5.1) with $\nu_t = 4.1\text{MHz}$, and this reveals the change in the proton relaxation arising from tunnel resonance. From the resonant condition, i.e. $\nu_t = 2\nu_L$, the methyl tunnelling frequency may be estimated as $\nu_t = 4.1\text{MHz}$, and this is consistent with the direct measurement using low-field NMR.

It should be noted that from temperature dependent measurement of T_1^{-1} in sorbic acid, no Haupt maximum is explicitly evident (Fig. 5.6). This is consistent with published data [4] on systems with similar tunnel frequencies where the AE components in the relaxation expression, Eqn. (5.1), overlap with the EE term, and this is also consistent with the spectral density data in Fig. 5.7a, where the high temperature data are dominated by the EE term. Therefore the methyl correlation rates may be determined by applying the EE term in Eqn. (5.1) to the $T_1^{-1}(1/T)$ data (Fig. 5.6). First by differentiating Eqn. (5.1) with respect to τ_c , the condition $(T_1^{-1})_{\max} = 1.43C_{EE}/\omega_t$ is obtained at the $T_1^{-1}(1/T)$ maximum. Therefore a value of $C_{EE} = (2.42 \pm 0.1) \times 10^9 \text{s}^{-2}$ is determined from the T_1^{-1} values at the relaxation maxima recorded at fields $B_z = 2.3T$ and $0.863T$. The methyl correlation rates in the range $0.005\text{K}^{-1} \leq 1/T \leq 0.025\text{K}^{-1}$ are determined from the T_1^{-1} data at fields $B_z = 2.3T$, $0.863T$ and $0.0375T$, by inverting Eqn. (5.1), and the resulting inverse correlation times for methyl reorientation are presented in Fig. 5.8. Good agreement is obtained for data sets recorded at different magnetic fields.

Because the methyl reorientation only dominates in the high temperature region, the low temperature term in Eqn. (5.2), labelled L , may be neglected. Values of $E_H/k_B = 1160 \pm 20\text{K}$ and $E_l/k_B = 810 \pm 15\text{K}$ (the high and lower temperature gradients of the $\tau_c^{-1}(1/T)$ curve) are obtained, by fitting the $\tau_c^{-1}(1/T)$ data to Eqn. (5.2). A pure three-fold barrier may be assumed for the methyl group in sorbic acid. As with the calculation [61, 64] in the case of sodium acetate trihydrate, the value of the barrier $V_3/k_B = 1146 \pm 20\text{K}$ is predicted for the measured tunnelling frequency $\nu_t = 4.1 \pm 0.04\text{MHz}$. From this, the first torsional splitting $E_{01}/k_B = 261$

± 5 K is also obtained. It is clear that the high temperature gradient $E_H/k_B = 1160$ K is consistent with the barrier height $V_3/k_B = 1146$ K. This is characteristic of the methyl reorientation at high temperature. Furthermore, the lower temperature gradient $E_l/k_B = 810$ K is between the barrier height $V_3/k_B = 1146$ K and the first torsional splitting $E_{01}/k_B = 261$ K. This indicates that the low temperature region is not reached in Fig. 5.8.

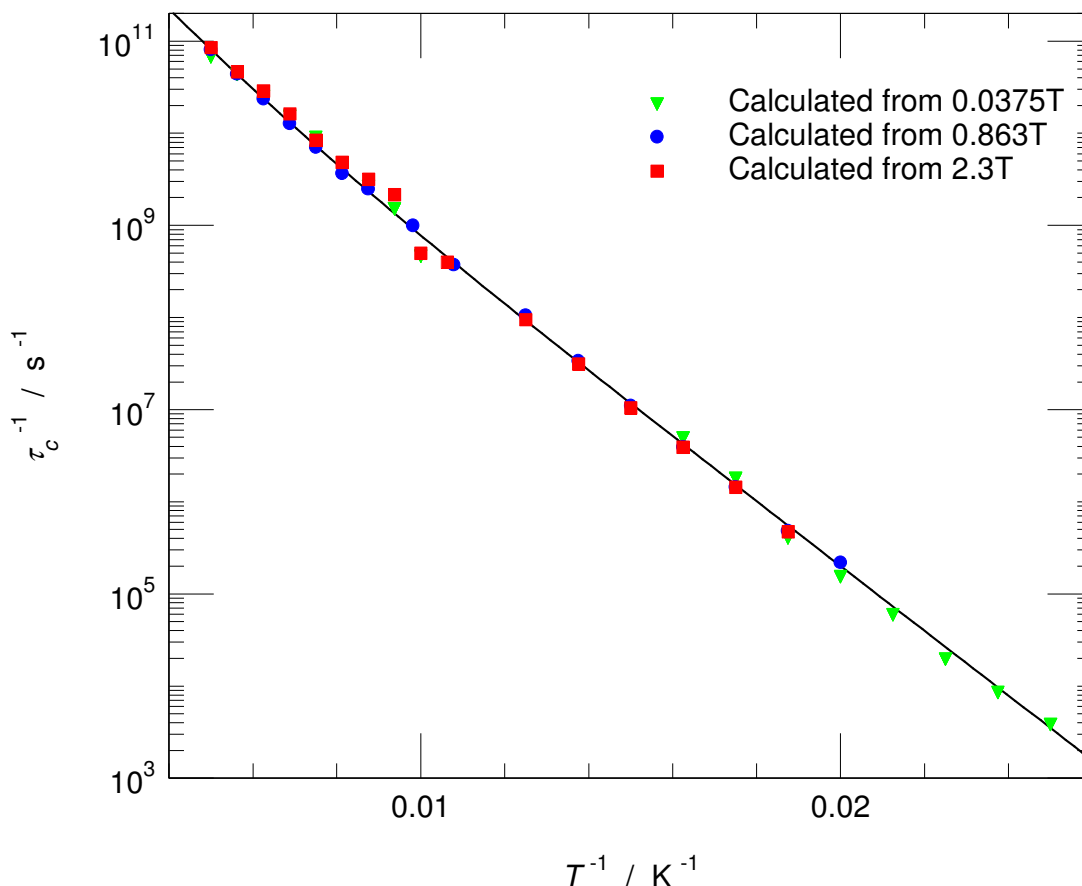


Figure 5.8 Inverse temperature dependence of the inverse correlation time τ_c^{-1} for CH_3 reorientation in sorbic acid; solid line indicates the fitting

At low temperatures $1/T > 0.025\text{K}^{-1}$, it is evident from both the temperature and field dependent T_1^{-1} data (Fig. 5.6, 5.7b) that a second dynamical process contributes to T_1^{-1} . This motion can be modelled by the Skinner-Trommsdorff model (Eqn. (5.7)) [60]. This indicates that the low temperature nuclear relaxation is dominated by the concerted double proton transfer in the hydrogen bonds of the carboxylic acid dimer. The first term on the right-hand side in Eqn. (5.8) dominates at low temperatures, therefore by fitting this term together with Eqn. (5.7) to the $T_1^{-1}(1/T)$ data recorded at the two lowest fields $B_z = 0.0375\text{T}$ and 0.0075T (Fig. 5.6), the energy asymmetry in hydrogen bonds and the dipolar constant are estimated to be $A/k_B = 213 \pm 5$ K and $C_D = (1.4 \pm 0.06) \times 10^7 \text{s}^{-2}$.

It is worth noting that in the model the activation energy $\Delta E_{\text{act}}/k_B$ at high temperature was set to 600K [57], which is typical for a proton transfer system (e.g. Benzoic acid). The exact value is not necessary in this case since in the high temperature region the T_1^{-1} data, dominated by methyl motion, is insensitive to this term. By combining the relaxation equations for methyl reorientation (EE term in Eqn. (5.1)) and for proton transfer (Eqn. (5.7)), the model is established, and the results are shown by solid lines in the relevant figures (Fig. 5.6, 5.7b). Best fit parameters are presented in Table 5.1. It is clear that good agreement with the data is obtained.

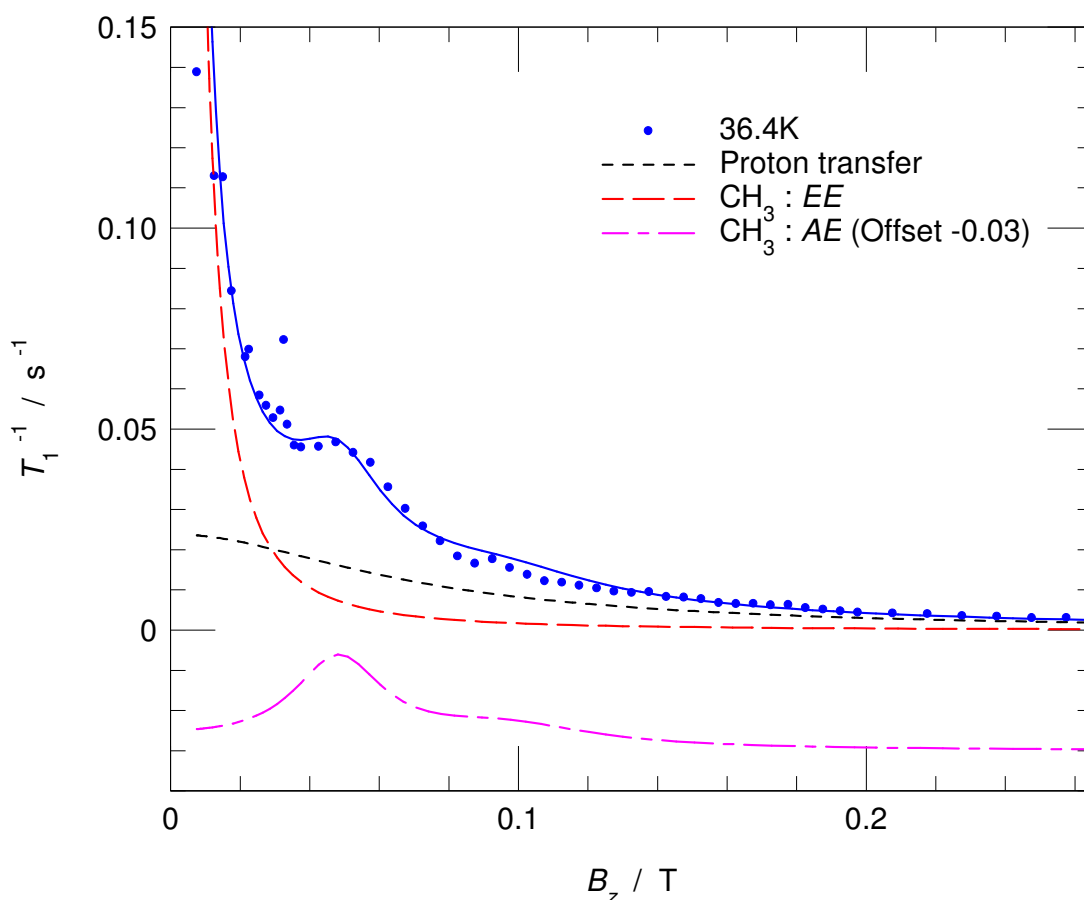


Figure 5.9 Spectral density of sorbic acid recorded at $T = 36.4\text{K}$; the solid line was obtained from the simulation (component arising from proton transfer and EE components of methyl reorientation are indicated by dashed lines, and AE components are plotted in dot-dash line; offset by -0.03 for clarity)

At low fields $0.03\text{T} \leq B_z \leq 0.1\text{T}$, small systematic features are observed in the $T_1^{-1}(B_z)$ data in Fig. 5.7b. This is the field region where tunnel resonance associated with the AE term in Eqn. (5.1) is expected. To investigate this, the low field region of spectral density at $T = 36.4\text{K}$ is replotted in Fig. 5.9. A weak T_1^{-1} anomaly is evident at $B_z = 0.048\text{T}$. Compared with the measured tunnelling frequency $\nu_t = 4.1\text{MHz}$, this field corresponds to the $\nu_t = 2\nu_L$ resonant

condition. The result calculated from the model, which includes the *AE* components in Eqn. (5.1), is represented by the solid line. Two dashed lines represent the T_1^{-1} contributions arising from proton transfer and the *EE* components of methyl reorientation, respectively. The *AE* components are plotted in dot-dash line (offset by -0.03 for clarity). It is evident that the reproducible T_1^{-1} peak centred at $B_z = 0.0480 \pm 0.0015$ T is the manifestation of methyl tunnelling, i.e. $\nu_t = 2\nu_L$. The tunnelling feature at $\nu_t = \nu_L$ appears in the model with smaller amplitude and twice the width.

It should be noted that in the model the best fit value $C_{AE} = (4.5 \pm 0.2) \times 10^4 \text{s}^{-2}$ is smaller than the typical literature values [61, 62]. As discussed in Chapter 2, because the methyl tunnelling reservoir is only weakly coupled to the lattice, the tunnelling temperature is usually different from the lattice temperature and it is affected by the thermal and magnetic treatment history of the sample. Because the effect of the tunnelling temperature on tunnel resonance is not accommodated in Eqn. (5.1), it is possible that there is a greater uncertainty in the interpretation of the dipolar constant C_{AE} .

Additionally, the *AE* Lorentzian components in the model have a width characterised by $\tau_{ct}^{-1} = (8.3 \pm 0.7) \times 10^6 \text{s}^{-1}$, which is significantly broader than the *EE* Lorentzian components. This may be associated with an open question in NMR research, i.e. whether the correlation time, characterising the Lorentzian width, is the same for *AE* and *EE* terms [66, 67]. The *AE* tunnelling lineshapes may have different width from the *EE* barrier hopping lineshapes. However, in sorbic acid the proton transfer introduces disorder, consequently there will be a distribution of methyl barrier heights arising from the hydrogen bond motion, and this may provide the mechanism for broadening the tunnelling peak since the methyl tunnelling frequency is exponentially dependent on the barrier height.

Finally, it should be noted that at one particular value of magnetic field $B_z = 0.0325$ T, a reproducible T_1^{-1} anomaly is observed (Fig. 5.7b), corresponding to a very narrow resonant feature. The integrated intensity of this feature does not suggest that this is associated with the bulk sample, it may be due to the tunnel resonance associated with the minority of methyl groups, possibly resulting from defects or impurities.

5.5 Conclusions

The benefits of evaluating the inverse correlation time for the molecular motion directly from field-dependent measurements of the spectral density have been clearly demonstrated. The field-dependent measurements have also enabled us to precisely determine the methyl barrier.

It has been illustrated that the tunnelling frequency can be estimated using tunnel resonance experiments and directly measured using the low-field NMR experiment. It should be noted that the tunnelling frequency $\nu_t = 4.10 \pm 0.04$ MHz in sorbic acid is the largest value directly measured using low-field dipole-dipole driven experiments. The field-dependent measurements also allow us to investigate multiple dynamics. It has been shown how different Lorentzian spectral density components may be resolved. In the case of sorbic acid, the methyl group reorientation and the proton transfer in hydrogen bonds have been well revealed by separating components in the spectral density. Furthermore, the methyl group tunnelling features have been manifested in the plots of spectral density.

	Sodium acetate trihydrate	Sorbic acid
τ_H^{-1}	$(4.5 \pm 0.4) \times 10^{12} \text{ s}^{-1}$	$(1.46 \pm 0.08) \times 10^{13} \text{ s}^{-1}$
E_H / k_B	$370 \pm 10 \text{ K}$	$1160 \pm 20 \text{ K}$
τ_L^{-1}	$(7.7 \pm 0.6) \times 10^8 \text{ s}^{-1}$	
E_L / k_B	$106 \pm 5 \text{ K}$	
τ_I^{-1}	$(9 \pm 0.7) \times 10^{11} \text{ s}^{-1}$	$(2.0 \pm 0.2) \times 10^{12} \text{ s}^{-1}$
E_I / k_B	$220 \pm 5 \text{ K}$	$810 \pm 15 \text{ K}$
$\hbar\omega_t^{(0)}$	$5.7 \text{ } \mu\text{eV}$ [63]	$4.10 \pm 0.04 \text{ MHz}$
$\hbar\omega_t^{(1)}$	$0.10 \pm 0.01 \text{ meV}$	
C_{EE}	$(2.6 \pm 0.1) \times 10^8 \text{ s}^{-2}$	$(2.4 \pm 0.1) \times 10^9 \text{ s}^{-2}$
C_{AE}	$(5.0 \pm 0.2) \times 10^8 \text{ s}^{-2}$	$(4.5 \pm 0.2) \times 10^4 \text{ s}^{-2}$
<i>CH₃ Model Potential</i>		
V_3 / k_B	$496 \pm 10 \text{ K}$	$1146 \pm 20 \text{ K}$
V_6 / k_B	$-137 \pm 5 \text{ K}$	
E_{01} / k_B	115 K [63]	$261 \pm 5 \text{ K}$
E_{02} / k_B	$256 \pm 10 \text{ K}$	$502 \pm 10 \text{ K}$
<i>Proton Transfer</i>		
k_0		$(1.4 \pm 0.1) \times 10^7 \text{ s}^{-1}$
A / k_B		$213 \pm 10 \text{ K}$
τ_0^{-1}		$(6.0 \pm 0.5) \times 10^{10} \text{ s}^{-1}$
$\Delta E_{act} / k_B$		600 K [57]
C_D		$(1.40 \pm 0.06) \times 10^7 \text{ s}^{-2}$

Table 5.1 Best fit parameters for sodium acetate trihydrate and sorbic acid

CHAPTER 6 Tunnelling reservoirs in copper doped zinc acetate dihydrate and toluene doped with DPPH radicals

6.1 Introduction

The amplitude of NMR signals is determined, in part, by the polarisation of the nuclear spins. To improve the sensitivity of NMR, various strategies have been employed for enhancing the polarisation. The latter can be achieved by the phenomenon of dynamic nuclear polarisation (DNP) [4, 24, 25]. Therefore there has been much interest in the study of DNP recently. One interesting issue among the investigations of DNP is the physics underpinning the energy transfer between different thermal reservoirs associated with the various spin systems. For methyl groups, this involves energy exchange among both tunnelling and Zeeman reservoirs. The work in this chapter will address this issue.

As discussed in Chapter 2 the methyl rotor, CH_3 , rotating under the influence of a hindering potential barrier must obey the Exclusion Principle which imposes strict constraints on the spatial and nuclear spin degrees of freedom. Consequently a tunnelling reservoir defined by a pair of states, which have different energies and symmetries, originates. The barrier in general has three-fold symmetry and the ground torsional state is split by a tunnelling splitting $\hbar\omega_t$, separating two nuclear spin-symmetry species labelled A and E , where the A species is a nuclear spin quartet with total spin $I = 3/2$, while degenerate E_a and E_b species are nuclear spin doublets with total spin $I = 1/2$. Normally A - E conversion is spin restricted. As a result, for methyl groups, the tunnelling reservoirs associated with the A and E nuclear spin symmetry species are thermally isolated from the lattice, particularly at low temperature. With cooling of the sample, the inter-conversion of the A and E species is spin-restricted and the tunnelling reservoir is characterised by a temperature θ_t , which can remain significantly higher than the lattice temperature for many hours, days or even weeks [4].

A variety of novel experimental techniques have been developed since the 1970s to study methyl tunnelling. Regarding the phenomenon of DNP, tunnel resonance experiments [17, 18] have been widely used. The key principle of the tunnel resonance experiments is to connect the tunnelling reservoir and the Zeeman reservoir that is associated with an electron or nuclear spin by tuning the magnetic field. When the Larmor frequency ω_L matches the tunnelling frequency ω_t , resonant contact will be established. Under this tunnel resonance condition, time-dependent interactions coupling space and spin become available so that A - E conversion can be substantially enhanced, consequently a dramatic nuclear spin polarisation or a change

in the nuclear spin-relaxation properties can be observed. Therefore methyl tunnelling can be revealed in the measurements of the magnetic field dependence of nuclear spin polarisation.

When the tunnelling reservoir is coupled with electron spins, significant DNP effects on the proton spins can be observed as energy flows out of the tunnelling reservoir into the lattice. In molecular systems, different methyl groups experiencing different potentials have different tunnelling frequencies ω_i . In terms of tunnelling frequency, a distribution of tunnelling reservoirs exists. Once a particular tunnelling reservoir makes contact with the electron spins, apart from the proton DNP signal deriving from the direct contact, the energy diffusion amongst tunnelling reservoirs can give rise to an additional contribution to the nuclear polarisation, therefore a modification to the DNP spectrum due to tunnel diffusion can be observed.

In this chapter, the phenomenon of the electron spin resonance (ESR) tunnel resonance has been studied by using some new experiments that have been designed to investigate the mechanisms underlying the creation of the DNP signal of the proton spins. Two samples have been studied, namely single crystals of copper doped zinc acetate dihydrate and toluene doped with DPPH radicals. Tunnel diffusion [24] is exhibited by the former sample and is absent in the latter.

6.2 Theoretical

Clough and co-workers have described various mechanisms defining the nuclear polarisation that arises when a tunnelling methyl group is brought into resonance with an electron spin [17, 18]. For a sample containing methyl groups with a mean tunnelling frequency ω_t , there is a tunnelling reservoir which has a Gaussian distribution of frequencies,

$$G(\omega_t^{(i)}) = \frac{1}{b\sqrt{2\pi}} \exp\left(-\frac{1}{2}\left(\frac{\omega_t^{(i)} - \omega_t}{b}\right)^2\right) \quad (6.1)$$

where $\omega_t^{(i)}$ is the tunnelling frequency of the methyl subgroup labelled i . b is the half width at half maximum of the distribution.

Associated with each subgroup i , there is a thermal reservoir characterised by the temperature $\theta_t^{(i)}$. These tunnelling reservoirs are very weakly coupled to the lattice, particularly at low temperature, therefore by cooling the sample the tunnelling temperature $\theta_t^{(i)}$ becomes decoupled from the lattice temperature θ_L , i.e. $\theta_t^{(i)} > \theta_L$.

In ESR tunnel resonance experiments, electron spins will be in resonance with the methyl subgroup i when $\omega_s = \omega_t^{(i)}$, where ω_s is the electron Larmor frequency. However, transitions between A and E methyl tunnelling states involve changes in nuclear spin-symmetry species, therefore only electron-nuclear dipole-dipole interactions that have the correct symmetry properties will induce the A - E conversion. As a result, transitions at frequencies $\omega_s - \omega_t^{(i)} \pm l\omega_n$ ($l=0, 1$) are allowed, arising from the electron-nuclear dipole-dipole interaction operators like S_+I_z , S_+I_+ and S_+I_- , where ω_n is the ^1H Larmor frequency. The operator S_+I_z induces transitions labelled $l=0$, thereby leading to no change in ^1H polarisation. However, transitions labelled $l=1$ are driven by the operators S_+I_+ and S_+I_- , where the energy mismatch between the tunnelling reservoir $\hbar\omega_t^{(i)}$ and electron spins $\hbar\omega_s$ is made up by the ^1H Zeeman energy $\hbar\omega_n$, therefore changes in ^1H polarisation are involved. Because the electron spins are well coupled to the lattice, the tunnelling state transitions in contact with the electron spins lead to a cooling of the tunnelling reservoir. As discussed in Chapter 2, the tunnelling temperature evolution was developed by Clough and Hobson [17],

$$\frac{d(\theta_L^{-1} - \theta_t^{(i)-1})}{dt} = -a_t (\theta_L^{-1} - \theta_t^{(i)-1}) G(\omega_t^{(i)}) \quad (6.2)$$

$$\times \left[W^{(-)} g(\omega_s - \omega_t^{(i)} - \omega_n) + W^{(+)} g(\omega_s - \omega_t^{(i)} + \omega_n) + W^{(0)} g(\omega_s - \omega_t^{(i)}) \right]$$

where a_t is a constant. $g(\omega)$ is the ESR spectrum [68] which is governed by the electron spin Zeeman interaction with the applied field B . $W^{(0,\pm)}$ are transition probabilities per unit time at $\omega_s = \omega_t^{(i)}$ and $\omega_s = \omega_t^{(i)} \mp \omega_n$, respectively. In Eqn. (6.2), the ESR spectrum may be assumed to have the Gaussian form,

$$g(\omega) = \frac{1}{c\sqrt{2\pi}} \exp\left(-\frac{1}{2}\left(\frac{\omega}{c}\right)^2\right) \quad (6.3)$$

where c is the half width at half maximum. On the right-hand side of Eqn. (6.2), the last term $W^{(0)} g(\omega_s - \omega_t^{(i)})$ accounts for the change in the tunnelling temperature when the tunnelling frequency matches the electron Larmor frequency, i.e. $\omega_s = \omega_t^{(i)}$. The first two terms $W^{(-)} g(\omega_s - \omega_t^{(i)} - \omega_n)$ and $W^{(+)} g(\omega_s - \omega_t^{(i)} + \omega_n)$ are responsible for the change in the tunnelling temperature when $\omega_s = \omega_t^{(i)} \pm \omega_n$, where transitions labelled $l=1$ are driven by the electron-nuclear dipole-dipole interactions S_+I_{\pm} .

The rate of change in ^1H polarisation $\langle I_z \rangle$ due to resonant contact with the electron spin may be written as follows (Clough and Hobson [17]),

$$\left[\frac{1}{I_0} \frac{d\langle I_z \rangle}{dt} \right]_{tr} \quad (6.4)$$

$$= -a(\theta_L^{-1} - \theta_t^{(i)-1}) G(\omega_t^{(i)}) \times \left[W^{(-)} g(\omega_s - \omega_t^{(i)} - \omega_n) - W^{(+)} g(\omega_s - \omega_t^{(i)} + \omega_n) \right]$$

where a is a constant. I_0 is the ^1H polarisation at thermal equilibrium at the field B . The terms in square brackets on the right-hand side of Eqn. (6.4) account for the change in ^1H polarisation. When $\omega_s = \omega_t^{(i)} \pm \omega_n$, any energy mismatch between the tunnelling reservoir and the electron spin Zeeman reservoir will be made up by a spin flip in the nuclear Zeeman states (Fig. 6.1). The minus sign between the two terms is due to the opposite directions of the spin flip. Although Eqn. (6.2) predicts a change in the tunnelling temperature $\theta_t^{(i)}$ when $\omega_s = \omega_t^{(i)}$, it is worth noting that there is no change in ^1H polarisation (Eqn. (6.4)), since no nuclear spin flip is involved.

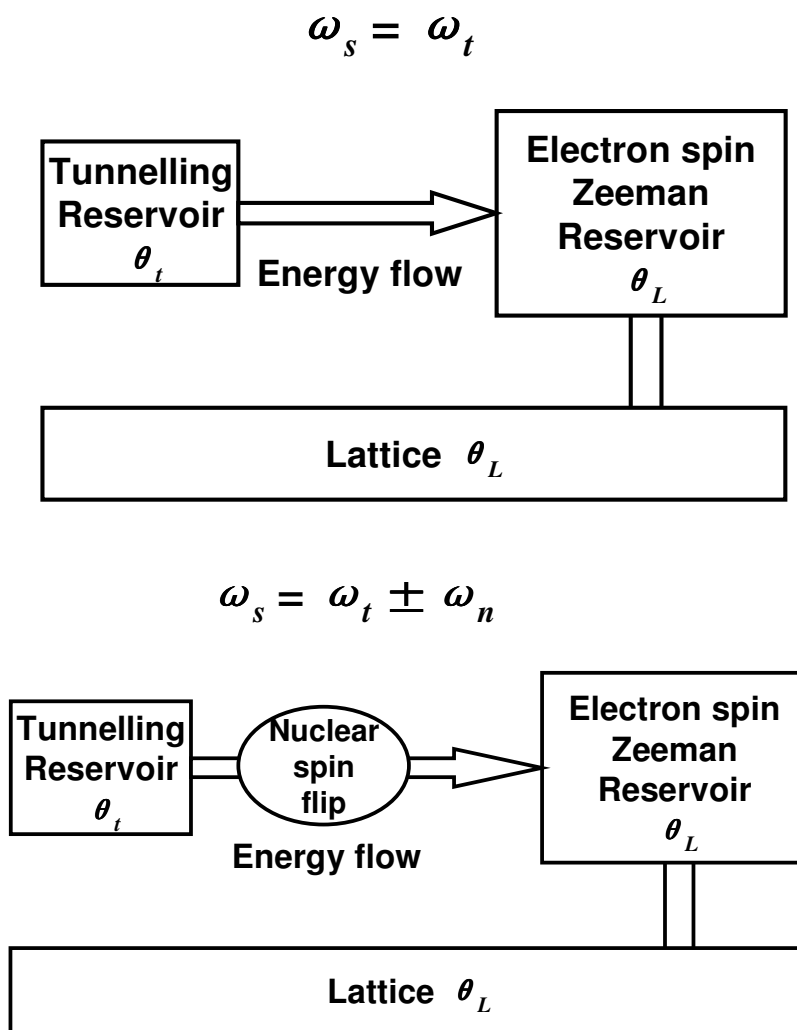


Figure 6.1 Schematic diagrams of the tunnelling state transitions in ESR tunnel resonance in terms of thermal reservoirs

Another mechanism that can contribute to the rate equation for $\langle I_z \rangle$ is the spin-lattice relaxation, which will slowly drive the ^1H polarisation towards thermal equilibrium,

$$\left[\frac{d\langle I_z \rangle}{dt} \right]_{rel} = - \frac{(\langle I_z \rangle - I_0)}{T_1} \quad (6.5)$$

where T_1 is spin-lattice relaxation time.

Additionally, there is another mechanism known as tunnel diffusion [24], which promotes equilibration towards a common temperature amongst the tunnelling subgroups. Considering two methyl subgroups, if they have the same tunnelling frequency, spatial diffusion can occur where conversion of one methyl group between the A and E species is accompanied by a second methyl group making the reverse transition. However, if they have a mismatch in energy which is equal to the ^1H Zeeman splitting at that field, the spectral diffusion of tunnelling energy can also occur where the difference in tunnelling energy is made up by a flip of the ^1H spin; in this case it is the nuclear dipole-dipole interaction that mediates the energy exchange. Therefore spectral tunnel diffusion can cause a change in the ^1H polarisation.

If the difference in frequency between two methyl subgroups matches the ^1H Larmor frequency (i.e. $\omega_t^{(i)} - \omega_t^{(i\pm)} = \pm \omega_n$), the spectral tunnel diffusion between these two drives them towards mutual equilibrium. This energy exchange mechanism will spread out among all subgroups and equilibrate towards a common temperature amongst the tunnelling subgroups (Fig. 6.2). Clough describes the process in terms of a tunnelling distribution temperature [17, 18, 24, 25, 69]. We shall model the same phenomenon in a form suitable for numerical simulation. Given the respective heat capacities are proportional to the tunnelling distribution $G(\omega_t)$, the rate of change in tunnelling temperatures of subgroups i and i^\pm will be governed by,

$$\begin{aligned} \frac{d\theta_t^{(i)}}{dt} &= -k_d \frac{G(\omega_t^{(i)})}{G(\omega_t^{(i)}) + G(\omega_t^{(i\pm)})} (\theta_t^{(i)} - \theta_t^{(i\pm)}) \delta(\omega_t^{(i)} - \omega_t^{(i\pm)} \pm \omega_n) \\ \frac{d\theta_t^{(i\pm)}}{dt} &= -k_d \frac{G(\omega_t^{(i\pm)})}{G(\omega_t^{(i)}) + G(\omega_t^{(i\pm)})} (\theta_t^{(i\pm)} - \theta_t^{(i)}) \delta(\omega_t^{(i)} - \omega_t^{(i\pm)} \pm \omega_n) \end{aligned} \quad (6.6)$$

where $\delta(\omega)$ is the Kroneker delta function and k_d is a constant. The tunnel diffusion process between the tunnelling reservoirs associated with these two subgroups is also accompanied by the change in ^1H polarisation, and it may be written as,

$$\left[\frac{1}{I_0} \frac{d\langle I_z \rangle}{dt} \right]_{id}^{(i,i\pm)} = k_0 (\theta_t^{(i)} - \theta_t^{(i\pm)}) \frac{G(\omega_t^{(i)})G(\omega_t^{(i\pm)})}{G(\omega_t^{(i)}) + G(\omega_t^{(i\pm)})} \delta(\omega_t^{(i)} - \omega_t^{(i\pm)} \pm \omega_n) \quad (6.7)$$

where k_0 is a constant. Eqn. (6.7) accounts for the change in ^1H polarisation arising from tunnel diffusion amongst a pair of tunnelling subgroups. The net change in ^1H polarisation $\langle I_z \rangle$ for the system will be a sum over all subgroups.

Tunnelling reservoirs

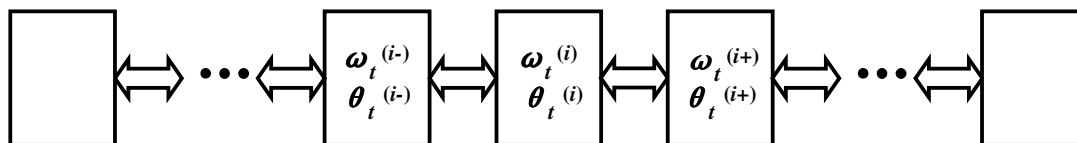


Figure 6.2 Schematic diagram of spectral tunnel diffusion amongst methyl tunnelling subgroups;

$$\omega_t^{(i)} - \omega_t^{(i\pm)} = \pm \omega_n$$

The evolution of the tunnelling temperature $\theta_t^{(i)}$ is governed by Eqn. (6.2) and (6.6). Once a particular methyl subgroup i is in resonant contact with the electron spins, i.e. $\omega_t^{(i)} = \omega_s$, the associated temperature $\theta_t^{(i)}$ will then be driven towards the lattice temperature θ_L . Simultaneously the change in the temperature $\theta_t^{(i)}$ will spread out within all subgroups via diffusion of the tunnelling energy. These two processes occur simultaneously so that the tunnelling temperature is the overall result of Eqn. (6.2) and (6.6).

The change in ^1H polarisation $\langle I_z \rangle$ is governed by Eqn. (6.4), (6.5) and (6.7). It is the overall result of three mechanisms; (a) contact with the electron spin, (b) spectral diffusion of the tunnelling energy and (c) spin-lattice relaxation.

6.3 Experimental

6.3.1 Copper doped zinc acetate dihydrate

In the experiments, single crystals of zinc acetate dihydrate doped with small quantities of copper ions have been studied. For tunnel resonance experiments, the unpaired electron spin was provided by the copper ions. The ESR spectrum of this sample is known from the literature [68]. The crystals were grown by slow evaporation over several weeks of an aqueous solution of zinc acetate and copper acetate. Three samples were studied with different copper ion concentrations, and they were prepared from aqueous solutions with Cu:Zn mole ratios of (a) 1:18.2 (5.2mol%), (b) 1:54.5 (1.80mol%) and (c) 1:128 (0.78mol%). For simplicity, they are labelled I, II and III, respectively. For all samples the crystal axes were determined from the crystal morphology. The c -axis of the single crystal was aligned parallel to the applied magnetic field so that the major principle axis of the g -tensor, g_{\parallel} was obtained. All experiments were conducted at $T = 4.2\text{K}$.

A variety of experiments were conducted to investigate the tunnelling properties of the samples; (a) tunnel resonance level-crossing experiment, (b) cooling of the tunnelling reservoir, (c) tunnel diffusion and (d) time evolution at the tunnel resonance. The pulse sequence of the tunnel resonance experiment (experiment (a)) was presented in Chapter 3 (Fig. 3.17). Time evolution at the tunnel resonance (experiment (d)) was conducted using the saturation-recovery pulse sequence illustrated in Chapter 3 (Fig. 3.13), with the recovery field B_r at tunnel resonance.

The pulse sequence of experiment (b), cooling of the tunnelling reservoir, is illustrated in Fig. 6.3, and the details are as follows,

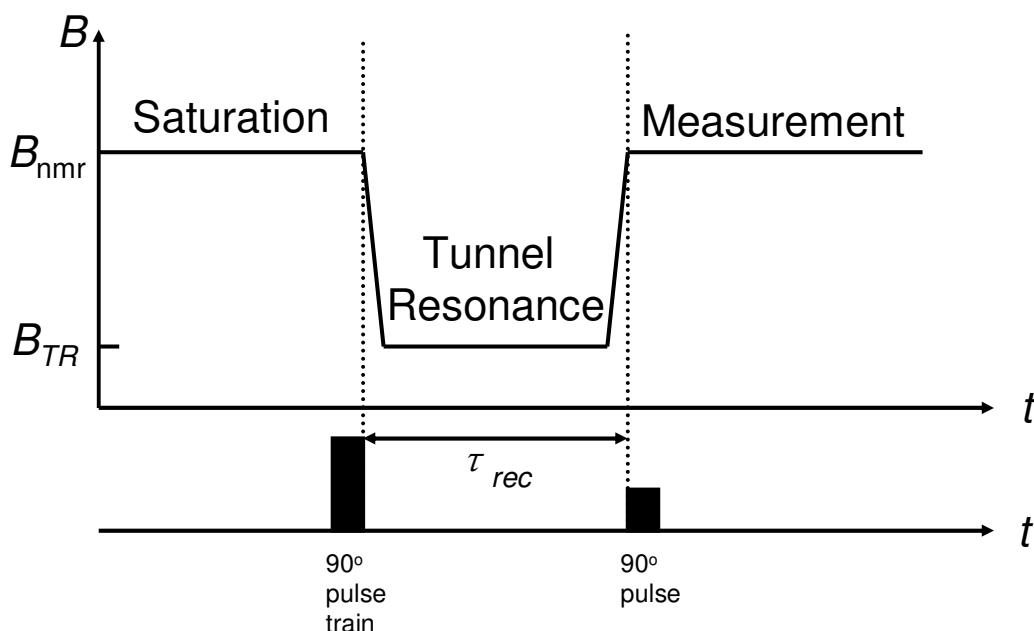


Figure 6.3 Field-cycling NMR pulse sequence of the tunnelling reservoir cooling experiment

- (1) Saturation of the ^1H magnetisation with a train of 90° rf pulses at the resonant field B_{nmr} .
- (2) Rapid switch to the tunnel-resonance field B_{TR} , where $\omega_s = \omega_t \pm \omega_n$.
- (3) Evolution of the ^1H magnetisation at the field B_{TR} for a fixed period of time $\tau_{\text{rec}} = 300\text{s}$.
- (4) Rapid switch back to the resonant field B_{nmr} .
- (5) Measurement of the ^1H polarisation $\langle I_z \rangle$ with a resonant 90° rf pulse.

By repeating the procedure (1)-(5), the evolution of the cooling of the tunnelling reservoir was obtained.

The pulse sequence of experiment (c), tunnel diffusion, is presented in Fig. 6.4, and the details are,

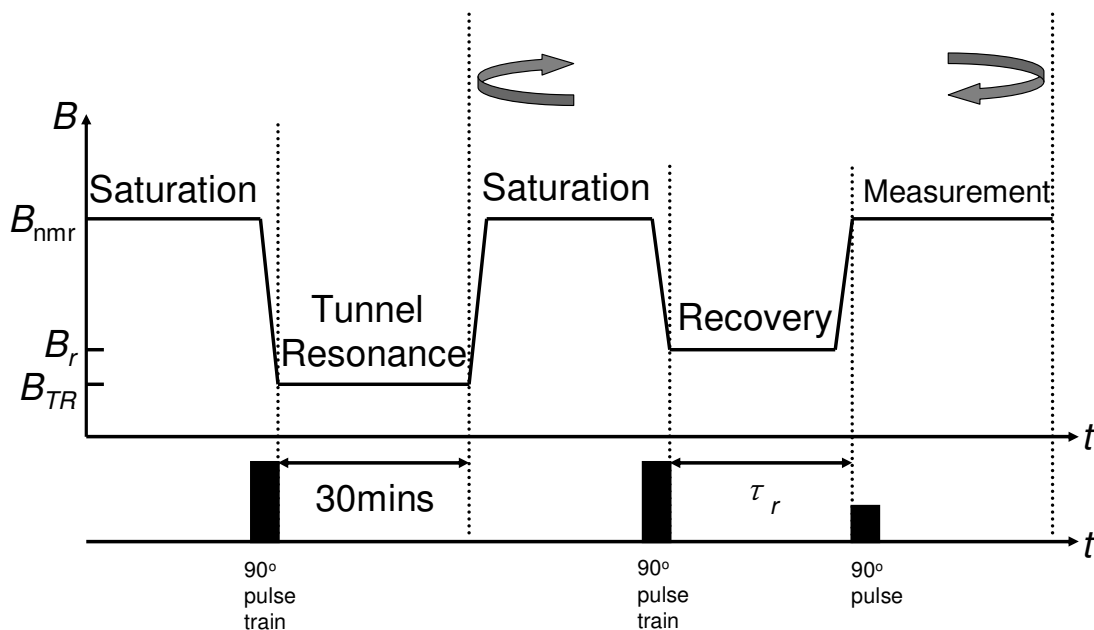


Figure 6.4 Field-cycling NMR pulse sequence of the tunnel diffusion experiment

- (1) Saturation of the ^1H magnetisation with a train of 90° rf pulses at B_{nmr} .
- (2) Rapid switch to the tunnel-resonance field B_{TR} , where $\omega_s = \omega_l \pm \omega_n$.
- (3) Evolution of the ^1H magnetisation at B_{TR} for $\tau_{\text{rec}} = 30\text{mins}$.
- (4) Rapid switch to B_{nmr} .
- (5) Saturation of ^1H magnetisation with a train of 90° pulses at B_{nmr} .
- (6) Rapid switch to the recovery field B_r , which is non-resonant, i.e. $B_r \neq B_{\text{TR}}$.
- (7) Evolution of the ^1H magnetisation at B_r for a fixed period of time $\tau_r = 10\text{s}$.
- (8) Rapid switch back to B_{nmr} .
- (9) Measurement of the ^1H polarisation $\langle I_z \rangle$ with a resonant 90° rf pulse.

The results of the tunnel diffusion experiment were obtained by repeating the procedure (5)-(9) to acquire the ^1H polarisation evolution at non-resonant field B_r .

It is worth noting that the experimental data of the ^1H polarisation $\langle I_z \rangle$ were in arbitrary units. All experimental data have been calibrated by scaling to the magnetisation at thermal equilibrium I_0 at the field $B = 0.036\text{T}$, which characterises the centre of the ESR spectrum. As a result all data are presented in terms of $\langle I_z \rangle / I_0$.

6.3.2 Toluene doped with DPPH radicals

In the experiments, DPPH (2,2-Diphenyl-1-picrylhydrazyl) was dissolved in toluene to introduce free radicals with which the methyl tunnelling groups in toluene may contact. The mole ratio of DPPH radical to toluene was estimated as 4mol%. It is known that there are two

crystalline phases of toluene, the stable one α melts at $T = 178\text{K}$ and the unstable one β melts at $T = 154\text{K}$ [70]. In this work, a particular heat treatment was used to obtain the α -crystalline phase of toluene,

- (1) The sample was cooled down to the boiling point of liquid nitrogen ($\sim 77\text{K}$).
- (2) The sample was steadily warmed up to the temperature $T = 160\text{K}$, which was slightly lower than the melting point of toluene.
- (3) The sample was annealed at $T = 160\text{K}$ for a period of time, typically, 30 minutes.
- (4) The sample was cooled down to the low temperature $T = 4.2\text{K}$.

Tunnel resonance experiments were conducted on toluene doped with DPPH radicals, by using the level-crossing pulse sequence (Fig. 3.17) with a variety of relaxation times.

6.3.3 Numerical simulations

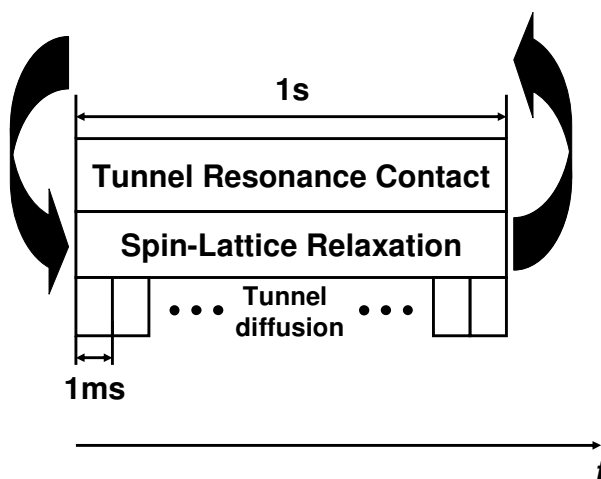


Figure 6.5 Schematic diagram of the numerical simulation of the ESR tunnel resonance phenomena

As discussed in section 6.2, the ^1H spin polarisation is governed by three mechanisms; (a) tunnelling contact with the electron spin (Eqn. (6.2) and (6.4)), (b) tunnel diffusion (Eqn. (6.6) and (6.7)) and (c) spin-lattice relaxation (Eqn. (6.5)). Numerical simulations can be achieved by combining these mechanisms. First of all, 101 methyl tunnelling subgroups were established with the Gaussian distribution (Eqn. (6.1)), and the difference in frequency between two adjacent subgroups was set to be the same as the nuclear spin Larmor frequency, i.e. $\omega_i^{(i)} - \omega_i^{(i\pm)} = \pm \omega_n$ ($i = 1, 2, \dots, 101$). The initial tunnelling temperature was assumed to be $\theta_i = 40\text{K}$, and the temperature of the electron spin Zeeman reservoir was always the same as the lattice temperature $\theta_L = 4\text{K}$ since the electron spin-lattice relaxation is known to be fast. At a magnetic field B , evolutions of both tunnelling temperature $\theta_i^{(i)}$ and ^1H polarisation $\langle I_z \rangle$

due to the tunnelling contact with the electron spin and the spin-lattice relaxation were calculated with time increments of 1s, by using Eqn. (6.2), (6.4) and (6.5). Simultaneously both $\theta_r^{(i)}$ and $\langle I_z \rangle$ due to tunnel diffusion were calculated with increments of 1ms, by using Eqn. (6.6) and (6.7), since tunnel diffusion is a much faster process (Fig. 6.5). The evolution of tunnelling temperatures $\theta_r^{(i)}$ and the change in ^1H polarisation $\langle I_z \rangle$ has been obtained from the results of simulations of these mechanisms simultaneously.

6.4 Results and discussion

6.4.1 Copper doped zinc acetate dihydrate

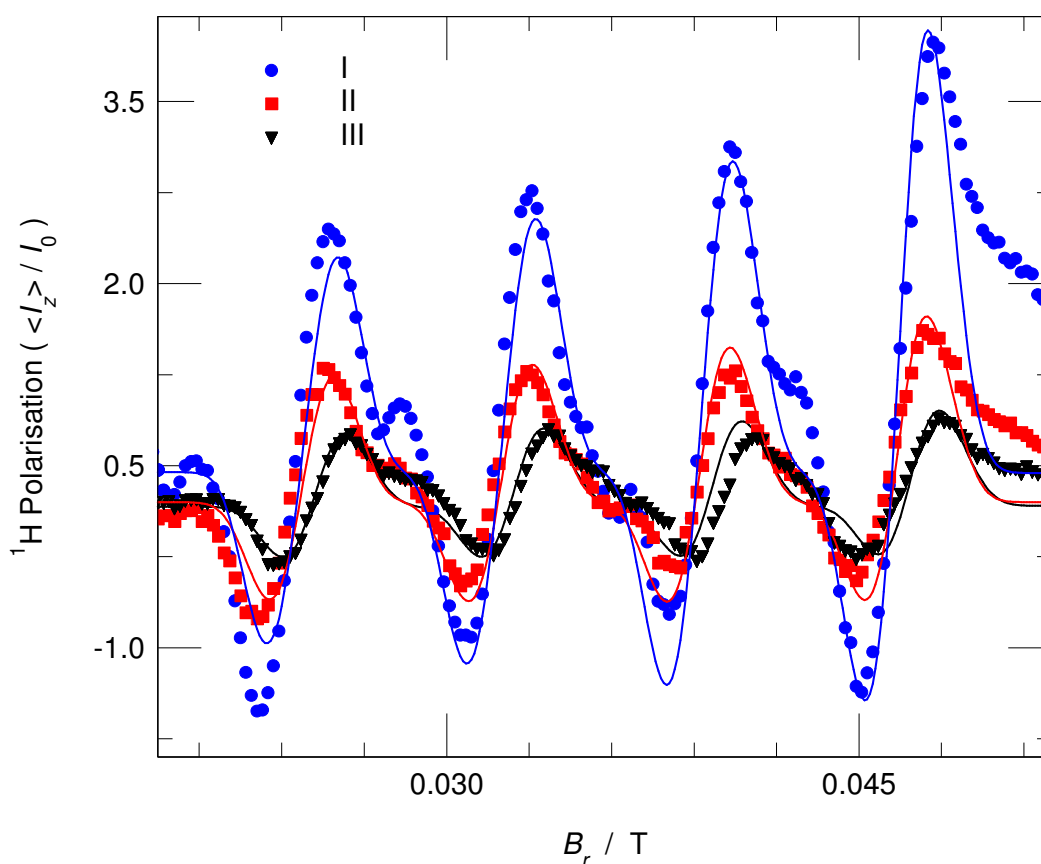


Figure 6.6 Tunnel resonance spectra of copper doped zinc acetate dihydrate; the data were recorded at $T = 4.2\text{K}$; solid lines represent simulation results

Tunnel resonance experiments were conducted at $T = 4.2\text{K}$, by using the level-crossing pulse sequence (Fig. 3.17), and plots of the ^1H spin polarisation as a function of relaxation field B_r are presented in Fig. 6.6. The data were recorded on three samples I, II and III. The spectra were all recorded in the direction of decreasing field. The time spent at the relaxation field B_r was $\tau_{\text{rec}} = 60\text{s}$. Substantial enhancements of the ^1H polarisation are observed, especially in

sample I (blue circles). Each spectrum comprises four lines and each line appears as the derivative of an absorption line.

Around the regions where $B_r = 0.028\text{T}$ and 0.043T , some anomalous broadenings or even small peaks in the background are also observed. This arises from the resonant contact with impurity electrons. In this case, paramagnetic manganese ions are the main impurities. Because they do not affect the resonant contact between the methyl tunnelling reservoir and copper electron spins of the interest, these anomalies in the spectra due to the manganese impurities will be ignored.

It is known that the four-fold hyperfine interaction between the unpaired copper electron and the spin $I_{\text{Cu}} = 3/2$ of the copper nuclei gives rise to a four-fold ESR spectrum [68]. It is evident that the tunnel resonance spectrum traces the envelope of the ESR spectrum of copper ions and hence the four-line spectrum is observed. For each line, it is clear that on the high-field side, the ^1H polarisation is enhanced so that the ^1H Zeeman reservoir is cooled. However on the low-field side, the ^1H polarisation is reduced, and this reveals the ^1H Zeeman reservoir is heated. This lineshape is characteristic of DNP.

The centre of the four-line spectrum represents the magnetic field at which the methyl tunnelling frequency ω_t matches the electron spin Larmor frequency ω_s ,

$$\omega_t = g_{\text{obs}} \beta B_{\text{TR}} / \hbar \quad (6.8)$$

where $\beta = 9.274 \times 10^{-24} \text{J/T}$ is the Bohr magneton. The methyl tunnelling frequency $\omega_t = 7.52 \times 10^9 \text{s}^{-1}$ is known from inelastic neutron scattering [71], and with the magnetic field measured at the centre of the four-line spectrum $B_{\text{TR}} = 0.036 \pm 0.0005\text{T}$, the g -value is obtained to be $g_{\text{obs}} = 2.38 \pm 0.03$. Given the known g -tensor ($g_{//} = 2.47$) [68], this is consistent with the orientation of the crystal in the magnetic field.

It is clear that with increasing the copper ion concentration, the enhancement of the ^1H polarisation is increased. This is because more resonant contacts can be made between electron spins and methyl groups and hence the tunnelling reservoirs, thereby inducing a stronger ^1H polarisation via tunnel resonance.

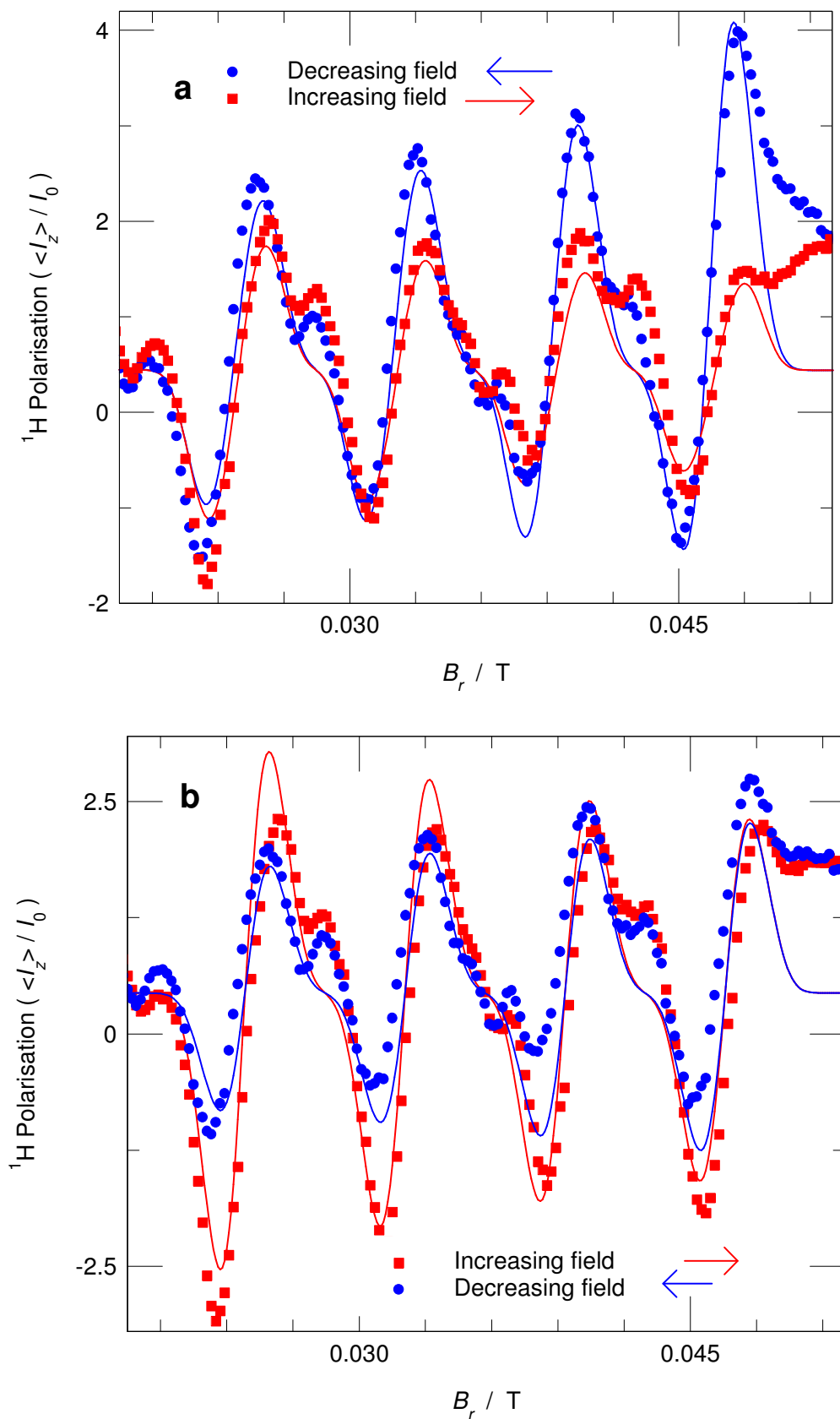


Figure 6.7 Tunnel resonance spectra of copper doped zinc acetate dihydrate (1:18.2) with field scan directions of (a) high-to-low-to-high and (b) low-to-high-to-low ($T = 4.2\text{K}$); solid lines represent simulation results

In Fig. 6.6, considering the width of the DNP lineshape, the difference in field between the positive and negative peaks is measured to be approximately 2.5mT, which is equivalent to 83MHz in frequency units. This is significantly larger than twice the ^1H Larmor frequency, $2\nu_n = 3.2\text{MHz}$, at the field $B_{\text{TR}} = 0.036\text{T}$ that characterises the centre of the tunnel resonance spectrum. It is also significantly broader than the inherent ESR linewidth of 25MHz (0.75mT) [68]. Therefore this broad DNP lineshape reveals that there is a distribution of tunnelling frequencies in the sample. Consequently, the diffusion of tunnelling energy associated with these tunnelling frequencies can provide an additional mechanism for the creation of dynamic nuclear polarisation. It is also clear that for each line in the spectrum, the amplitude of positive peak is greater than that of negative one. This asymmetric feature reveals the manifestation of tunnel diffusion, since the latter can give rise to a history-dependent lineshape.

Tunnel resonance experiments were conducted in two different ways on sample I. The spectra in Fig. 6.7 were recorded in the field direction of (a) high-to-low-to-high and (b) low-to-high-to-low. It is evident in both figures that following the field direction in which the spectra were recorded, the enhancement of the ^1H polarisation is decreased, i.e. in Fig. 6.7a, the DNP effect is decreased from higher to lower field, then back up to higher field, while it is also decreased in Fig. 6.7b in the opposite directions. As discussed above, once tunnel resonance conditions are matched, the resonant contact between tunnelling reservoirs and electrons spins is then established, the electron-proton dipolar interactions become available to mediate the transfer of energy from hot tunnelling reservoirs to the cold lattice. However unlike the lattice, heat capacities of tunnelling reservoirs are not infinite. Therefore the tunnelling temperature will be decreased as the energy preserved in tunnelling reservoirs continuously flows out. Because proton spin flips are involved in this process, the rate of the ^1H spin flips will be reduced. As a result the enhancement of the ^1H polarisation will be decreased. The observation of the history dependence of the ^1H polarisation is a manifestation of the cooling of tunnelling reservoirs that possess finite heat capacities.

To investigate further, on sample II, tunnel resonance spectra were recorded in both field directions, and summation and subtraction of the two spectra are presented in Fig. 6.8. In the summation spectrum (black squares) for each line, the positive and negative peaks have similar amplitudes. This symmetric feature traces out the DNP lineshape, which arises from tunnel resonant contact with the electron spin, since the summation of the spectra recorded in opposite field directions cancels out the asymmetry that is characteristic of the tunnel diffusion process. However the subtraction spectrum (green circles) is observed to be a Gaussian-like pattern, and this indicates tunnel diffusion amongst tunnelling reservoirs. The

shape of the peaks in the subtraction spectrum is reflective of the Gaussian distribution of tunnelling frequencies in the tunnelling reservoir.

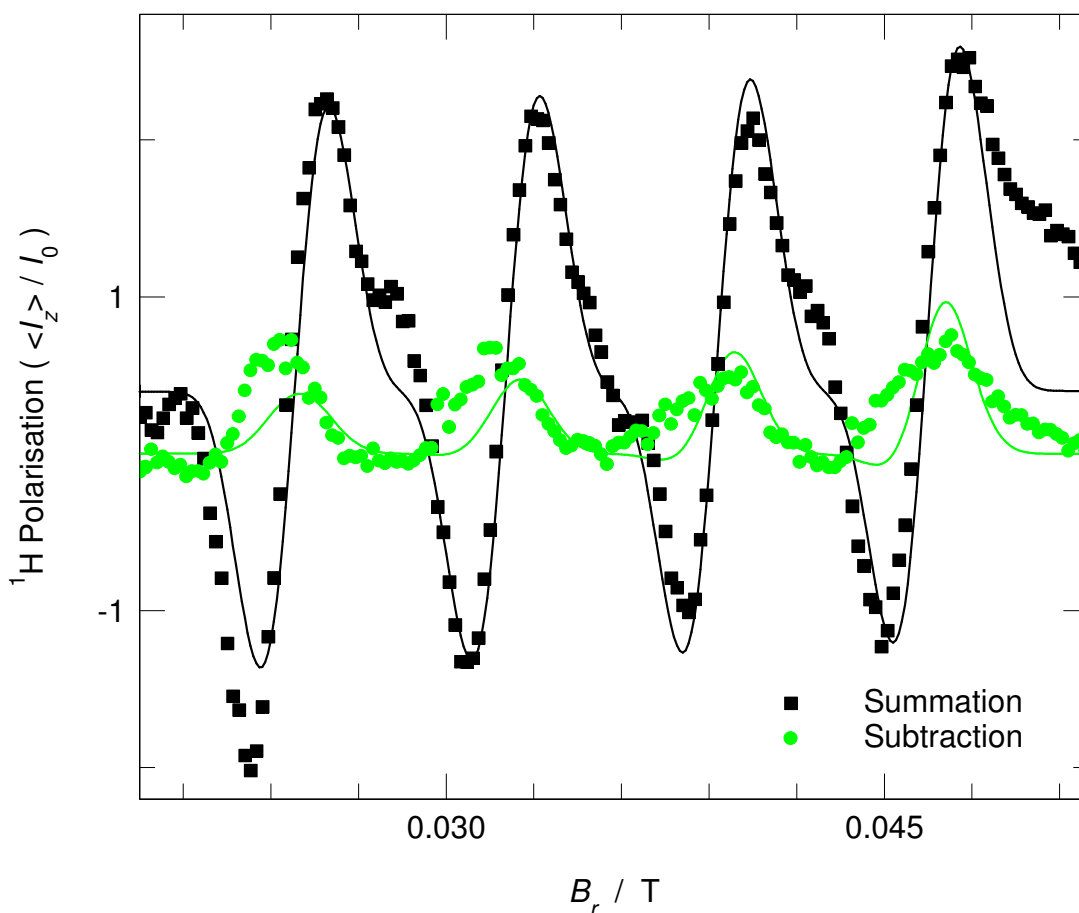


Figure 6.8 Results from summation and subtraction of the tunnel resonance spectra of copper doped zinc acetate dihydrate (1:54.5) recorded in both field directions ($T = 4.2\text{K}$); solid lines represent simulation results

Numerical simulations of the tunnel resonance experiments were made. Firstly a distribution consisting of a range of tunnelling frequencies, centred at $\nu_t = 1.2\text{GHz}$, which is the tunnelling frequency of this sample as measured by neutron scattering [71], was established. 101 methyl subgroups (and hence tunnelling frequencies) was determined to be a sufficient number for the purpose of simulation. For each subgroup, the change in tunnelling temperature $\theta_t^{(i)}$ due to its tunnel resonant contact with the electron spin was calculated every second, by using Eqn. (6.2). Simultaneously, during this 1 second interval, the redistribution in tunnelling temperature $\theta_t^{(i)}$ within these 101 subgroups was calculated every 1 millisecond, by using Eqn. (6.6). After the calculation of one loop of 1 second, a new set of tunnelling temperatures $\theta_t^{(i)}$ ($i = 1, 2, \dots, 101$) was obtained. For each field B_r , the tunnelling temperatures $\theta_t^{(i)}$ were calculated for $\tau_{\text{rec}} = 60\text{s}$, which was set to be the same as that in the experiment. By following

the field change in the experiment, i.e. the field was decreased then increased, the evolution of tunnelling temperatures $\theta_t^{(i)}$ was simulated. Similarly, by using Eqn. (6.4) and (6.7), which predict the rate of change in ^1H polarisation $\langle I_z \rangle$, together with the calculated tunnelling temperatures $\theta_t^{(i)}$, the ^1H polarisation $\langle I_z \rangle$ was simulated for each field B_r using the same simulation procedure. It should be noted that the spin-lattice relaxation was not considered in this simulation, and it was negligible since the spin-lattice relaxation time T_1 ($>600\text{s}$) is much slower than the recovery time at each field (i.e. $\tau_{\text{rec}} = 60\text{s}$). The simulation results for the tunnel resonance spectra are illustrated by solid lines in all relevant figures (Fig. 6.6–6.8), and good agreement with the experimental data is obtained. The best fit parameters are presented in Table 6.2. The evolution of tunnelling temperatures $\theta_t^{(i)}$ in the tunnel resonance experiment (Fig. 6.7a) was simulated and is presented in Fig. 6.9 and Fig. 6.10 in 3D as a function of time t and tunnelling frequency ν .

The initial tunnelling temperature was assumed to be $\theta_t(t=0) = 40\text{K}$, which is the typical value for a freshly cooled system. In the $\theta_t - \nu$ plot (Fig. 6.9b), the distribution of frequencies for tunnelling reservoirs are presented. The $t - \nu$ plot (Fig. 6.10a) illustrates the spectral diffusion amongst the tunnelling reservoirs with time. In the $\theta_t - t$ plot (Fig. 6.10b), the cooling of the tunnelling reservoirs is demonstrated.

In the $\theta_t - t$ plot (Fig. 6.10b), it is clear that the upper boundary is relatively smooth. This describes the evolution of the tunnelling temperature $\theta_t^{(\text{non-res})}$ of the non-resonant methyl groups (e.g. $\nu = 1.13\text{GHz}$ and 1.27GHz). In this case the cooling of the tunnelling temperature $\theta_t^{(\text{non-res})}$ is mainly due to tunnel diffusion. However, the lower boundary is from the methyl groups that experience a large change in tunnelling temperature. It also has a cooling trend, but steps appear corresponding to the four lines in the copper hyperfine spectrum (Fig. 6.7a); eight in all, since the simulation follows field scan in both down and up directions through tunnel resonance. When the field is tuned so that resonant contact is made between the tunnelling reservoir and the electron spin, the tunnelling temperature θ_t is rapidly decreased, followed by a flat region when the field is tuned out and the contact is off; the slight increase of θ_t in this flat region is due to the heat exchange between the tunnelling reservoir of the interest and other hotter tunnelling reservoirs via tunnel diffusion.

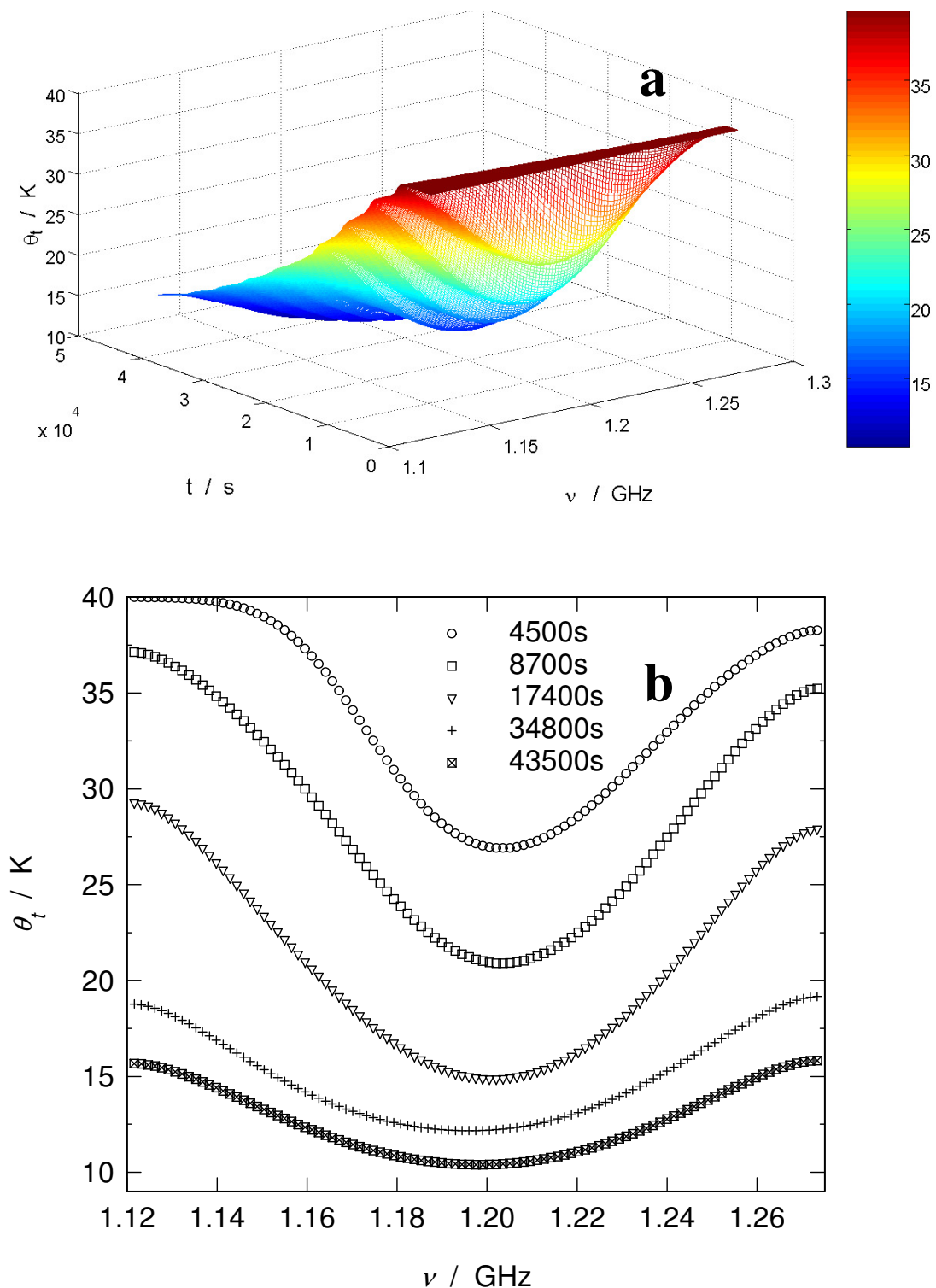


Figure 6.9 (a) Evolution of tunnelling temperatures θ_t as a function of time t and tunnelling frequency ν from simulation of the tunnel resonance spectra in Fig. 6.7a; (b) plot of tunnelling temperature vs. tunnelling frequency

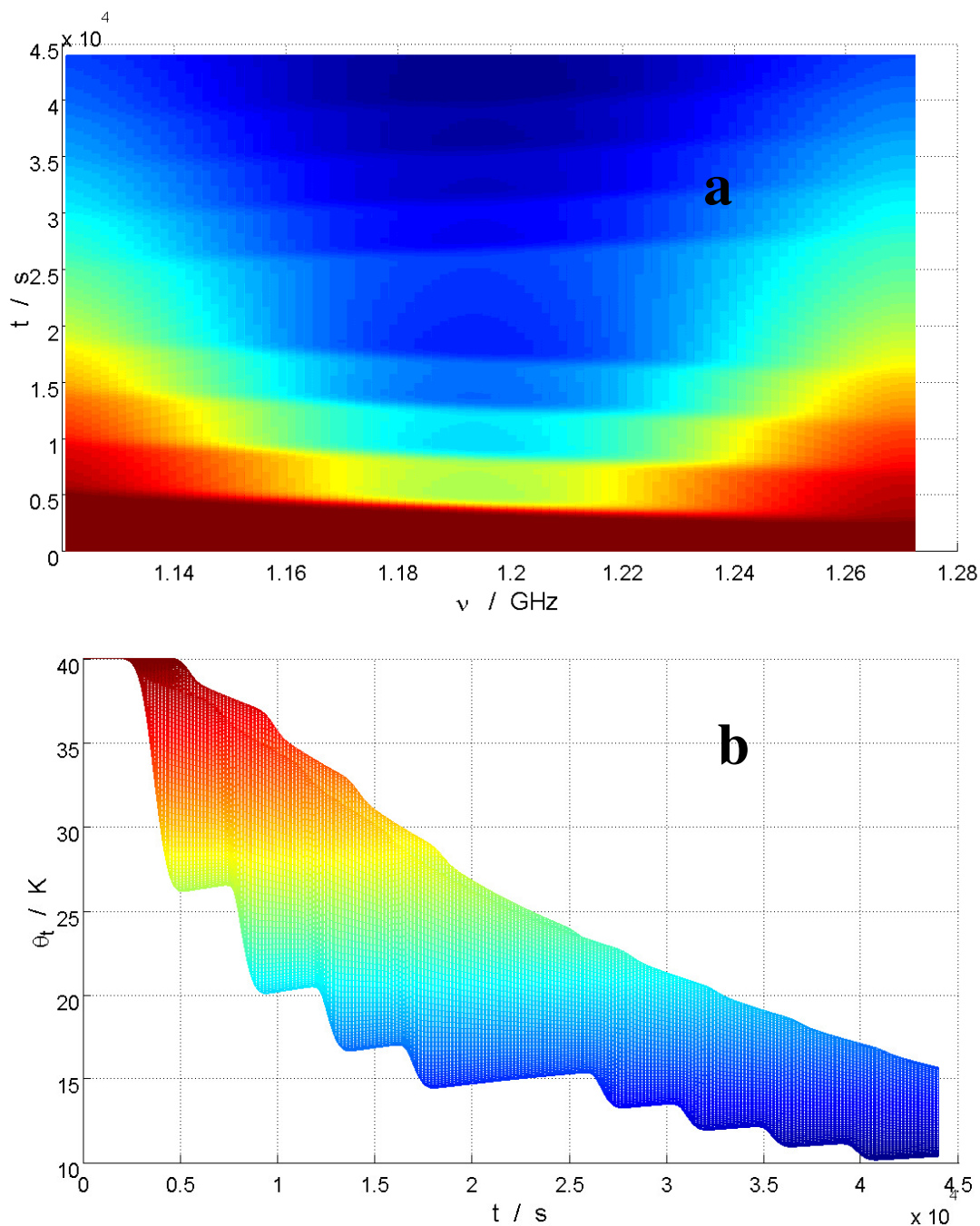


Figure 6.10 (a) plot of time t vs. tunnelling frequency ν and (b) plot of tunnelling temperature θ_t vs. time t from simulation of the tunnel resonance spectra in Fig. 6.7a

As discussed above, the heat capacity of the tunnelling reservoir is finite. Therefore, by making repeated contact with the electron spin, the tunnelling reservoir will systematically lose energy and is cooled down. To study the cooling of the tunnelling reservoir, a series of experiments were conducted using the pulse sequence shown in Fig. 6.3. On the freshly cooled sample, the ^1H polarisation generated during the fixed period of time $\tau_{\text{rec}} = 300$ s at the relaxation field B_{TR} were recorded. The data were recorded on samples I, II and III. In two

sets of experiments, B_{TR} was set to coincide with either positive or negative lobe of the derivative-shape DNP line in Fig. 6.6, i.e. $B_{TR} = 0.048T$ and $0.045T$. In each experiment, the contact time with the electron spin was more than 30 hours. The results are presented in Fig. 6.11.

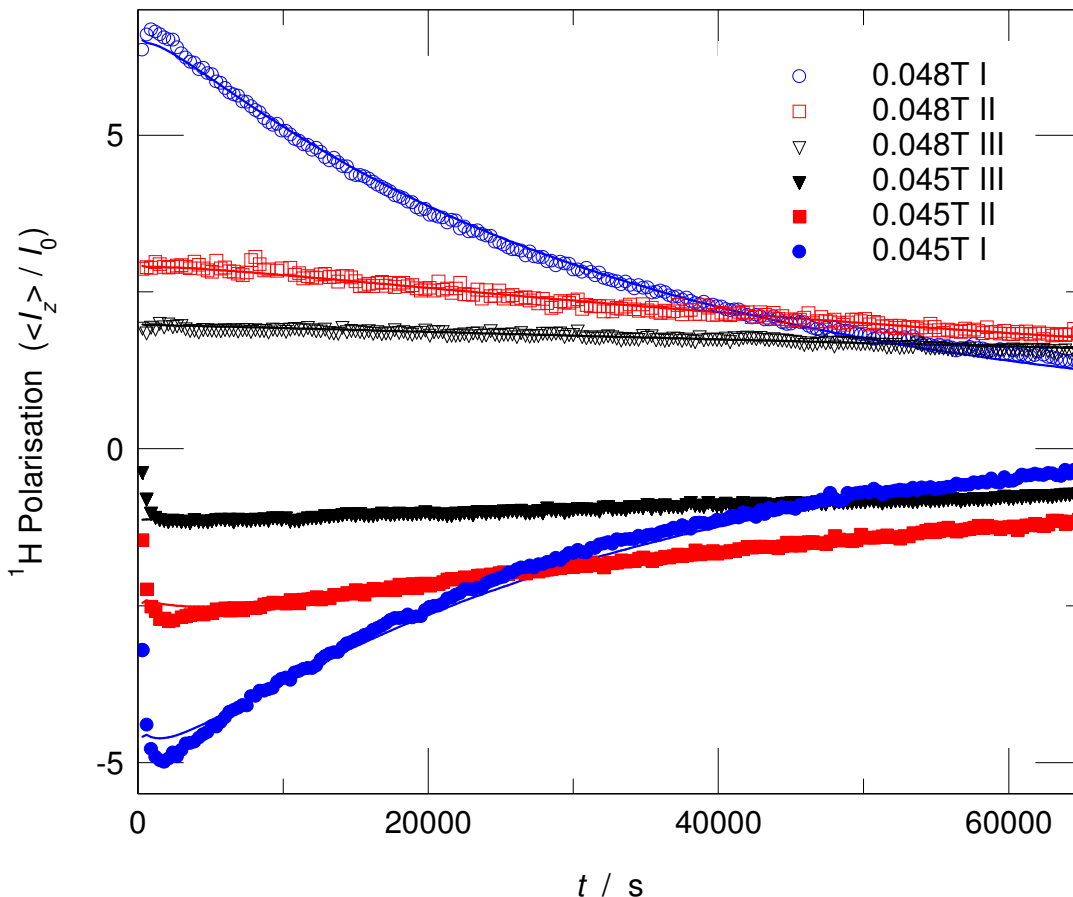


Figure 6.11 Cooling of the tunnelling reservoir in copper doped zinc acetate dehydrate ($T = 4.2K$); solid lines represent simulation results

In both cases it is evident that the 1H polarisation generated at tunnel resonance is reduced systematically with time, since the energy preserved in the tunnelling reservoir flows out and hence the tunnelling reservoir is cooled down. The 1H polarisation will recover towards thermal equilibrium in the limit of long time. In the case of negative lobe of the DNP derivative (i.e. $B_{TR} = 0.045T$, filled points), the 1H polarisation approaches thermal equilibrium from the direction of negative polarisations. Conversely, in the case of positive lobe (i.e. $B_{TR} = 0.048T$, open points), the 1H polarisation is always positive. In both cases, an exponential decay is observed,

$$\langle I_z \rangle = A \exp(-t/T_{tunn}) + I_0 \quad (6.9)$$

where T_{tunn} is the time constant characterizing the cooling rate of the tunnelling reservoir at tunnel resonance, and A is a constant. By fitting the experimental data to Eqn. (6.8), the best fit values of T_{tunn} are shown in Table 6.1.

	Sample I	Sample II	Sample III
$T_{\text{tunn}}(0.048\text{T}) / \text{s}$	$(0.32 \pm 0.01) \times 10^5$	$(1.00 \pm 0.03) \times 10^5$	$(1.90 \pm 0.06) \times 10^5$
$T_{\text{tunn}}(0.045\text{T}) / \text{s}$	$(0.33 \pm 0.01) \times 10^5$	$(0.90 \pm 0.03) \times 10^5$	$(2.10 \pm 0.06) \times 10^5$

Table 6.1 Best fit values of the cooling rate of the tunnelling reservoir in copper doped zinc acetate single crystals

It is clear for each sample that the time constants are similar for both cases. This reveals that the cooling is characteristic of the tunnelling reservoir. With increasing the copper ion concentration, it is evident that the cooling rate is increased. This is because more resonant contacts with electron spins enable the energy preserved in the tunnelling reservoir to flow out more quickly and hence cause a faster cooling rate.

It is worth noting that the cooling is dominated by the contact with the electron spin. When the magnetic field is non-resonant, the tunnelling reservoir is strongly decoupled from the lattice and any relaxation time constants are likely to be in excess of many weeks. For practical reasons this non-resonant tunnelling relaxation rate has not yet been measured.

The tunnelling energy spectrally diffuses amongst the methyl groups. When there is a mismatch between the frequencies of two methyl groups, they can exchange a quantum of tunnelling energy accompanying a change in the nuclear spin states, where any energy mismatch will be made up by a quantum of ^1H Zeeman energy. On the positive lobe of the DNP lineshape, there will be a net cooling of the nuclear spin Zeeman reservoir, thereby leading to an enhancement of the ^1H polarisation. While on the negative lobe, a net warming of the nuclear spin Zeeman reservoir will cause an inversion of the ^1H polarisation. This tunnel diffusion process will make a significant contribution to the observed tunnel resonance lineshapes and manifests itself in the subtraction spectrum (Fig. 6.8).

In this work, the tunnel diffusion rate was measured using the tunnel diffusion pulse sequence (Fig. 6.4). The magnetic field was initially set to coincide with the tunnel resonant field for a fixed period of time $\tau = 1800\text{s}$. During this preparation period, the energy flowed out of the tunnelling reservoir due to contact with the electron spin. Following the preparation stage, the recovered ^1H polarisation was repeatedly recorded every 10s at the non-resonant field $B_r = 0.089\text{T}$ and the results are presented in Fig. 6.12.

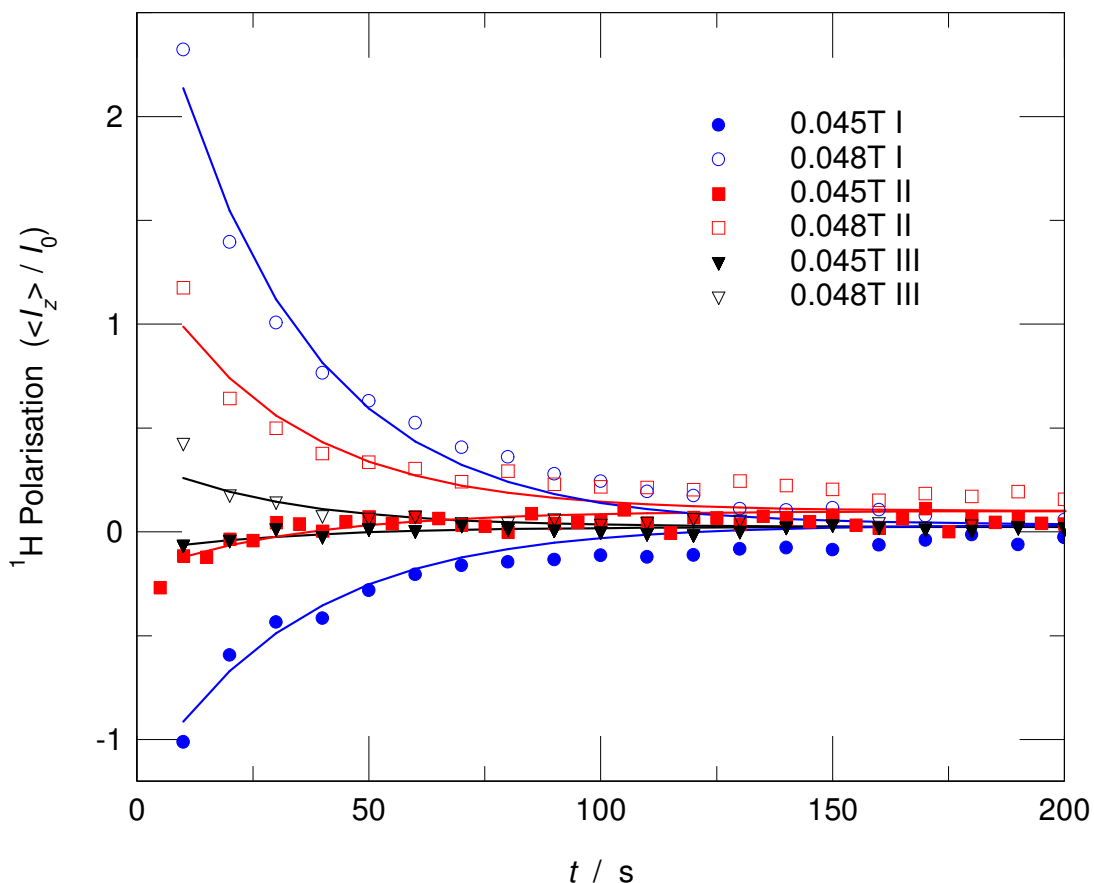


Figure 6.12 Results of the tunnel diffusion experiments conducted on copper doped zinc acetate dihydrate ($T = 4.2\text{K}$); solid line represent simulation results

The experiments were conducted on samples I, II and III, and for each sample, the data were recorded after being prepared at either fields of $B_{TR} = 0.048\text{T}$ or 0.045T , which coincided with either positive or negative lobe of the DNP lineshape. The recovery field B_r was offset from the tunnel resonance. However, it is evident that in the case of positive lobe preparation, the initial ^1H polarisation is significantly larger than that that would have recovered due to spin-lattice relaxation alone (open points), while the initial ^1H polarisation is much smaller than thermal equilibrium, or even negative (filled points) in the case of negative lobe preparation. In each case with increasing time, recovery of the ^1H polarisation towards thermal equilibrium is observed. This is a manifestation of the tunnel diffusion process. During the preparation period, the tunnelling reservoir comes into contact with the electron spin, and the energy flows out of the tunnelling reservoir. The system is disturbed away from its pseudo-equilibrium state, and a much larger or smaller initial ^1H polarisation is therefore generated. Once the recovery field is set to be non-resonant, the energy is redistributed towards equilibrium via tunnel diffusion, which is accompanied by the spin flip in the nuclear states, resulting in the continued observation of the recovery of the ^1H polarisation.

From the data in Fig. 6.12, the time constant characterising the tunnel diffusion process is measured to be $T_{\text{diff}} = 25\text{s}$, approximately. It is significant that the diffusion time constants are the same in all samples. This reveals that the tunnel diffusion process is independent of the copper ion concentration, and this is consistent with the fact that electron spins are not involved in the tunnel diffusion process.

Similar to simulations of the tunnel resonance experiments, numerical simulations of the tunnel diffusion curves shown in Fig. 6.12 were made. The simulated ^1H polarisation $\langle I_z \rangle$ is illustrated by the solid lines in Fig. 6.12, and good agreement is achieved for all cases. The evolution of tunnelling temperatures θ_t in the simulation of the case of preparation field $B_{TR} = 0.045\text{T}$ for sample II (red, filled squares in Fig. 6.12) is presented in Fig. 6.13 in 3D as a function of time t and tunnelling frequency ν .

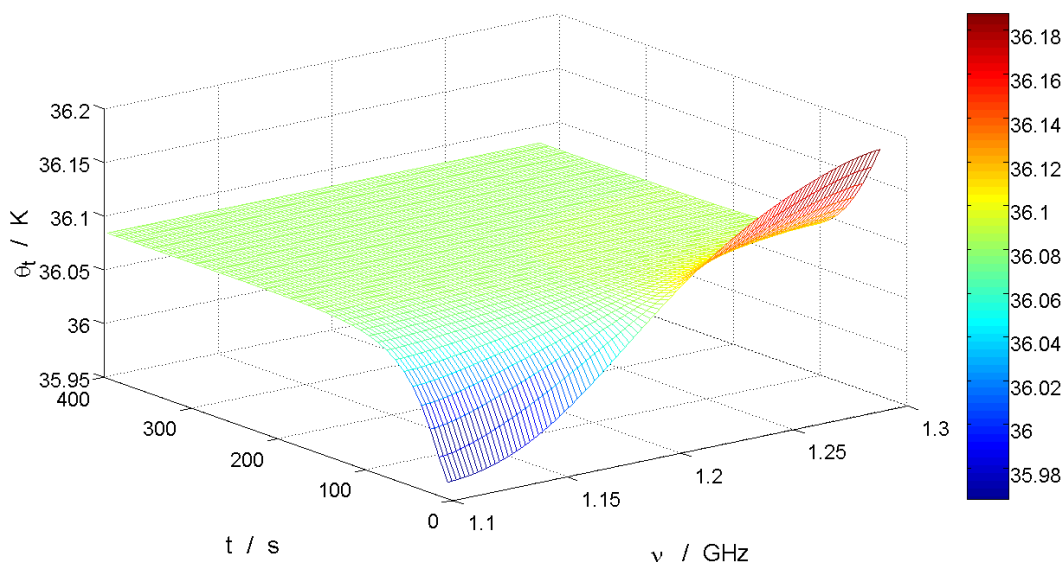


Figure 6.13 Evolution of tunnelling temperatures θ_t as a function of time t and tunnelling frequency ν from the simulation of the tunnel diffusion curve shown as the red, filled squares in Fig. 6.12

During the preparation period, there is resonant contact between electron spins and a narrow region of the tunnelling reservoir centred at approximately $\nu = 1.13\text{GHz}$, thereby causing energy to flow out of this region of the tunnelling distribution, and hence cooling it. However, the non-resonant regions of the tunnelling distribution (e.g. $\nu = 1.27\text{GHz}$) remain almost undisturbed. Therefore at time $t = 0$, the tunnelling temperature θ_t about the preparation frequency is colder than that at regions that are non-resonant. With increasing time, the tunnelling temperature across the distribution is equilibrated via tunnel diffusion.

Because the spin-lattice relaxation time T_1 is very slow for this sample, in the cases of above experiments, the effect of the spin-lattice relaxation mechanism on the experimental results is negligible. To reveal the effect of the spin-lattice relaxation, some other experiments were conducted using the saturation-recovery pulse sequence (Fig. 3.13). The ^1H polarisation was recorded on samples I, II and III at both positive and negative lobes of the DNP lineshape, i.e. $B_r = 0.048\text{T}$ and 0.045T . For comparison, the ^1H polarisation recovered at non-resonant field $B_r = 0.089\text{T}$ was also recorded, and the results are presented in Fig. 6.14.

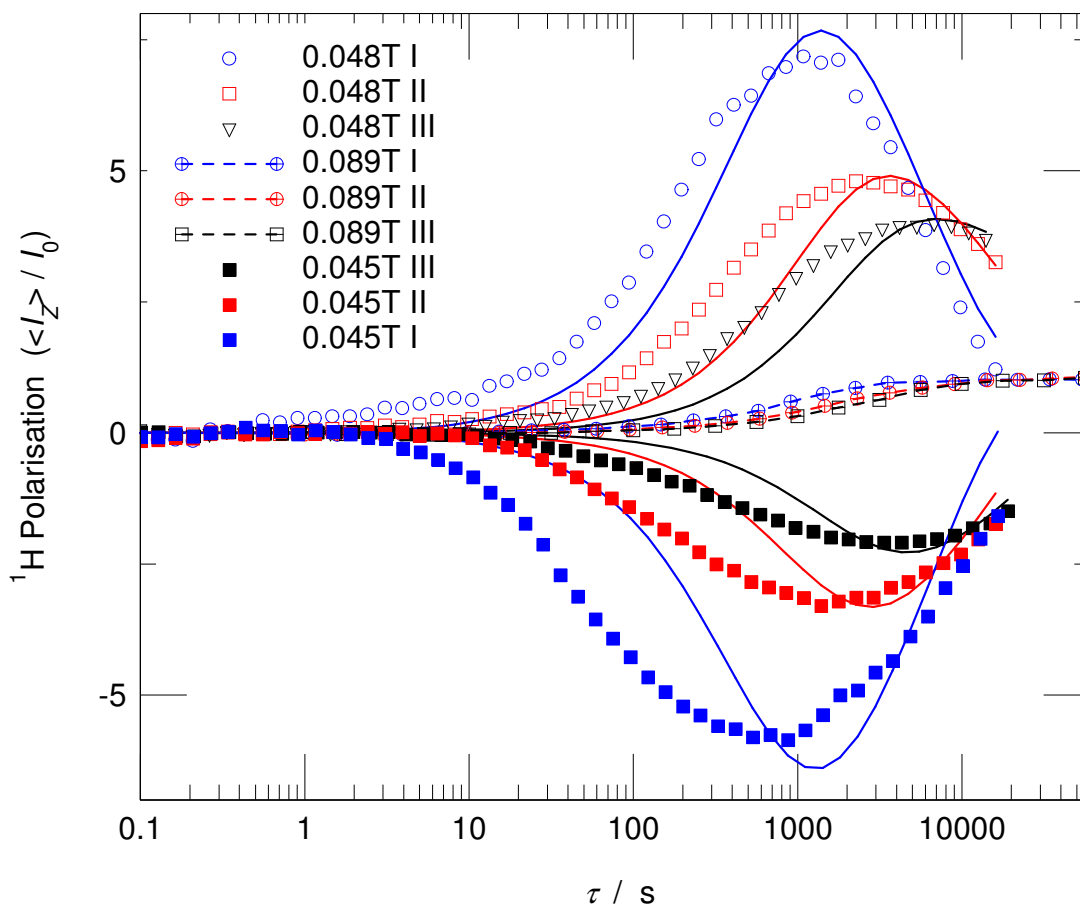


Figure 6.14 Results of the saturation-recovery experiments on copper doped zinc acetate dihydrate ($T = 4.2\text{K}$); solid lines represent simulation results

It is clear that with increasing recovery time τ , in the case of a positive lobe (i.e. $B_r = 0.048\text{T}$, open points), the ^1H polarisation is increased up to a value that is substantially larger than thermal equilibrium. While in the case of a negative lobe (i.e. $B_r = 0.045\text{T}$, filled points), the ^1H polarisation is inverted significantly. These results are the manifestations of the DNP phenomenon. When the recovery time τ is long enough, it is observed that the ^1H polarisation is recovered towards thermal equilibrium. This reveals the effect of the spin-lattice relaxation mechanism. In the simulation of this experiment, apart from calculations of the ^1H

polarisation due to tunnel resonant contact with the electron spin and tunnel diffusion discussed above, the change in ^1H polarisation due to the spin-lattice relaxation mechanism was simultaneously calculated every 1 second, by using Eqn. (6.5). The overall ^1H polarisation from the simulation of the three mechanisms is presented by the solid lines in Fig. 6.14. The estimate of spin-lattice relaxation time T_1 at the field $B_r = 0.048\text{T}$ was firstly made by extrapolating the value of T_1 measured at $B_r = 0.089\text{T}$, was then refined in the numerical simulation to be $T_1 = 600 \pm 30$ s, 1200 ± 60 s and 1800 ± 90 s for samples I, II and III, respectively. It is clear that increasing the copper ion concentration affects the ^1H polarisation in two ways: (1) the enhancement effect of ^1H polarisation is stronger due to more tunnel resonant contacts with the electron spin; (2) the spin-lattice relaxation time T_1 is faster, and this is consistent with the trend in the non-resonant T_1 curves ($B_r = 0.089\text{T}$), where T_1 is measured to be 1010 ± 50 s, 2140 ± 100 s and 2890 ± 150 s for samples I, II and III, respectively. This is because more unpaired electrons cause more contacts with the tunnelling reservoir and hence more transitions can occur, thereby inducing the ^1H spins to relax more quickly.

Label	I	II	III
(Cu:Zn) ratio	1:18.2	1:54.5	1:218
$T_1(48\text{mT}) / \text{s}$	600 ± 30	1200 ± 60	1800 ± 90
$T_1(89\text{mT}) / \text{s}$	1010 ± 50	2140 ± 100	2890 ± 150
$aW^{(-)} = aW^{(+)} / \text{Ks}^{-3}$	$(4.4 \pm 0.2) \times 10^{16}$	$(1.8 \pm 0.1) \times 10^{16}$	$(0.90 \pm 0.04) \times 10^{16}$
$a_tW^{(-)} = a_tW^{(+)} = a_tW^{(0)} / \text{s}^{-3}$	$(2.0 \pm 0.1) \times 10^{13}$	$(0.70 \pm 0.03) \times 10^{13}$	$(0.35 \pm 0.02) \times 10^{13}$
k_d / s^{-1}	0.040 ± 0.002	0.040 ± 0.002	0.040 ± 0.002
$k_0 / \text{K}^{-1} \text{s}^{-2}$	$(2.25 \pm 0.05) \times 10^9$	$(2.25 \pm 0.05) \times 10^9$	$(2.25 \pm 0.05) \times 10^9$

Table 6.2 Best fit parameters for copper doped zinc acetate single crystals; $g_{\text{obs}} = 2.38 \pm 0.03$,

$$A_{\text{Cu}} = 7.25 \pm 0.05 \text{ mT}, \omega_t = 7.25 \times 10^9 \text{ s}^{-1} [71] \text{ and } b = (1.9 \pm 0.1) \times 10^8 \text{ s}^{-1}$$

6.4.2 Toluene doped with DPPH radicals

In this thesis, the α -crystalline phase of toluene has been studied. Two methyl tunnelling splittings in α -crystalline toluene have earlier been revealed by neutron scattering experiments, and the tunnelling frequencies are $\nu_t^{(1)} = 6.29\text{GHz}$ and $\nu_t^{(2)} = 6.89\text{GHz}$, respectively [72].

In this work, toluene was doped with DPPH radicals by mixing the compounds at room temperature. The tunnel resonant contact between methyl tunnelling reservoirs and electron spins associated with DPPH radicals is made. To reveal the phenomenon of tunnel resonance, some experiments were conducted by using the level-crossing pulse sequence (Fig. 3.17), and the results are presented in Fig. 6.15.

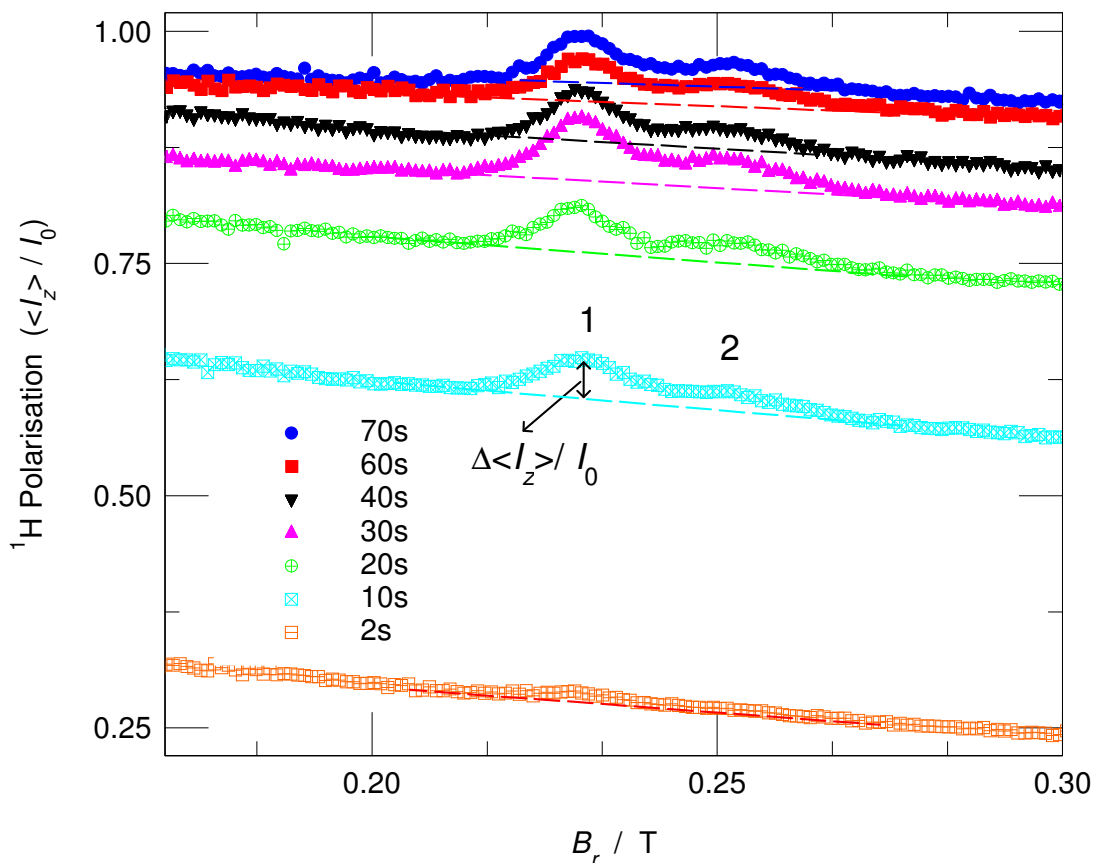


Figure 6.15 Tunnel resonance spectra of toluene doped with DPPH radicals ($T = 4.2\text{K}$); dashed lines are shown as eye guides

The ^1H polarisation was recorded at a variety of recovery times $2\text{s} \leq \tau_{\text{rec}} \leq 70\text{s}$ at $T = 4.2\text{K}$. The dashed lines are shown as eye guides. In each spectrum, two peaks centred at $B_r^{(1)} = 0.230 \pm 0.002\text{ T}$ and $B_r^{(2)} = 0.251 \pm 0.002\text{ T}$ are observed, and this reveals the enhancement of nuclear polarisation. These two peaks are related to two characteristic tunnelling frequencies of the methyl groups in α -crystalline toluene. Given $\nu_t = \gamma_e B_r / 2\pi$, where γ_e is the magnetogyric ratio of the electron, the following tunnelling frequencies $\nu_t^{(1)} = 6.45 \pm 0.05\text{ GHz}$ and $\nu_t^{(2)} = 7.03 \pm 0.06\text{ GHz}$ are obtained. This is consistent with the results from neutron scattering experiments [72].

For peak 1, with increasing the recovery time τ_{rec} , it is clear that the relative enhancement of ^1H polarisation $\Delta\langle I_z \rangle / I_0$ (indicated in Fig. 6.15, defined as the amplitude of the peak at $B_r^{(1)} = 0.230\text{T}$ minus the background), is increased then decreased. This reveals a competition between two mechanisms that simultaneously affect the ^1H polarisation. One mechanism is the spin-lattice relaxation of the nuclear spin, and the other is the DNP mechanism due to the tunnel resonant contact between the methyl tunnelling reservoir and the electron spin. The ^1H polarisation is enhanced in the DNP process, whereas the spin-lattice relaxation simultaneously causes the ^1H polarisation to recover towards thermal equilibrium. For a particular recovery time τ_{rec} , the observed ^1H polarisation is the net result of the two mechanisms. When recovery times are short (i.e. $\tau_{\text{rec}} \leq 30\text{s}$), the increase of the relative ^1H polarisation $\Delta\langle I_z \rangle / I_0$ with increasing recovery time τ_{rec} shows the dominance of the DNP process. However, in the case of long recovery times (i.e. $\tau_{\text{rec}} \geq 40\text{s}$), the relative ^1H polarisation $\Delta\langle I_z \rangle / I_0$ is decreased with increasing recovery time τ_{rec} . This is due to the effect of spin-lattice relaxation on the ^1H polarisation. The spin-lattice relaxation time T_1 at $B_r = 0.23\text{T}$, which is estimated to be 90s by extrapolating the evolution of ^1H polarisation at non-resonant field $B_r = 0.2\text{T}$ from Fig. 6.15, is comparable with the recovery time τ_{rec} in this case.

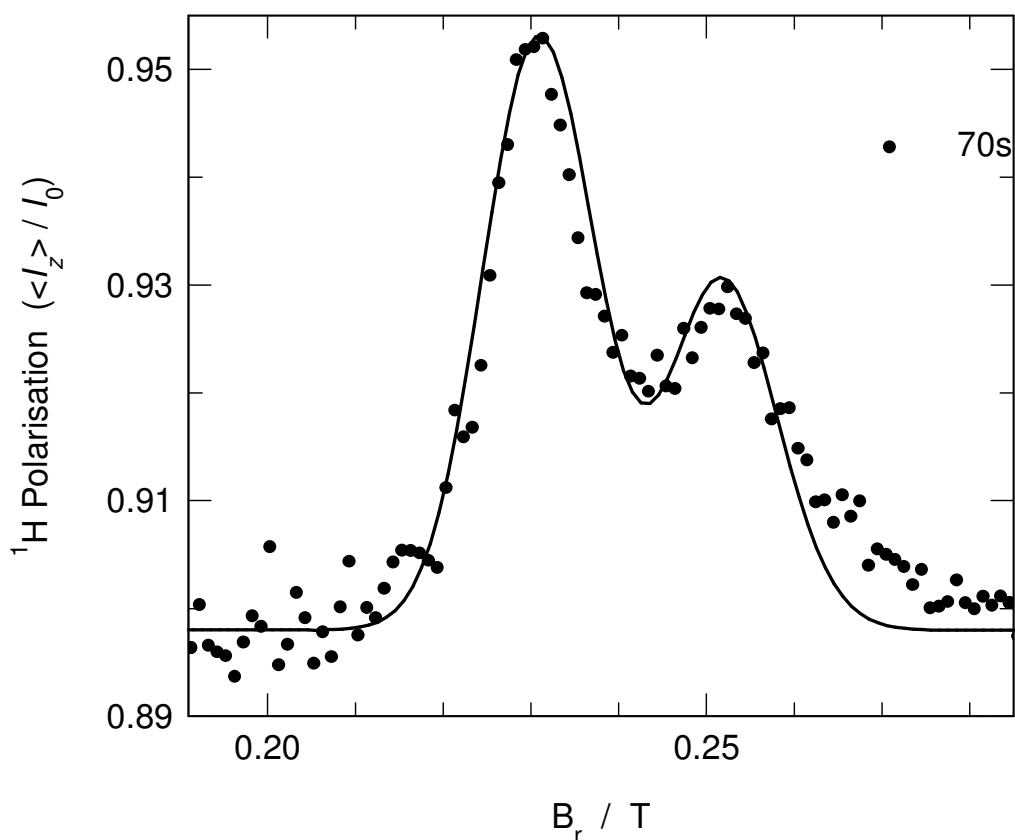


Figure 6.16 Result of the numerical simulation of the tunnel resonance spectrum of toluene doped with DPPH radicals with $\tau_{\text{rec}} = 70\text{s}$; experimental data are shown as points

As with the numerical simulation procedure discussed above, the tunnel resonance spectrum for $\tau_{\text{rec}} = 70\text{s}$ was simulated, and the result is shown as the solid line in Fig. 6.16, and the best fit parameters are presented in Table 6.3. Good agreement with the experimental data (points in Fig. 6.16) is obtained. It should be noted that in the numerical simulation, the change in ^1H polarisation due to tunnel diffusion is very small so that the tunnel diffusion mechanism can be neglected in the case of toluene doped with DPPH radicals.

Unlike the tunnel resonance spectrum of copper doped zinc acetate dihydrate (Fig. 6.6), the presence of the negative peak that is characteristic of DNP lineshape is not evident in Fig. 6.16. This may be accounted for by the results of the numerical simulation. The best fit values of transition probabilities per unit time are, $W^{(-)} / W^{(+)} = 1.65$. This shows that the transition probability per unit time $W^{(-)}$ is larger than $W^{(+)}$. It is these non-equal transition probabilities that give rise to this asymmetric lineshape. Additionally, the calculated amplitude ratio of the two tunnelling peaks is $A^{(2)} / A^{(1)} = 0.53$, and this is consistent with the neutron scattering experimental results [72].

$\nu_r^{(1)}$	$6.450 \pm 0.008 \text{ GHz}$
$\nu_r^{(2)}$	$7.032 \pm 0.008 \text{ GHz},$
b	$(1.14 \pm 0.01) \times 10^9 \text{ s}^{-1}$
$A^{(2)} / A^{(1)}$	0.53 ± 0.01
$aW^{(+)}$	$(1.02 \pm 0.05) \times 10^{15} \text{ Ks}^{-3}$
$aW^{(-)}$	$(1.68 \pm 0.08) \times 10^{15} \text{ Ks}^{-3}$
$a_r W^{(+)}$	$(1.06 \pm 0.05) \times 10^{13} \text{ s}^{-3}$
$a_r W^{(-)}$	$(1.75 \pm 0.08) \times 10^{13} \text{ s}^{-3}$
$a_r W^{(0)}$	$(1.40 \pm 0.07) \times 10^{13} \text{ s}^{-3}$
$T_1 (B_r = 0.23\text{T})$	$90 \pm 5 \text{ s}$

Table 6.3 Best fit parameters for toluene doped with DPPH radicals

6.5 Conclusions

We shall compare the tunnel resonance spectra of single crystals of copper doped zinc acetate dihydrate with that of toluene doped with DPPH radicals. Apart from the difference arising from the inherent lineshapes of the different samples (four-fold ESR spectrum associated with the former sample, while two inherent tunnelling peaks for the latter one), there are two significant differences as follows.

The first is that in terms of the maximum ^1H polarisation, compared with copper doped zinc acetate dihydrate, the enhancement is much smaller in the case of toluene doped with DPPH radicals. This may be due to its fast spin-lattice relaxation time T_1 ($\sim 90\text{s}$) compared with the contact time for the DNP process to evolve in the toluene sample. Even when the recovery time is relatively short ($2\text{--}70\text{s}$), the spin-lattice relaxation mechanism plays a very important role, which makes the ^1H polarisation recover towards thermal equilibrium very quickly. However for the former sample, the T_1 ($>600\text{s}$) is very slow therefore it is possible for a larger enhancement of the ^1H polarisation to be obtained.

The second difference is that in the case of latter sample, on the low-field side of tunnel resonance, no evident negative peak has been observed. This asymmetric tunnel resonance spectrum is attributable to the different transition probabilities per unit time, $W^{(-)} / W^{(+)} = 1.65$. However, for the former sample, the same transition probabilities gave rise to a rather symmetric DNP lineshape. This also reflects in part the apparent absence of tunnel diffusion in the toluene sample.

To conclude, two examples of tunnel resonance spectra have been investigated; one exhibits strong diffusion of tunnelling energy, while this is negligible in the other. The numerical simulations in both cases provide very good agreement with a wide variety of tunnel resonance experiments designed to emphasise the DNP lineshapes, the diffusion of tunnelling energy and the cooling of the tunnelling reservoir as well as the time evolution of the ^1H polarisation. The quality of the agreement between experiments and numerical simulations demonstrates the validity of theoretical framework that describes the tunnel resonance phenomenon.

Chapter 7 Summary

The quantum dynamics and tunnelling of methyl rotors, and associated phenomena, has been studied using field-cycling NMR.

Methyl tunnelling frequencies have been directly measured in methylmalonic acid and methyl ethyl ketone using low-field dipole-dipole driven experiments (i.e. 77kHz for methylmalonic acid and 494kHz for methyl ethyl ketone). Dramatic modifications of the Selection Rules at low magnetic fields allow transitions that are forbidden at high field to occur; these transitions have been observed in the low-field NMR spectra. It has been shown that stirring low-field NMR can be used to enhance the tunnelling sidebands. rf irradiation stirred at the frequency of a particular tunnelling sideband, say $a+$, results in enhancement of the opposite sideband, $a-$. The degree of enhancement has been shown to be dependent on the irradiation time.

Temperature-dependent and field-dependent measurements of the spin-lattice relaxation time have been conducted on sodium acetate trihydrate and sorbic acid. Correlation times characteristic of CH_3 reorientations have been determined. Given the rotational Hamiltonian, methyl hindering potentials have been calculated (i.e. $V_3/k_B = 496\text{K}$ and $V_6/k_B = -137\text{K}$ for sodium acetate trihydrate and $V_3/k_B = 1146\text{K}$ for sorbic acid). The Haupt equations have been simulated, and good agreement with the experimental data has been shown. In the case of sodium acetate trihydrate, the Haupt maximum has been observed in the $T_1^{-1}(1/T)$ plot, and the broadening feature due to methyl tunnelling has been revealed in the spectral density. For sorbic acid, the methyl tunnelling frequency was measured to be 4.1MHz, which is to date the highest methyl tunnelling frequency measured by low-field NMR. Components arising from methyl tunnelling have been observed as discrete peaks in the spectral density. Dynamical components associated with CH_3 reorientations have been successfully distinguished from a second dynamical process, i.e. proton transfer in the hydrogen bonds, by mapping the spectral density.

ESR tunnel resonance and associated phenomena has been investigated in copper doped zinc acetate dihydrate, and toluene doped with DPPH radicals. The phenomenon of DNP has been observed in both samples. For the former sample, the cooling rate of the tunnelling reservoir has been measured at tunnel resonance, and the spectral diffusion of the tunnelling energy has been demonstrated, by using a variety of NMR pulse sequences. The rate of cooling of the tunnelling reservoir was measured to be in the range $3 \times 10^4 - 2 \times 10^5 \text{s}$, depending on the copper ion concentration. The rate of tunnel diffusion was found to be 25s, and is not

dependent on the copper ion concentration. The competition between the DNP and spin-lattice relaxation mechanism has been shown in the time evolution of the ^1H polarisation experiments. It has been shown that higher concentrations of copper electrons result in a stronger DNP effect. Numerical simulations considering the DNP, tunnel diffusion and spin-lattice relaxation mechanisms have been carried out, and good agreement with the experimental data has been achieved. In the case of the DPPH doped toluene sample, the tunnel resonance has been observed, however the tunnel diffusion was found to be negligible.

Chapter 8 Bibliography

- [1] Isaac Newton, *Philosophiae naturalis principia mathematica*, Royal Society, 1687
- [2] Per F Dahl, *Flash of Cathode Rays: a history of J.J. Thomson's electron*, Institute of Physics Publishing, 1997
- [3] B.H. Bransden, C.J. Joachain, *Introduction to Quantum Mechanics*, Longman Scientific and Technical, 1989
- [4] A.J. Horsewill, *Progr. Nucl. Magn. Reson. Spectrosc.* **35** (1999) 359
- [5] J.G. Powles, H.S. Gutowsky, *J. Chem. Phys.* **23** (1955) 1692
- [6] E.O. Stejskal, H.S. Gutowsky, *J. Chem. Phys.* **28** (1958) 388
- [7] C.P. Smyth, *Chem. Rev.* **19** (1936) 329
- [8] N. Bloembergen, E.M. Purcell, R.V. Pound. *Phys. Rev.* **73** (1948) 679
- [9] J.H. Van Vleck. *Phys. Rev.* **74** (1948) 1168
- [10] H.S. Gutowsky, G.E. Pake. *J. Chem. Phys.* **18** (1950) 162
- [11] E.O. Stejskal, D.E. Woessner, T.C. Farrar, H.S. Gutowsky, *J. Chem. Phys.* **31** (1959) 55
- [12] J. Haupt, *Z. Naturforsch.* **26a** (1971) 1578
- [13] B. Alefeld, A. Kollmar, B.A. Dasannacharya, *J. Chem. Phys.* **63** (1975) 4415
- [14] W Muller-Warmüth, R Schüler, M Prager, A Kollmar, *J. Chem. Phys.* **69** (1978) 2382
- [15] M. Prager, A. Heidemann, *Chem. Rev.* **97** (1997) 2933
- [16] S. Clough, A.J. Horsewill, P.J. McDonald, F.O. Zelaya, *Phys. Rev. Lett.* **55** (1985) 1794
- [17] S. Clough, T. Hobson, *J. Phys. C: Solid State Phys.* **7** (1974) 3387
- [18] S. Clough, W.S. Hinshaw, T. Hobson, *Phys. Rev. Lett.* **31** (1973) 1375
- [19] Massimi, Michela, *Pauli's Exclusion Principle*, Cambridge University Press, 2005
- [20] Werner Press, *Single-Particle Rotations in Molecular Crystals*, Springer-Verlag, 1981
- [21] P. Van Hecke, G. Janssens, *Phys. Rev. B* **17** (1978) 2124
- [22] M. Punkkinen, J.E. Tuohi, E.E. Ylinen, *Chem. Phys. Lett.* **36** (1975) 393
- [23] H. Glättli, A Sentz, M. Eisenkremer, *Phys. Rev. Lett.* **28** (1972) 871
- [24] S. Clough, A.J. Horsewill, M.N.J. Paley, *Phys. Rev. Lett.* **46** (1981) 71
- [25] S. Clough, A.J. Horsewill, M.N.J. Paley, *J. Phys. C: Solid State Phys.* **15** (1982) 3803
- [26] P.S. Allen, S. Clough, *Phys. Rev. Lett.* **22** (1969) 1351
- [27] A.J. Horsewill, *Spectrochimica Acta* **48A** (1992) 379
- [28] A. Abragam, *The Principles of Nuclear Magnetism*, Clarendon Press, Oxford, 1961
- [29] M.H. Levitt, *Spin dynamics*, John Wiley and Sons, Ltd., 2000
- [30] J.W. Hennel, J. Klinowski, *Fundamentals of Nuclear Magnetic Resonance*, Longman Scientific and Technical, 1993
- [31] C.P. Slichter, *Principles of Magnetic Resonance, Third Edition*, Springer-Verlag, 1990

- [32] E. Fukushima, S.B.W. Roeder, *Experimental Pulse NMR. A Nuts and Bolts Approach*, Addison-Wesley, Reading, Massachusetts, 1981
- [33] J.C. Raich, H.M. James, *Phys. Rev. Lett.* **16** (1966) 173
- [34] D.C. Mattis, *The Theory of Magnetism I Statics and Dynamics*, Springer-Verlag, 1981
- [35] T. Hobson, PhD Thesis, Nottingham, 1975
- [36] F. Noack, *Progr. Nucl. Magn. Reson. Spectrosc.* **18** (1986) 171
- [37] R. Kimmich, *Bull. Magn. Reson.* **1** (1980) 195
- [38] R. Kimmich, E. Anordo, *Progr. Nucl. Magn. Reson. Spectrosc.* **44** (2004) 257
- [39] S.H. Koenig, R.D. Brown III, *Progr. Nucl. Magn. Reson. Spectrosc.* **22** (1990) 487
- [40] A.J. Horsewill, *Progr. Nucl. Magn. Reson. Spectrosc.* **52** (2008) 170
- [41] Q. Xue, PhD Thesis, Nottingham, 2003
- [42] W. Wu, PhD Thesis, Nottingham, 2005
- [43] A.M. Alsanosi, A.J. Horsewill, *Chem. Phys.* **160** (1992) 25
- [44] A.J. Horsewill, A. Aibout, *J. Phys.: Condens. Matter* **1** (1989) 10533
- [45] A.M. Alsanosi, A.J. Horsewill, S. Clough, *J. Phys. Condens. Matter* **1** (1989) 643
- [46] M. Van Cleemput, A. Buekenhoudt, L. Van Gerven, A.J. Horsewill, *J. Chem. Phys.* **103** (1995) 2787
- [47] N.H. Jones, PhD Thesis, Nottingham, 2002
- [48] K.J. Abed, S. Clough, A.J. Horsewill, M.A. Mohammed, *Chem. Phys. Lett.* **147** (1988) 624
- [49] M.J. Barlow, S. Clough, A.J. Horsewill, M.A. Mohammed, *Solid State Nucl. Mag. Res.* **1** (1992) 197
- [50] S. Clough, G.J. Barker, K.J. Abed, A.J. Horsewill, *Phys. Rev. Lett.* **60** (1988) 136
- [51] M.A. Neumann, M. Johnson, A. Aibout, A.J. Horsewill, *Chem. Phys.* **229** (1998) 245
- [52] M.J. Barlow, S. Clough, P.A. Debenham, A.J. Horsewill, *J. Phys.: Condens. Matter* **4** (1992) 4165
- [53] S.R. Booth, S. Clough, P.J. McDonald, *J. Phys. C: Solid State Phys.* **17** (1984) L379
- [54] S. Clough, A.J. Horsewill, M.R. Johnson, I.B.I. Tomsah, *Mol. Phys.* **78** (1993) 781
- [55] S. Clough, A. Heidemann, A.J. Horsewill, J.D. Lewis, M.N.J. Paley, *J. Phys. C: Solid State Phys.* **14** (1981) L525
- [56] D.F. Brougham, A.J. Horsewill, R.I. Jenkinson, *Chem. Phys. Lett.* **272** (1997) 69
- [57] R.I. Jenkinson, A. Ikram, A.J. Horsewill, H.P. Trommsdorff, *Chem. Phys.* **294** (2003) 95
- [58] Q. Xue, A.J. Horsewill, M.R. Johnson, H.P. Trommsdorff, *J. Chem. Phys.* **120** (2004) 11107
- [59] W. Wu, D.L. Noble, A.J. Horsewill, *Chem. Phys. Lett.* **402** (2005) 519
- [60] J.L. Skinner, H.P. Trommsdorff, *J. Chem. Phys.* **89** (1988) 897
- [61] A.-S. Montjoie, W. Müller-Warmuth, *Z. Naturforsch* **40a** (1985) 596

- [62] F. Köksal, E. Röessler, H. Sillescu, *J. Phys. C: Solid State Phys.* **15** (1982) 5821
- [63] S. Clough, A. Heidemann, M. N.J. Paley, J.B. Suck, *J. Phys. C: solid State Phys.* **13** (1980) 6599
- [64] S. Clough, A. Heidemann, A.J. Horsewill, J.D. Lewis, M.N.J. Paley, *J. Phys. C: Solid State Phys.* **15** (1982) 2495
- [65] P.S. Allen, *J. Phys. C* **7** (1974) L22
- [66] T. Ratajczyk, S. Szymański, *J. Chem. Phys.* **123** (2005) 204509
- [67] P. Gutsche, H. Schmitt, U. Haeblerlen, T. Ratajczyk, S. Szymański, *Chemphyschem* **7** (2006) 886
- [68] N.M. Atherton, A.J. Horsewill, *Mol. Phys.* **42** (1981) 985
- [69] S. Clough, B.J. Mulady, *Phys. Rev. Lett.* **30** (1973) 161
- [70] D. Cavagnat, J. Lascombe, J.C. Lassegues, A.J. Horsewill, A. Heidemann, J.B. Suck, *J. Physique*, **45** (1984) 97
- [71] S. Clough, A. Heidemann, M. Paley, *J. Phys. C: Solid State Phys.* **14** (1981) 1001
- [72] D. Cavagnat, A. Magerl, C. Vettier, S. Clough, *J. Phys. C: Solid State Phys.* **19** (1986) 6665